POLITECNICO DI TORINO

Collegio di Ingegneria Chimica e dei Materiali

**Corso di Laurea Magistrale**
**in Ingegneria Chimica e dei Processi Sostenibili**


Tesi di Laurea Magistrale

# Computational fluid dynamics simulations of flows in stirred tanks: application to bio-reactors



**Relatore**

prof. Daniele Marchisio

**Candidato**

Enrico Agostini


Marzo 2019

# Sommario

I reattori agitati meccanicamente sono apparecchiature comunemente usate in molte applicazioni industriali per le buone performance in termini di miscelazione, per il semplice design e per la facilità di funzionamento. Tuttavia, la modellazione del flusso al loro interno è complicata perché il sistema è dominato dal moto turbolento e dipende fortemente dalle proprietà fisiche del fluido. I metodi della *Computational Fluid Dynamics* (CFD) rappresentano un valido strumento di indagine per convalidare modelli più rigorosi per la descrizione dell'idrodinamica del miscelatore.

L'obiettivo del lavoro della presente tesi è quello di studiare la formazione di eterogeneità all'interno del sistema durante la produzione di enzimi, mediante fermentazione del fungo filamentoso *Trichoderma Reesei*, usando il software commerciale Ansys Fluent, identificando l'effetto della reologia complessa e della turbolenza.

Sono stati simulati due reattori, a singolo e doppio agitatore. Il modello turbolento è stato convalidato inizialmente simulando acqua e confrontando i risultati con i dati sperimentali raccolti. Il sistema acqua-aria è stato risolto usando un modello multifase euleriano-euleriano, testando diverse opzioni nella scelta di drag law, condizioni al contorno e modalità di simulazione con l'obiettivo di trovare il set-up migliore dal punto di vista della stabilità e convergenza della soluzione numerica.

Per descrivere il brodo di fermentazione, che ha un comportamento reologico non-Newtoniano pseudoplastico, si sono simulate soluzioni acquose di idrocolloidi (Carbossimetil Cellulosa e Gomma di Xantan). La viscosità di tali fluidi campione è stata descritta con il modello a legge di potenza, che è stato implementato nel software.

Infine, si è indagato sulla distribuzione della concentrazione di substrato all'interno del fermentatore e sulle traiettorie disegnate dai microrganismi durante il loro moto. Lo zucchero è stato simulato mediante l'equazione del trasporto di una grandezza scalare in diffusione nel reattore, alimentata dalla superficie superiore del serbatoio. Le traiettorie dei microorganismi sono state tracciate per mezzo di simulazioni lagrangiane di particelle discrete in moto casuale. Il passaggio attraverso una regione di campionamento ha permesso di fare un'analisi dell'ambiente con cui vengono a contatto.

Dai risultati ottenuti è emerso che i modelli turbolenti *Realizable k-ε* e *Standard k-ε* descrivono correttamente l'idrodinamica di un reattore miscelato quando il sistema si trova in regime turbolento completamente sviluppato, come per il caso dell'acqua. Se il sistema ha comportamento non-Newtoniano, con la presenza di ampie aree stagnati, il modello perde la sua accuratezza, pur riuscendo a prevedere il comportamento globale. Nel caso multifase è risultato che *Standard k-ε* è il modello che più garantisce la stabilità della simulazione. Inoltre, è emersa l'importanza del coefficiente di Brucato, nella drag-law, per ottenere risultati che rispettassero la realtà fisica. Infine, si è mostrato che il metodo del particle tracking può essere molto utile che, se correttamente implementato, a descrivere l'ambiente con cui i microorganismi vengono a contatto, per produrre dati da utilizzare in studi down-scale.

# Abstract

Mechanically stirred tanks are commonly used in several different industrial application because of their mixing performances and simplicity of design and operation. Despite this, the modelling of the inner flow field is difficult because of the chaotic turbulent motion or the physical properties of the fluid inside the tank. Computational Fluid Dynamics (CFD) represent a valuable tool to validate a rigorous model for the scale-up of stirred tanks and optimize their operating conditions.

The aim of this work is to investigate the fluid dynamics of an aerated bioreactor for enzyme production from filamentous fungi Trichoderma Reesei, using commercial simulation software Ansys Fluent, identifying the effect of the complex rheology and turbulence in the formation of heterogeneities of the flow.

Two stirred tanks, with single and double impeller, were simulated. The global flow field was computed using at first water as fluid, to validate the turbulent model with experimental data available from previous studies carried out at IFPEN during the last seven years. The water-air system was solved with a Euler-Euler multiphase turbulent model, using several interphases drag laws, as well as simulation setup to find the best combination to have a stable and converging solution along with a good prediction of the gas holdup in the vessel during operation. The results of the simulations would be used to validate the proposed gas-liquid model.

The power law rheological model was chosen to describe the complex flow field during microbial fermentation. The effect of the shear-thinning behaviour was investigated using Carboxymethyl Cellulose and Xanthan Gum solutions as model fluids, for they show similar behaviour to the fermentative broth.

Finally, the effect of the substrate distribution on the microbial growth and enzyme production was considered. The sugar was simulated as a scalar quantity diffusing inside the vessel, fed in semi-batch mode from the top surface. Then, cluster of microorganisms were simulated with a Lagrangian discrete particle simulations. Each particle, moving along the flow field transported by both a random walk mechanism as well as by turbulent convective flow, was tracked and an analysis concerning the passage in different substrate concentration areas was done. The data would be useful for future down-scale studies on microorganism behaviour in function of sugar concentration.

From the results obtained emerged that both *Realizable k-ε* and *Standard k-ε* correctly describe the internal hydrodynamics of the STR when the system is fully turbulent, e.g with water. If the system has a non-Newtonian behaviour, with wide stagnant areas, the model is less accurate, despite being able to predict the global flow. In the multiphase system, *Standard k-ε* showed to be the model which gave the most stable simulations. Furthermore, it emerged the importance of using the Brucato turbulent modification coefficient in the drag-law, in order to obtain physically consistent results. Finally, it was showed the usefulness of the particle tracking method which, if correctly implemented, can results in meaningful information, regarding microorganism and the environment they come in contact to. These results could be used in further down-scale studies.

# Contents

# Sommario esteso

Questo elaborato presenta il lavoro di tesi svolto in collaborazione con il centro di ricerca francese *Istitute Français du Petrol – Energie Nouvelle* (IFPEN), presso la sede di Solaize, Lione, nel dipartimento *R12 – Conception et modelisation de procédés* (Concezione e modellizzazione di processo), durante il periodo Marzo – Agosto 2018.

Lo studio è parte di un ampio progetto il cui elemento centrale è la produzione di biocarburanti di seconda generazione, nello specifico il *bioetanolo*, da biomassa di matrice lignocellulosica.

L'obiettivo di questo lavoro è di effettuare simulazioni numeriche della fluidodinamica all'interno di un bioreattore del tipo a serbatoio agitato, comunemente usati per la produzione microbica di enzimi. Utilizzando un software commerciale di Fluodinamica Computazionale, *Computational Fluid dynamics* in lingua inglese (CFD), si sono eseguite delle simulazioni per predire la miscelazione, la formazione di eterogeneità nel reattore e la distribuzione di substrato di fermentazione, nel caso di acqua, fluido con comportamento non-Newtoniano e in un sistema multifase gas-liquido, con liquido come fase continua e gas come fase dispersa.

Il manoscritto sarà così strutturato (con riferimento alla versione inglese):

Nel capitolo 2 è descritto l'inquadramento del lavoro di tesi all'interno del processo, approfondendo il sempre più crescente interesse verso i biocarburanti, in particolare la produzione di bioetanolo da biomassa lignocellulosica. Sono presentate le principali difficoltà da affrontare durante il processo fermentativo dal punto di vista fluidodinamico. Infine, è descritto il processo sviluppato presso IFPEN.

Il capitolo 3 descrive i principali aspetti teorici necessari a modellare la miscelazione in regime turbolento all'interno dei reattori agitati, con particolare riferimento alle grandezze globali per sistemi mono e multifase, con fluidi sia newtoniani sia non-Newtoniani.

Nel capitolo 4 sono riportati i principali modelli turbolenti e per sistemi multifase applicabili al caso in esame.

Il capitolo 5 descrive i metodi usati per le simulazioni numeriche, le griglie di calcolo e le impostazioni per i sistemi mono e multifase, con acqua o fluidi non-Newtoniani, inclusa la modifica della reologia. Inoltre, sono presentate le simulazioni per il sistema *fed-batch* e il metodo del *particle tracking*.

Nel capitolo 6 sono esposti gli esiti delle simulazioni, con analisi dei risultati e confronto con i dati sperimentali, disponibili da studi precedenti.

Infine, il capitolo 7 riassume globalmente il lavoro svolto e i risultati ottenuti, proponendo le possibili direzioni degli studi futuri sull'argomento.

# I Introduzione

La crescente domanda di energia a livello mondiale ha creato la necessità di trovare soluzioni più sostenibili dal punto di vista ambientale al problema dei carburanti. I biocarburanti prodotti da biomassa di scarto, detti di seconda generazione, sono una delle alternative più promettenti, in quanto possono aiutare a diminuire le emissioni di $CO_2$. In "Figura 2.1" (p. 4) si può vedere un confronto tra le tre tipologie di biocarburanti.

L'etanolo da fonti rinnovabili (impropriamente detto bioetanolo), uno dei biocarburanti più studiati, è prodotto dalla fermentazione alcolica di zuccheri semplici, che vengono estratti da matrice lignocellulosica di scarto, opportunamente pretrattata. Tali pretrattamenti possono essere sia meccanici, sia chimici, sia enzimatici, o una loro combinazione e servono a convertire i polimeri e i polisaccaridi che compongono la biomassa, principalmente cellulosa, emicellulosa e lignina, come spiegato in "Figura 2.2" (p. 4), in monosaccaridi, ad esempio il glucosio.

Gli enzimi idrolitici, come la *cellulase,* sono prodotti dalla fermentazione di funghi filamentosi, tra i quali il più comune è il *Trichoderma Reesei*. A causa della particolare morfologia di questo microorganismo, durante la fase di crescita il *brodo* di fermentazione assume un comportamento non-Newtoniano di tipo *pseudoplastico*, ovvero maggiore è lo shear rate $\dot{\gamma}$, minore sarà la viscosità apparente $\mu_a$. Questo aumento di viscosità durante la fermentazione, mostrato nei grafici di "Figura 2.3" (p. 6), causa il peggioramento del livello di miscelazione, portando alla formazione di eterogeneità nel bioreattore e ostacolando il trasporto di materia.

Il processo sviluppato presso IFPEN si configura in due fasi: la fase di crescita e la fase produttiva. Nella prima fase un inoculo del fungo filamentoso viene fatto crescere in un ambiente con elevate concentrazioni di nutrienti. L'aumento della concentrazione di biomassa è tale da necessitare l'uso di diversi bioreattori di dimensioni sempre crescenti. Il costante accrescimento della biomassa aumenta la viscosità del sistema, impedendo uno scambio di materia ottimale tra aria e liquido, limitando il trasporto di ossigeno ai microorganismi. Raggiunta una elevata concentrazione di biomassa comincia la seconda fase del processo.

Nella seconda fase, si deve impedire l'ulteriore crescita dei microrganismi, pertanto la concentrazione di substrato è mantenuta al minimo per stimolare la produzione di *cellulase*. Questa seconda fase avviene in modalità *fed-batch*, ovvero il reattore agitato, costantemente areato, viene alimentato con una portata di glucosio molto bassa e costante. Infine, al termine della fase produttiva il *brodo* di fermentazione viene filtrato per la separazione e il recupero dell'enzima e della biomassa.

# II Elementi teorici ed equazioni principali

I reattori agitati sono serbatoi cilindrici dotati di uno o più agitatori meccanici che ruotando mettono in moto il fluido contenuto al loro interno e di frangiflutti laterali che sopprimono l'effetto vortice creato dalla turbina. Le grandezze caratteristiche, usate per il dimensionamento, sono i diametri $T$ e $D$ rispettivamente del serbatoio e dell'agitatore e l'altezza $H$. L'immagine di "Figura 3.1" (p. 7) mostra un reattore "a sezione quadrata" ovvero la tipologia oggetto di

questo elaborato e comunemente studiata in ambito accademico, con altezza $H$ uguale a diametro $T$ e $D$ pari a $1/3T$, posizionato ad un'altezza $C$ pari a $1/3T$. Un'altra configurazione presa in esame è quella a doppio agitatore, molto frequente in ambito industriale, con altezza $H$ pari al doppio del diametro $T$.

Gli agitatori presi in considerazione durante le simulazioni sono: una girante a disco radiale, in particolare una turbina *Rushton* e una girante assiale, a lame inclinate (*Pitched-blade*) a 45°, mostrati in "Figura 3.2" (p. 8). Le turbine assiali producono un flusso di tipo circolatorio con elevato potere propulsivo, adeguato alla sospensione di solidi. Il campo di moto è costituito da due *loop* paralleli all'asse rotante dell'agitatore. Le turbine radiali, invece, generano un flusso con elevate velocità tangenziali, sforzo di taglio e turbolenza ma minor propulsione, fattori che le rendono ottimali per la dispersione di gas. Il campo di moto è caratterizzato da 4 *loop*, i due di maggiori dimensioni sopra il piano della turbina, i due minori al di sotto di tale quota. In "Figura 3.3" (p. 7) sono schematizzati le caratteristiche dei flussi.

## II.I Aspetti teorici dei reattori agitati

Le grandezze fisiche usate per progettare un reattore agitato generalmente sono la *potenza fornita* e il *tempo di miscelazione*. Queste grandezze possono essere espresse, per mezzo di numeri adimensionali e correlazioni matematiche, in funzione dei parametri di progetto, $D$ e $T$, delle condizioni operative, come la velocità di rotazione dell'agitatore $N$ e le proprietà fisiche del fluido, densità $\rho$ e viscosità $\mu$.

Nel caso di fluidi non-Newtoniani dilatanti, la viscosità può essere espressa con il modello a *legge di potenza*, o di Ostwald, Eq. (II.1), dove $K$ è l'*indice di consistenza* e $n$ è l'*indice di flusso*, inferiore a 1:

$$\tau = K\dot{\gamma}^n \tag{II.1}$$

La viscosità apparente $\mu_a$ è necessaria a quantificare la potenza da fornire al sistema. Essa è genericamente definita come il rapporto tra lo sforzo di taglio e il gradiente di velocità:

$$\mu_a = \frac{\tau}{\dot{\gamma}} = K\dot{\gamma}^{n-1} \tag{II.2}$$

La stima del gradiente di velocità, che appare nell'Eq. (II.3) è stata per la prima volta proposto da Metzner e Otto (1957), dove è ipotizzato che in un fluido non-Newtoniano pseudoplastico, in regime laminare, esista uno *shear-rate* medio $\dot{\gamma}_A$, direttamente proporzionale alla velocità dell'agitatore, con costante di proporzionalità $k_m$, costante di Metzner-Otto, specifica per tipo di turbina:

$$\dot{\gamma}_A = k_s N \tag{II.3}$$

Questa relazione è stata utilizzata con successo anche in condizioni diverse dal regime di flusso laminare (Venneker et al. 2010; Ameur and Bouzit 2012; Zhang et al. 2017; Khapre A. e Munshi B. 2014). In Sánchez Pérez et al. (2006) è stata ricavata, mediante analisi rigorosa, una equazione generalizzata, Eq. (II.4), proponendone un'estensione al campo turbolento, Eq. (II.5):

$$\dot{\gamma} = qN \tag{II.4}$$

$$\dot{\gamma} = q' N^{\frac{3}{1+n}} \tag{II.5}$$

I principali numeri adimensionali che descrivono il sistema sono: *Reynolds*, rapporto tra i fenomeni di trasporto inerziali e molecolari, *Froude*, rapporto tra le forze di inerzia e quelle

gravitazionali e il *numero di potenza*, un coefficiente di proporzionalità simile al coefficiente d'attrito nei tubi, indice della potenza fornita dall'agitatore. Le definizioni sono indicate nelle Eq. (II.1 – 3):

$$Re = \frac{\rho N D^2}{\mu} \tag{II.6}$$

$$Fr = \frac{N^2 D}{g} \tag{II.7}$$

$$N_p = \frac{P}{\rho N^3 D^5} \tag{II.8}$$

Il tempo di miscelazione $\theta_m$ è definibile come la quantità di tempo che un tracciante, iniettato nel reattore, impiega per raggiungere una concentrazione omogenea in tutto il volume. È, dunque, una grandezza legata ai parametri geometrici, alle condizioni operative e all'energia fornita al sistema. Nienow (1998) riportata una relazione proporzionale tra $\theta_m$ e le grandezze prima citate, prototipo per numerose relazioni ricavate sperimentalmente e specifiche rispetto alle condizioni di processo:

$$\theta_m \propto \frac{{N_p}^{-\frac{1}{3}}}{N}\left(\frac{D}{T}\right)^{-2} \tag{II.9}$$

L'insufflazione di un gas all'interno del reattore provoca cambiamenti nella fluidodinamica globale del sistema. In letteratura tre differenti regimi gas-liquido sono stati identificati: *footing*, *loading*, *fully recirculated*, mostrati in "Figura 3.5" (p. 14). Il primo si verifica se l'energia fornita dall'agitatore non è sufficiente a disperdere la fase gassosa, che quindi risale fino in superficie intrappolata dal vortice intorno all'asse rotante. L'ultimo regime è quello tipico di reattore ben agitato, in cui la fase gas si disperde omogeneamente nel fluido, con bolle di piccole dimensioni.

La transizione tra un regime di flusso e l'altro è identificata dal numero di Froude *Fr* e il numero di *flusso gassoso* $Fl_G$, definito in Eq. (3.24) ( p. 42) e rappresentata in una "mappa di flusso" (Lee and Dudukovic 2014), riportata in "Figura 3.6" (p. 15). Il gas, raggiunte le condizioni di dispersione, tende ad accumularsi nelle aree a bassa pressione dietro alle lame dell'agitatore, formando cavità (vedi "Figure 3.7-8" (p. 43 – 44) e diminuendo l'assorbimento di potenza del sistema. Questo fenomeno è stato ampiamente descritto e in letteratura sono presenti numerose correlazioni (Bouaifi and Roustan 2011; Luong and Voleky 1979; Gabelle et al. 2011; Paul et al. 2004). L'equazione proposta da Gabelle et al. (2011), convalidata per un ampio range di condizioni operative negli studi relativi ai bioreattori condotti presso IFPEN, evidenzia la forte influenza dei fattori geometrici e della portata di gas sulla potenza assorbita:

$$\ln\frac{P_G}{P} = -15.36\ {Q_G}^{0.62} T^{-1.27}\left(\frac{D}{T}\right)^{0.51} {N_P}^{0.16} \tag{II.10}$$

## II.II Modellazione della turbolenza

Il comportamento di un fluido in movimento è descritto dalle equazioni di conservazione della massa e della quantità di moto, ovvero l'*equazione di continuità* (II.1) e le *equazioni di Navier-Stokes* (II.2):

$$\frac{\partial \rho}{\partial t} + \frac{\partial(\rho U_i)}{\partial x_i} = 0 \tag{II.11}$$

$$\frac{\partial(\rho U_i)}{\partial t} + \frac{\partial\left(\rho U_i U_j\right)}{\partial x_j} = -\frac{\partial p}{\partial x_i} + \frac{\partial d_{ij}}{\partial x_j} + \rho g_i \qquad \text{(II.12)}$$

Dove $g_i$ è la componente i-esima dell'accelerazione gravitazionale e $d_{ij}$ è il tensore degli sforzi viscosi, che dipende dal comportamento reologico del fluido. Il metodo *direct numerical simulation* (DNS), ovvero la soluzione diretta di queste equazioni senza nessun tipo di modellazione, non è una strategia percorribile per applicazioni ingegneristiche, in quanto richiede elevate risorse computazionali. È possibile verificare (§4.2) che per tali condizioni il numero di celle necessarie è $N \sim Re^{9/4}$, pertanto, con flussi in pieno regime turbolento il numero di elementi della griglia risulta eccedere alle capacità di calcolo di qualsiasi calcolatore esistente. La soluzione più adottata per flussi turbolenti è di scomporre le variabili istantanee (velocità e pressione), operazione nota come *decomposizione di Reynolds,* in due componenti, una media e una fluttuante e successivamente mediare l'equazione rispetto al tempo, operazione nota come *media di Reynolds*. Dalle Eq.(II.11) e (II.12), si ottiene un nuovo set di equazioni, le *Reynolds-averaged Navier-Stokes equations* (RANS), che come soluzione hanno i valori medi delle proprietà del flusso nel tempo e nello spazio:

$$\frac{\partial\langle U_i\rangle}{\partial t} + \langle U_j\rangle\frac{\partial\langle U_i\rangle}{\partial x_j} = -\frac{1}{\rho}\frac{\partial\langle p\rangle}{\partial x_i} + \frac{1}{\rho}\left[\mu\left(\frac{\partial\langle U_i\rangle}{\partial x_j} + \frac{\partial\langle U_j\rangle}{\partial x_i}\right) - \rho\langle u_i{}' u_j{}'\rangle\right] + g_i \qquad \text{(II.13)}$$

La struttura dell'Eq. (II.13), dove si è assunto il fluido Newtoniano e incomprimibile, e si è utilizzata la legge di Newton per legare il tensori degli sforzi con la velocità di deformazione del fluido, è molto simile alla Eq. (II.12), eccetto che per il tensore aggiuntivo $d_{ij}^t = -\rho\langle u_i{}' u_j{}'\rangle$, chiamato *tensore degli sforzi turbolenti di Reynolds*, che rappresenta l'interazione tra la componente media e quella fluttuante e i cui elementi non sono noti. L'approssimazione di Boussinesq, Eq. (II.14), suggerisce che tale tensore sia funzione delle componenti medie della velocità, dell'*energia cinetica turbolenta k* e che il trasferimento della quantità di moto avvenga per meccanismi di tipo diffusivo.

$$\frac{\tau_{ij}}{\rho} = -\langle u_i{}' u_j{}'\rangle = \nu_T\left(\frac{\partial\langle U_i\rangle}{\partial x_j} + \frac{\partial\langle U_j\rangle}{\partial x_i}\right) - \frac{2}{3}k\delta_{ij} \qquad \text{(II.14)}$$

Il coefficiente di proporzionalità $\nu_T$ è chiamato *viscosità turbolenta* e la sua modellazione è l'obiettivo di diversi modelli della turbolenza basati sull'approssimazione di Boussinesq. La viscosità turbolenta, esprimibile come $\nu_T = C_\nu u l$, è proporzionale al prodotto tra una velocità $u$ e una lunghezza $l$, caratteristiche della turbolenza, $C_\nu$ è una costante del modello. Poiché $\nu_T$ varia rispetto al tempo e allo spazio, sono necessarie delle equazioni del trasporto addizionali per determinare $u$ e $l$. I modelli più diffusi sono quelli a due equazioni. In essi la velocità caratteristica è espressa mediante l'energia cinetica turbolenta $k$. La lunghezza caratteristica, invece, può essere ricavata dall'equazione del trasporto di una quantità turbolenta generica $\chi$, funzione di $k$ e $l$, espressa secondo una legge di potenza del tipo $\chi = u^\alpha l^\beta$. La "Tabella II.1" riassume le variabili la loro interpretazione:

**Tabella II.1** Variabili principali per la definizione della lunghezza caratteristica turbolenta.

| α | β | χ | Simbolo di χ | Interpretazione di χ |
|---|---|---|---|---|
| 0 | 1 | $l$ | $l$ | Lunghezza caratteristica |
| 1 | -2 | $k/l^2$ | $\omega$ | Vorticosità caratteristica |
| 1/2 | -1 | $k^{1/2}/l$ | $f$ | Frequenza caratteristica |
| -1/2 | 1 | $k^{-1/2}l$ | $\tau$ | Tempo caratteristico |
| 3/2 | -1 | $k^{3/2}/l$ | $\varepsilon$ | Velocità di dissipazione |

La velocità di dissipazione dell'energia cinetica turbolenta $\varepsilon$ è la grandezza più utilizzata e i modelli *k-ε* sono ampiamente implementati in tutti i più comuni software di simulazione numerica di flussi turbolenti. Accanto a questi, anche i modelli *k-ω* hanno un ruolo importante, soprattutto per flussi di tipo *confinati*. La "Tabella II.2" riporta i principali modelli e le loro caratteristiche. Per le equazioni complete e un trattamento più approfondito si rimanda ai paragrafi (§4.2.1-4).

**Tabella II.2** Caratteristiche dei principali modelli turbolenti a due equazioni.

| **Modello** | **Vantaggi** | **Limitazioni** |
|---|---|---|
| Standard k-ε | Stabile, Diffusissimo.<br>Adatto a flussi molto turbolenti | Inaccurato con flussi vorticosi o con repentini cambi di direzione |
| RNG k-ε | Buone prestazioni in flussi vorticosi o con zone caratterizzate da un basso *Re* | Minor stabilità<br>Non adatto per getti circolari |
| Realizable k-ε | Flussi con curvature o grandi sforzi di taglio. | Minor stabilità<br>Maggior costo computazionale |
| k-ω | Ottimi risultati a bassi valori di *Re,* in flussi con forti gradienti di pressione e confinati | Richiede una mesh fitta nei pressi delle pareti |

## II.III Trasporto di grandezze scalari

Simulazioni numeriche di sistemi chimici richiedono la soluzione di equazioni del trasporto di grandezze scalari aggiuntive per descrivere, ad esempio, specie chimiche o la temperatura. Analogamente a quanto fatto per la quantità di moto, applicando l'operazione di *scomposizione di Reynolds* e di mediazione si ottiene un'equazione del trasporto per un sistema turbolento:

$$\frac{\partial(\rho\langle\phi\rangle)}{\partial t}+\frac{\partial(\rho\langle U_i\rangle\langle\phi\rangle)}{\partial x_j}=\frac{\partial}{\partial x_j}\left[\Gamma_\phi\frac{\partial\langle\phi\rangle}{\partial x_j}-\rho\langle u'_i\phi'\rangle\right]+\langle S_\phi\rangle \qquad \text{(II.15)}$$

Ancora una volta il termine $\rho\langle u'_i\phi'\rangle$, la cui definizione è riportata in Eq. (II.16),contenente le fluttuazioni di quantità scalari, è modellato associandolo ad un trasporto di tipo diffusivo, proporzionale al gradiente di concentrazione di scalare mediato secondo Reynolds , la diffusività turbolenta è uguale a $\Gamma_{\phi,T} = \frac{\nu_T}{Sc_T}$ , dove $Sc_T$ è il *numero di Schmidt* turbolento, che per la maggior parte delle applicazioni è compreso tra 0.7 e 1.

$$-\rho\langle u'_i\phi'\rangle = \Gamma_{\phi,T}\frac{\partial\langle\phi\rangle}{\partial x_j} \tag{II.16}$$

## II.IV Modelli multifase

Un sistema multifase si classifica in base al tipo di interazione tra i suoi componenti. Si parla di sistema *segregato* quando le interfacce tra le due fasi sono poche e di grandi dimensioni. In un sistema disperso, invece, una fase, detta *primaria*, è continua, mentre l'altra, la *secondaria*, è in forma di bolle, particelle o gocce. Il parametro chiave per descrivere un sistema disperso, oggetto di questo elaborato, è la frazione in volume $\alpha_k$, che determina la distribuzione all'interno del dominio computazionale delle due fasi:

$$\begin{cases} \alpha_k = \dfrac{\sum_i^{N_k} V_i}{V} \\ \sum_k \alpha_k = 1 \end{cases} \tag{II.17}$$

I modelli multifase per sistemi dispersi sono, a loro volta, riassumibili in modelli *Euleriani-Lagrangiani* e *Euleriani-Euleriani*. Il primo descrive la fase primaria come un continuo e quella secondaria come dispersa, la somma di una grande quantità di singole particelle. Quindi per la fase primaria il punto di vista è stazionario, o euleriano, mentre per quella secondaria è lagrangiano, ovvero l'osservatore si muove con le particelle. Nel caso di un modello euleriano-euleriano, entrambe le fasi sono dei *continui* compenetranti, per i quali le equazioni di continuità e della quantità di moto sono risolte separatamente. In questo modo si va a stimare la frazione volumica media che ogni fase occupa in un preciso punto del dominio. I modelli euleriano-lagrangiano sono molto più onerosi dal punto di vista computazionale rispetto a quelli euleriano-euleriano, per questo motivo quest'ultimi sono spesso preferiti nello studio di sistemi molto complessi, nonostante necessitino di modelli di *chiusura* per descrivere le interazioni tra le fasi. Le equazioni di continuità, Eq. (II.18) e di trasporto di quantità di moto per ogni fase, Eq. (II.19) del sistema multifase sono:

$$\frac{\partial\alpha_k\rho_k}{\partial t} + \frac{\partial(\alpha_k\rho_k U_{i,k})}{\partial x_i} = 0 \tag{II.18}$$

$$\frac{\partial\left(\alpha_k\rho_k U_{i,k}\right)}{\partial t} + \frac{\partial\left(\alpha_k\rho_k U_{i,k}U_{j,k}\right)}{\partial x_j} = -\frac{\partial\alpha_k p}{\partial x_i} + \frac{\partial\alpha_k\tau_{ij,k}}{\partial x_j} + \alpha_k\rho_k g_i + f_{i,k} \tag{II.19}$$

L'ultimo termine dell'Eq. (II.19) rappresenta la quantità di moto scambiata tra i due fluidi all'interfaccia. Tali forze sono comunemente definite come la somma $f_{i,k} = f_{D,i,k} + f_{L,i,k} + f_{VM,i,k} + f_{TD,i,k}$,i cui termini sono riassunti in "Tabella II.3":

**Tabella II.3** Le forze scambiate tra fase primaria e secondaria all'interfaccia.

| | |
|---|---|
| $f_{D,i,k}$ | Forza di trascinamento, dovuta all'attrito tra bolle di gas e fase continua |
| $f_{L,i,k}$ | Forza di "sollevamento", generata dai gradienti di velocità e rotazione della particella |
| $f_{VM,i,k}$ | Forza da "massa virtuale", dovuta all'accelerazione del fluido circostante |
| $f_{TD,i,k}$ | Forza di dispersion turbolenta, dovuta alle fluttuazioni viscose |

La forza di trascinamento (§ 4.1.1) è il termine della somma che più influenza le bolle e la loro forma, quindi anche la quantità di gas disperso nel fluido di processo e il trasporto di materia all'interfaccia. Numerosi sono i modelli che si possono trovare in letteratura per la stima del coefficiente d'attrito $C_D$ che sono implementati nel software utilizzato, tra i quali si possono citare Grace et al. (1978), Tomiyama et al. (1998), Schiller-Neumann (Ansys Theory Guide, 2013).

La forza di "sollevamento" (§ 4.1.2), quella di "massa virtuale" (§ 4.1.3) e di dispersione turbolenta (§ 4.1.4) sono invece state trascurate nelle simulazioni effettuate durante questo lavoro di tesi, in quanto considerate trascurabili rispetto al termine di trascinamento.

# III Dettagli computazionali e condizioni operative

Le simulazioni, su di un dominio computazionale tridimensionale, sono state svolte per due configurazioni di reattore differenti, a singolo e a doppio agitatore, rappresentati in "Figura 3.1" (p. 7) e "Figura 5.2" (p. 34). Per entrambi i casi i risultati sono stati confrontati con dati raccolti durante studi sperimentali sulle due apparecchiature.

## III.I Griglie di calcolo

Per riprodurre il movimento della turbina e del fluido circostante si divide il dominio computazionale in due regioni: quella in movimento, contenente l'agitatore e parte del fluido circostante; quella stazionaria, contenente la maggior parte del volume di fluido e le pareti del reattore. Si possono utilizzare due modelli di *mesh* in movimento: il modello *sliding mesh* (SM) è un metodo intrinsecamente transitorio, nel quale le celle della regione in movimento si spostano di una certa quantità angolare ogni *time step*. ad ogni e della zona; il modello MRF, *multiple reference frame*, la regione in movimento rimane ferma, ma il suo sistema di riferimento ruota con una velocità angolare pari a quella dell'agitatore $2\pi N$. Questo genera forze, del tipo di *Coriolis*, che sono incluse nella soluzione dell'equazioni di Navier-Stokes. Il metodo MRF è stazionario e molto meno oneroso dal punto di vista computazionale rispetto a quello SM. Tuttavia, simulare un processo intrinsecamente variabile nel tempo con un metodo stazionario conduce inevitabilmente ad un certo livello di approssimazione. Inoltre, è importante scegliere in maniera opportuna la posizione relativa tra l'orientazione dell'agitatore e i frangiflutti, poiché questo può influenzare il risultato della simulazione, nonché la sua stabilità.

Il sistema a singolo agitatore è stato simulato utilizzando una mesh tetraedrica con $2.9 \cdot 10^6$ celle, per la quale il numero di celle ottimale è stato determinato mediante analisi della sensibilità, e una griglia strutturata composta da $2 \cdot 10^6$ elementi esaedrici. Per il sistema a doppio agitatore, invece, si è usata solo una mesh tetraedrica, composta da $4.24 \cdot 10^6$.

Le caratteristiche salienti delle griglie di calcolo utilizzate sono riassunte in "Tabella III.1", per una trattazione più approfondita si rimanda a (§ 5.1). Durante il lavoro di tesi sono stati simulati reattori di dimensioni diverse, riassunti in "Tabella III.2". È stato possibile simulare geometrie con dimensioni diverse con le stesse mesh perché si trattava di sistemi geometricamente simili, dunque ottenibili mediante la scalatura proporzionale delle dimensioni.

**Tabella III.1** Caratteristiche delle mesh usate per le simulazioni.

| **Configurazione** | Singolo agitatore mesh tetraedrica | Singolo agitatore mesh esaedrica | Doppio agitatore mesh tetraedrica |
|---|---|---|---|
| **N° elementi** | $2.90 \cdot 10^6$ | $2 \cdot 10^6$ | $4.24 \cdot 10^6$ |
| **Skewness** | 0.67 | - | 0.63 |
| **Orthogonal quality** | 0.42 | - | 0.45 |
| ***Inflation* allo strato limite** | Tre strati | No | Tre strati |
| **Dimensione minima elementi** | 2 mm nella zona MRF, 0.75 mm sulla superficie agitatore 5 mm nella zona statica | Mesh strutturata, 0.75 mm sulla superficie agitatore | 2 mm nella zona MRF, 1.5 mm sulla superficie agitatore 8 mm nella zona statica |

**Tabella III.2** Dimensioni geometriche dei reattori simulati durante il lavoro di tesi.

| **Reattore** | **Agitatori** | **Diametro reattore/agitatore** | **Volume ($m^3$)** |
|---|---|---|---|
| $T_{30}$ | Singolo, Rushton | T= 0.3 m ; D= 0.1 m | 0.021 |
| $T_{60}$ | Singolo, Rushton | T= 0.6 m ; D= 0.2 m | 0.170 |
| $T_{30,R+PB}$ | Doppio, Rushton+ 45° Pitched Blade | T= 0.3 m ; $D_R$=$D_{PB}$= 0.1 m | 0.042 |
| $T_{1m3}$ | Singolo, Rushton | T= 1.1 m ; D= 0.3 m | 1 |
| $T_{50m3}$ | Singolo, Rushton | T=4 m ; D = 1.3 m | 50 |

## III.II Modelli, metodi di calcolo e condizioni al contorno

Per il sistema monofase, sia con acqua sia con fluido non-Newtoniano, si sono eseguite simulazioni in stato stazionario, principalmente con il modello *Realizable k-ε*, con algoritmo

risolutivo *accoppiato* (*Pressure-Velocity Coupling*), con fattori di sotto-rilassamento *pseudo-transient* attivati, per migliorare la stabilità e la convergenza della soluzione. Questi risultati sono stati comparati con quelli ottenuti utilizzando il modello *Standard k-ε* e l'algoritmo "segregato" *SIMPLE*. Riguardo la discretizzazione, lo schema *upwind* del secondo ordine è stato usato nelle mesh non strutturate, il metodo *QUICK* per la griglia strutturata. Per la convergenza della soluzione si è monitorato il valore di un parametro durante la simulazione e i residui normalizzati delle equazioni. Quando tale parametro risultava inferiore a una soglia stabilita e i residui normalizzati erano inferiori a $1 \cdot 10^{-6}$ la soluzione è stata considerata convergente. Le condizioni al contorno applicate sono: *non-scivolamento* alle pareti del reattore e degli organi meccanici, ovvero velocità del fluido nulla; condizione di *simmetria*, ovvero nessuno sforzo, sulla superficie superiore del dominio computazionale, considerato come un livello di fluido sottostante al pelo libero e quindi privo di interfaccia. Infine, su tutte le pareti, per soddisfare le leggi fisiche che regolano il profilo di velocità è stato utilizzato il modello *enhanced wall treatment*.

Per il sistema multifase sono state eseguite simulazioni con modello euleriano-euleriano sia in modalità stazionarie sia transitorie. Il sistema gas-liquido in oggetto tende facilmente all'instabilità durante il calcolo della soluzione, costringendo ad usare metodi di discretizzazione e modelli meno stringenti: discretizzazione *upwind* del primo ordine, algoritmo SIMPLE per la modalità in transitorio. Nel caso stazionario l'algoritmo utilizzato è stato il *Coupled*, abilitando la modalità *pseudo-transient* e impostando il numero di *Courant* a valori inferiori a $1 \cdot 10^{-5}$. Entrambi i modelli *Standard* e *Realizable k-ε* sono stati utilizzati. Le condizioni al contorno sono le stesse del sistema monofase con l'aggiunta della condizione di *scivolamento* del gas sulle pareti e quella riguardante la superficie superiore del reattore, dove il gas fuoriesce. Quest'ultima condizione è importante per garantire il bilancio massico della fase gas. Tre condizioni al contorno sono state testate: *degassing*, che definisce una superficie di *outlet* solo per la fase gassosa, mentre è un contorno privo di sforzi per la fase primaria; *pressure outlet*, che impone una condizione sulla pressione statica, con una frazione di gas di ricircolo (*backflow*) pari a 1; come terza opzione, si è provato ad aggiungere un volume computazionale extra, di solo gas, nella parte superiore, la cui sezione di testa è stata impostata come *pressure outlet*. Quest'ultima condizione, molto comune nelle simulazioni di colonne a bolle, garantisce la conservazione della fase secondaria ma aggiunge un costo computazionale elevato. Infine, per l'ingresso del gas dal distributore omogeneo, ne sono state impostate la velocità, corrispondente ad una portata di 1 $m^3/h$, e la frazione volumica, circa 0.5. In questo modo il valore della velocità in ingresso risulta essere il doppio della velocità superficiale desiderata.

## III.III Grandezze confrontate

Le grandezze valutate per verificare l'accuratezza delle simulazioni e valutare l'idrodinamica globale e la miscelazione sono il *numero di potenza* e il *tempo di miscelazione*.

Il numero di potenza è stato calcolato con due definizioni differenti:

$$N_{p,\Gamma} = \frac{2\pi\,\Gamma}{\rho N^2 D^5} \tag{III.1}$$

$$N_{p,\varepsilon} = \frac{\int_V \rho\varepsilon \,\mathrm{d}V}{\rho N^3 D^5} \tag{III.2}$$

Nell'Eq. (III.1) $N_p$ è in funzione della coppia $\Gamma$ misurata sull'asse rotante, nell' Eq. (III.2) lo si calcola dalla velocità di dissipazione dell'energia cinetica turbolenta $\varepsilon$. La prima definizione è molto usata nelle simulazioni CFD in quanto molto affidabile, mentre la seconda dipende

dall'accuratezza della stima della turbolenza da parte del modello. È chiaro che se $N_{p,\varepsilon}$ è molto simile a $N_{p,\Gamma}$ e al valore sperimentale la simulazione avrà descritto l'idrodinamica del sistema con maggiore accuratezza.

Il tempo di miscelamento è stato calcolato simulando la miscelazione di un tracciante, rappresentato da una grandezza scalare (detta *user defined scalar*, UDS), all'interno del reattore. Usando il metodo della varianza, Eq. (III.3), il tempo impiegato dallo scalare per raggiungere una concentrazione nell'intero volume la cui varianza è minore o uguale al 5% si definisce $\theta_{95}$.

$$\log(\sigma^2) = \log\left[\frac{1}{N_{cells}}\sum_{i=1}^{N_{cells}}\left(\frac{C_i}{C_\infty}-1\right)^2\right] \tag{III.3}$$

## III.IV La reologia complessa

Il comportamento reologico del *brodo* di fermentazione è stato riprodotto utilizzando le soluzioni acquose di due idrocolloidi: la gomma di Xantan (XG) e la Carbossimetil Cellulosa (CMC). I parametri reologici, del modello reologico a legge di potenza, misurati per queste soluzioni sono stati usati durante le simulazioni per determinare numero di potenza e tempo di miscelamento, i quali a loro volta sono stati confrontati con i dati sperimentali.

La modifica del modello turbolento per tener conto del comportamento pseudoplastico dei fluidi è stata fatta in due modi: nel primo con impostazioni interne al software di simulazione, nel secondo attraverso una funzione scritta appositamente per modificare il metodo di calcolo della viscosità da parte dell'algoritmo. Il software Ansys Fluent permette di modificare la reologia cambiando il modello della viscosità, da costante a legge di potenza, e quindi di inserire i parametri, citati in (§ II.I). La viscosità è funzione dello shear-rate $\dot{\gamma}$, che è calcolato dalla definizione $\dot{\gamma} \equiv \sqrt{2(\boldsymbol{D}:\boldsymbol{D})}$. $\boldsymbol{D}$ è il tensore degli sforzi viscosi, le cui componenti sono le $d_{ij}$ già introdotte, e dipende dalle velocità media del flusso turbolento. Con l'intenzione di verificare se fosse possibile valutare la viscosità da un parametro locale si è utilizzata la definizione dello shear-rate in un reattore agitato, data da (Sánchez Pérez et al. 2006), Eq. (III.4). Alla potenza $P$ è stata sostituita l'espressione $P = \rho V \varepsilon$ e $\mu_a = K\dot{\gamma}^{n-1}$, per ottenere l'Eq. (III.5), dove $\varepsilon_i$ è la velocità di dissipazione calcolata per ogni cella.

$$\dot{\gamma} \equiv \left(\frac{1}{\mu}\frac{P}{V}\right)^{\frac{1}{2}} \tag{III.4}$$

$$\dot{\gamma} \equiv \left(\frac{\rho\varepsilon_i}{K}\right)^{\frac{1}{n+1}} \tag{III.5}$$

L'uso di quest'ultimo metodo si giustifica con il fatto che a scale di grandezza elevata, il calcolo di $\dot{\gamma}$ dai gradienti medi di velocità tende a non essere più accurato, a causa delle maggiori eterogeneità.

## III.V Simulazioni del sistema fed-batch e particle tracking

La valutazione dei gradienti di substrato durante la fermentazione e la circolazione della biomassa nel bioreattore è importante per determinare, con un approccio *scale-down*, gli effetti che questi due fenomeni hanno sul microorganismo e sul suo metabolismo. La distribuzione di concentrazione di glucosio è implementata introducendo uno specie scalare, con le stesse

proprietà fisiche del glucosio, all'interno di una simulazione, il cui campo di moto sia già stato risolto e "congelato", e simulandone il trasporto. Sono state introdotte una *sorgente* di scalare nella sezione superiore, che rappresenta l'inlet di substrato, e in ogni cella restante di volume di fluido è stata implementata la cinetica di consumo di glucosio, Eq. (III.6), che funge da *sorgente negativa* di scalare.

$$\frac{dS}{dt} = -X \cdot \left[ \frac{\mu_{max} \cdot S \cdot y}{Y_{X,S} \cdot (K_{S,\mu} + S)} + \frac{S \cdot (q_{P,max} \cdot (1 - y) + q_{P,min})}{Y_{P,S} \cdot (K_{S,P} + S)} \right] \quad \text{(III.6)}$$

Calcolata la distribuzione di substrato, che dipende dalla concentrazione di biomassa X contenuta nel reattore, sono state definite due zone, una denominata ricca, ad alta concentrazione in glucosio per la quale la biomassa cresce, e una povera, nella quale il microorganismo produce enzima. La circolazione dei microrganismi tra le due aree è stata implementata con una simulazione di tipo lagrangiano che segue le traiettorie di particelle solide discrete, rappresentative di ammassi di cellule. Queste particelle sono definite come prive di massa (massless) e si muovono in maniera casuale (random walk), seguendo il campo di moto all'interno del reattore. Definendo una sezione di campionamento, per esempio l'area ricca in substrato, si può costruire una funzione di distribuzione della frequenza di attraversamento di tale regione e quindi ottenere dati circa il tempo medio trascorso dalle cellule nella zona ricca, piuttosto che la quantità di biomassa che risiede in tale area. Tutte queste informazioni possono, infine, essere utilizzate in laboratorio biologico per determinare gli effetti sulla resa in enzima.

# IV Simulazioni CFD e risultati

In questo capitolo sono riassunti i risultati principali delle simulazioni effettuate durante il lavoro di tesi. Un'esposizione più completa si trova al capitolo §6.

## IV.I Validazione del modello turbolento

La convalida del modello turbolento è stata effettuata simulando il reattore $T_{30}$ (informazioni geometriche in "Tabella III.2") con il modello *Realizable k-ε* con acqua. La velocità dell'agitatore *N* (200, 400, 680, 800 rpm) comprende il regime turbolento, che per un reattore agitato parte da *Re>4000.*

Il *numero di potenza* è stato calcolato dalla soluzione di simulazioni in modalità stazionaria *pseudo-transitoria* con entrambe relazioni di Eq. (III.1) e (III.2), e queste sono state confrontate con il valore ricavato sperimentalmente, $N_{P,exp}$= 3.93. Il grafico in "Figura 6.1" (p. 49) mostra che i valori ricavati dalla simulazione sono consistenti con il dato sperimentale. In particolare, l'accuratezza di $N_{p,\varepsilon}$ indica che il modello, per condizioni di regime turbolento ben sviluppato, è in grado di predire l'idrodinamica del sistema quantificando correttamente l'energia dissipata nel sistema.

Utilizzando i campi di moto precedentemente ottenuti si è simulato, in modalità transitoria, il trasporto dello UDS per ricavare il *tempo di miscelamento*. In una piccola porzione di volume computazionale si è imposto una concentrazione unitaria di UDS, "l'iniezione" di tracciante in "Figura 6.2" (p. 50). Le proprietà fisiche dello scalare sono implementate con una *user defined function* (UDF), riportata in "Appendice B". Lo scalare si diffonde nel dominio computazionale

seguendo l'idrodinamica del sistema. Il $\theta_{95}$ calcolato è confrontato con quello ricavato dalla relazione di *Ruszkowski* (Grenville et al. 1992), Eq. (6.1), specifica per turbine Rushton in reattori agitati con T=H. Nel grafico di "Figura 6.3" (p. 51) si confrontano i valori di $\theta_{95}$ calcolati: con la relazioni empirica, simulando con *Realizable k-ε* (che risulta il modello più preciso) e con *Standard k-ε*. L'errore è basso per entrambi i modelli, non superiore al 10%.

## IV.II Simulazioni con fluidi non-Newtoniani

Per la convalida del modello turbolento con fluidi non-Newtoniani è stato simulato il sistema a doppio agitatore $T_{30,R+PB}$, in quanto unico sistema per il quale erano stati ricavati dati sperimentali per $N_P$ e $\theta_{95}$. I fluidi simulati sono acqua, la soluzione acquosa di CMC 0.5% wt e quella di XG 0.25% wt. Le modalità sono le stesse descritte per il sistema monofase con acqua; la viscosità è stata modificata utilizzando il metodo proposto dal software Ansys Fluent, come descritto nel paragrafo (§5.4). I risultati, riportati nei grafici di "Figura 6.4" (p. 52 – 53), indicano che vi è coerenza con quanto ottenuto per il sistema a singolo agitatore. Il numero di potenza, ricavato con entrambe le definizioni non si discosta dal dato sperimentale. Questo non sorprende perché la maggior parte dell'energia è dissipata nella zona limitrofa all'agitatore, area in cui il fluido, a causa del suo comportamento pseudoplastico, presenta viscosità molto simili a quelle dell'acqua. Solo a basse velocità, ossia 200 rpm, l'errore è maggiore, indicando che il sistema è più stagnante, e quindi meno turbolento.

L'analisi dei risultati ottenuti per il tempo di miscelamento, illustrati in "Figura 6.6" (p. 54), conferma che il modello turbolento è in grado di prevedere che, all'aumentare della velocità di agitazione, il $\theta_{95}$ diminuisce. Tuttavia, non permette di calcolare valori che siano prossimi a quelli sperimentali, se non a velocità elevate. Tali dati indicano che per basse velocità ($N$=200, 400 rpm) il sistema è pienamente turbolento solo nelle regioni adiacenti all'agitatore, a dimostrazione del fatto che i tempi di miscelamento sono molto sottostimati, mentre è fortemente stagnante in prossimità delle pareti, sul fondo e in testa al reattore. Il modello – data l'ipotesi che il regime turbolento sia pienamente sviluppato in ogni parte del reattore – sovrastima il livello di miscelazione dello stesso. A velocità maggiore, $N$= 800 rpm, il sistema è molto più turbolento e infatti il valore sperimentale e quello simulato concordano.

La modifica del metodo di calcolo dello shear-rate, utilizzando i valori locale di ε, come proposto in (§5.4 .2 e §III.IV), è stata ottenuta programmando una UDF, riportata in "Appendice C". Le simulazioni sono state realizzate sulla mesh strutturata, scalandola fino a ottenere un reattore dal volume di 50 $m^3$. Si sono impostate le condizioni operative in modo da avere lo stesso valore di *potenza specifica dissipata* nel sistema $T_{30}$ a velocità $N$= 680 rpm, ovvero $P_0/V$ = 2.7 $kW/m^3$. Questo valore rientra nel range comunemente usato in applicazioni industriale, che è compreso tra 2-3 $kW/m^3$ a 5-6 $kW/m^3$. Le immagini in "Figura 6.12" (p. 58) mostrano i profili di *viscosità effettiva*, la cui definizione è la somma tra la *viscosità turbolenta* e quella *molecolare*, quest'ultima calcolata sia con il metodo standard di Ansys Fluent (a sinistra) sia con quello proposto in questo elaborato (a destra). Il confronto tra le due illustrazioni mostra che la differenza tra i metodi è trascurabile e ciò è dovuto al fatto che la $\mu_T$ è molti ordini di grandezza superiore a $\mu_{mol}$, almeno a questo livello di energia fornita.

## IV.III Simulazioni multifase

Le simulazioni multifase hanno richiesto molto tempo per la ricerca di una configurazione che fosse numericamente stabile e con dati coerenti con le leggi della Fisica. Per questa ragione i risultati presentati sintetizzano i tentativi esperiti. Le impostazioni del sistema multifase sono:

modello euleriano-euleriano, aria dispersa in acqua con un diametro delle bolle costante e pari a $d_b$= 0.003 m. I modelli di turbolenza testati sono *Realizable k-ε* e *Standard k-ε* con l'opzione multifase *"dispersed"* abilitata, per tenere conto della notevole differenza di densità tra i due componenti. Le interazioni tra le due fasi considerate, per ragioni di stabilità e di riduzione dei tempi di calcolo, sono state limitate a tensione superficiale, σ = 0.073 Nm, *virtual mass* e *drag law*. La superficie del diffusore di gas è stata definita come un *velocity inlet*, pertanto veniva richiesto di scegliere la velocità di ingresso della fase secondaria e la sua frazione in volume. La velocità è stata ricavata dalla portata volumica sperimentale, pari a $Q_G$= 1 $Nm^3/h$, dalla formula in Eq. (IV.1):

$$v_{g,sparger} = \frac{Q_g}{A_{sparger} \cdot \alpha_{g,IN}} \tag{IV.1}$$

Con $A_{sparger}$ si indica superficie del diffusore da cui il gas fuoriesce e $\alpha_{g,IN}$ è la frazione volumica di gas nel flusso in entrata al sistema.

Il primo sistema indagato è stato il reattore $T_{30}$ con velocità di agitazione uguali a 400, 800, 1000 rpm, scelte perché, nel corso delle sperimentazioni, si è osservato che il sistema risultava pienamente disperso. La sezione di uscita del gas è stata impostata come una superficie di *degassing*. Inizialmente si è interpolato un *flow-field*, precedentemente calcolato con un'altra simulazione, in modo da ridurre i tempi computazionali. La drag-law Grace (§4.4.1) è stata la scelta iniziale. Le simulazioni sono state condotte sia in modalità stazionaria, sia in modalità transitoria, con passo temporale crescente da $1 \cdot 10^{-6}$ s a $1 \cdot 10^{-3}$ s. Le simulazioni in steady-state sono immediatamente andate a divergenza come anche quelle in modalità transitoria, al raggiungimento di un passo temporale di $1 \cdot 10^{-3}$ s. Si è ritenuto che la causa di questa forte instabilità fosse l'interpolazione di soluzioni precedentemente calcolate, pertanto questa pratica è stata abbandonata nelle prove successive.

Per agevolare la stabilità, nel secondo set-up investigato si è optato per uno schema di discretizzazione del tipo UDS del primo ordine. Il singolo time-step si è considerato giunto a convergenza quando i residui normalizzati dell'errore erano inferiori a $1 \cdot 10^{-3}$. Tutto ciò a svantaggio dell'accuratezza della soluzione. Ogni time-step veniva risolto con un massimo di 50 iterazioni e ogni simulazione ha avuto la durata media di 72h nel centro di calcolo. Ad ogni cambio di time-step il sistema diventava fortemente instabile e perdeva accuratezza. Il tempo "reale" raggiunto non superava i 6 secondi. I dati calcolati sono risultati non corretti, con un *hold-up* di gas dell' 1%, a fronte di un valore sperimentale medio del 2.7%, e un $N_{P,G}$ con valori compresi tra 0.9 e 1, a fronte di un valore atteso che fosse 0.5 – 0.8 volte quello monofase, dunque attorno a $N_{P,G}$ =1.95 – 3.2.

Nella terza serie di tentativi il sistema di simulazioni precedenti è stato modificato nel modo seguente: il modello di drag-law è stato cambiato con quello proposto da Tomiyama (§4.4.1), già validato presso IFPEN per le colonne a bolle; l'interazione tra le due fasi dovuta alla forza *virtual mass* è stata disabilitata, in quanto noto fattore di instabilità; la condizione al contorno della sezione di testa del reattore è stata modificata. La parte superiore del dominio computazionale è stata addizionata di un volume extra, la cui frazione volumica di gas è stata imposta pari a 1. La superficie di uscita è stata definita con la condizione di *pressure outlet*. La mesh della parte aggiuntiva è stata realizzata con celle più grossolane rispetto al resto del dominio, per limitare l'onere computazionale. Nonostante i cambiamenti apportati i risultati si sono rivelati errati. In particolare, l'aria restava intrappolata nel reattore, formando ampie cavità nelle regioni adiacenti e sottostanti all'agitatore e intorno all'asse rotante. Inoltre, sacche di gas irrealistiche intrappolate nel loop principale del liquido impedivano la normale coalescenza,

come illustrato nelle immagini di "Figura 6.14" (p. 61). L'hold-up di gas previsto dalla simulazione, compreso nel range 0.7 – 1%, risultava ancora troppo basso rispetto a quanto atteso. Si è supposto che i valori del numero di potenza calcolati, con valori così bassi, siano da attribuire alla grande quantità di gas che, accumulandosi attorno all'agitatore, porta alla riduzione dell'energia fornita al sistema. Le origini di queste problematiche sono attribuibili a molti fattori: la mesh, il modello turbolento, la drag law e le dimensioni della regione MRF troppo ampia.

Infine, l'ultima configurazione esperita ha dato risultati più coerenti con i dati sperimentali: si è simulato il reattore $T_{60}$, con modello *Standard k-ε* (perché più stabile), la drag law scelta è Grace, a cui si è aggiunto il coefficiente di modifica di Brucato (§4.4.1). La regione MRF è stata ridotta di dimensioni. Le simulazioni sono state eseguite inizialmente con modalità steady-state per inizializzare il sistema, e poi proseguite in modalità transitoria, con un aumento del time-step "adattativo", partendo da $1 \cdot 10^{-6}$ s a 0.02 s. Il flusso di gas è stato progressivamente aumentato durante la simulazione, partendo da un valore molto basso fino a raggiungere il valore sperimentale di 1 $Nm^3/h$. Infine, la mesh è stata raffinata sulla superficie superiore del diffusore di gas con celle di dimensioni caratteristiche pari a 0.001 m. La sezione superiore è stata impostata con la condizione di *degassing*. La qualità dei risultati è molto migliorata, con una distribuzione di gas realistica, come dimostrato dall'immagine di "Figura 6.15" (p. 62). La "Tabella (IV.1)" mostra i valori di hold-up e energia dissipata confrontati con quelli sperimentali:

**Tabella IV.1** Confronto tra dati sperimentali e simulazioni CFD per il sistema multifase.

| | $\alpha_G$ (-) | $P_G/P_0$ |
|---|---|---|
| **Exp.** | 2.7% | 0.676 |
| **CFD** | 2.4% | 0.684 |

## IV.IV Simulazioni sistema fed-batch e particle tracking

Le simulazioni sul sistema *fed-batch* sono state eseguite principalmente sui reattori $T_{60}$ e $T_{1m3}$, in condizioni operative tali da avere la stessa potenza specifica dissipata, $P_0/V$ = 2.7 $kW/m^3$. Il metodo seguito per la simulazione della diffusione del glucosio (con modalità transitoria) è quello esposto in (§III.V e §5.5.1). La concentrazione iniziale di biomassa $X$ è stata considerata pari a 5, 10 e 20 $kg/m^3$. I flow-field utilizzati provengono da simulazioni già risolte con acqua, CMC 0.5% wt e XG 0.5% wt. Il substrato alimentato al reattore con portata specifica $q_{s,IN}$ = 0.03 kg *zucchero*/ kg *biomassa*/hr che, per esempio, per il $T_{60}$ consiste in una portata di soluzione acquosa $Q_{sugar} = 5.61 \cdot 10^{-8}$ $m^3/s$, è indubbiamente troppo piccola per influenzare il campo di moto, quindi è corretto utilizzare un flow-field già risolto. Per determinare il tempo caratteristico del processo di consumo del substrato e il passo temporale da utilizzare si è risolta l'Eq. (III.6) su Microsoft Excel. Il grafico in "Figura 6.16" (p. 63) riporta la soluzione dell'equazione per i tre valori di biomassa iniziale scelti, riferiti al reattore $T_{60}$. Si può facilmente verificare che il processo di consumo di substrato ha dei tempi caratteristici dell'ordine di grandezza delle ore, mentre la miscelazione alle condizioni operative scelte ha un $\theta_{95}$ dell'ordine dei secondi. Pertanto, si è supposto che la regione da considerare "ricca" in substrato ammontasse ad una frazione molto piccola dell'intero volume.

I risultati delle simulazioni, su scale diverse e con fluidi differenti, come illustrato nelle "Figure 6.17-18" (p. 94) mostra che lo zucchero si concentra maggiormente nella parte superiore del reattore, in particolar modo nel volume adiacente al punto di alimentazione e intorno all'asse di rotazione. Nelle zone più stagnanti, ovvero intorno alle pareti e sul fondo la quantità di substrato è molto bassa. Questa distribuzione è comunque in linea con il fatto che la turbina Rushton tende a dividere il reattore in due regioni: quella soprastante l'agitatore, con un campo di moto molto vigoroso, quindi meglio miscelata e quella sottostante, più stagnante. Queste due parti sono tendenzialmente segregate tra loro e questo fenomeno si intensifica con l'aumentare della viscosità del fluido. La costruzione di una *funzione di densità di probabilità* (PDF) relativa alla concentrazione di substrato, mostrata in "Figura 6.19" (p. 65), indica che quest'ultima segue una distribuzione del tipo *log-normale*, confermando le ipotesi iniziali fatte sul sistema.

Infine, si è provato a implementare il metodo del *particle tracking*, senza ancora applicarlo al sistema con il substrato. Una semplice regione cilindrica, all'altezza dell'agitatore, è stata separata dal resto del dominio computazionale e usata come volume di campionamento per determinarne la frequenza di attraversamento. Si sono dunque simulate le traiettorie di 40000 particelle discrete "prive di massa" (*massless*) in libero moto casuale (*free random walk*). Si è poi costruito un grafico rappresentante la frequenza di attraversamento della regione campione, presentato in "Figura 6.21" (p. 66). Ancora una volta il grafico richiama una distribuzione log-normale, ad indicare che la maggior parte delle particelle attraversa l'area campione per tempi molto brevi, 1 – 3 secondi. Questa tecnica, se correttamente implementata può fornire utili informazioni per un futuro studio sugli effetti metabolici della concentrazione di substrato che la biomassa può incontrare durante il processo di fermentazione.

# V Conclusioni

Nel presente lavoro sono state svolte simulazione CFD monofase e multifase di un bioreattore agitato con il codice commerciale Ansys Fluent 17.2. I risultati numerici sono stati confrontati con correlazioni empiriche in letteratura e dati sperimentali precedentemente raccolti per due apparecchiature dal diametro di 0.3 m e 0.6 m. L'oggetto del lavoro svolto è stato quello di trovare i modelli turbolenti che meglio descrivessero l'idrodinamica e il miscelamento del sistema al crescere delle dimensioni, con lo scopo di prevedere accuratamente le eterogeneità, che si creano durante le operazioni di miscelazione, in tempi di calcolo ragionevoli.

Inizialmente, l'idrodinamica è stata validata per un sistema monofase con acqua, singolo agitatore e serbatoio con diametro e altezza uguali, in regime turbolento pienamente sviluppato. Nel paragrafo (§6.1) confrontando i dati di *numero di potenza* $N_p$ e *tempo di miscelamento* $\theta_{95}$ ricavati simulando il reattore con i modelli turbolenti *Standard k-ε* e *Realizable k-ε*, è emerso che entrambi sono in grado di predire accuratamente la miscelazione nel reattore e l'energia dissipata. In particolare, il primo dei due modelli citati è quello che commette l'errore minore, sebbene sia più oneroso in termini di tempo computazionale. La ragione risiede nel fatto che questo modello è stato ricavato imponendo dei vincoli di "veridicità fisica" che ben si applicano al sistema in esame, dominato da moto vorticoso.

Il *brodo* fermentativo reale ha un comportamento reologico non-Newtoniano, di tipo pseudoplastico. Le simulazioni sono state eseguite usando soluzioni acquose degli idrocolloidi Carbossimetil Cellulosa ( 0.5 % wt) e Gomma di Xantan (0.25% e 0.5% wt) come fluidi sperimentali. Il modello reologico scelto è quello della legge di potenza; i parametri $K$ e $n$ usati erano precedentemente stati ricavati da studi sperimentali presso IFPEN. La modificazione della reologia è stata realizzata con due metodi: uno presente di *default* nel software di simulazione, basata sui valori medi di velocità del flusso turbolento, l'altro implementato mediante una UDF proposta dal gruppo di lavoro, basata su grandezze locali. I risultati, nella sezione (§6.2), mostrano che il metodo di *default* del software è in grado di predire con un buon grado di precisione l'energia dissipata nel sistema, tuttavia è molto impreciso riguardo alla miscelazione, sottostimando ampiamente i valori sperimentali di tempo di miscelamento quando il sistema è molto stagnante. Questo fenomeno è, ad ogni modo, dovuto al fatto che tutti i modelli $k$-$\varepsilon$, per ipotesi, tendono a sovrastimare la turbolenza del sistema. Il secondo metodo ha dimostrato che in un sistema a elevati livelli di turbolenza il calcolo della viscosità molecolare da variabili locali, invece, ha poca influenza sulla simulazione numerica dell'idrodinamica globale. Tuttavia, potrebbe avere una maggiore influenza su un sistema multifase.

Il modello multifase euleriano-euleriano è stato applicato alle diverse simulazioni multifase svolte con differenti modelli turbolenti, metodi e impostazioni per trovare quale fosse la migliore configurazione in termini di accuratezza della soluzione, stabilità della simulazione e tempo computazionale. I risultati, presentati in (§6.3), mostrano l'importanza della scelta nel modello della drag-law e l'influenza che l'uso del *coefficiente di modificazione di Brucato* ha avuto nell' ottenere una simulazione stabile e con una buona soluzione, in termini di hold-up di gas nel reattore e di potenza dissipata. Inoltre, si è dimostrata la grande influenza che possono avere le condizioni al contorno, le dimensioni della zona MRF e la qualità della griglia di calcolo sull'esito della simulazione.

Infine, il sistema fermentativo fed-batch è stato simulato per analizzare la distribuzione di substrato all'interno del reattore. Inoltre, è stato investigato un metodo per tracciare le traiettorie di particelle discrete in moto nel sistema per acquisire informazioni circa il moto dei microrganismi da fornire a eventuali studi futuri per determinare gli effetti che i diversi livelli di substrato hanno sul metabolismo. I risultati raccolti in (§6.4) confermano l'ipotesi che la distribuzione di substrato consente di distinguere nel fermentatore regioni ben definite, rispettivamente ricche e povere di glucosio, la cui distribuzione segue l'andamento log-normale. Implementato il metodo di tracciamento delle traiettorie di particelle discrete, simulate con modello lagrangiano, si è costruito un grafico di distribuzione di frequenza con cui le particelle attraversano la regione "campione" definita all'interno del dominio computazionale.

Ulteriori studi approfonditi dovranno concentrarsi sul sistema multifase, in particolare: riuscire ad ottenere simulazioni stabili e convergenti con schemi di discretizzazione del secondo ordine per migliorare la precisione dei risultati; verificare l'influenza sul sistema di portate di gas superiori, con velocità di gas superficiali nel range di $U_G = 8 – 15$ m/s, che più si avvicinano alle condizioni operative in applicazioni industriali; analizzare l'effetto che la reologia complessa ha sul coefficiente di attrito $C_D$, sulla forma e la dimensione delle bolle e quindi sull'hold-up di liquido e il trasporto di massa tra le due fasi. Inoltre, un maggiore approfondimento dovrebbe essere focalizzato all'implementazione del metodo di *particle-tracking* per l'analisi delle traiettorie e del metabolismo dei microorganismi, con determinazione rigorosa delle funzioni di distribuzione di substrato e di frequenza di passaggio nelle regioni a differente concentrazione di glucosio, per fornire dati a studi sul metabolismo della biomassa.

# 1 Introduction

This thesis presents the internship experience carried out in Institut Français du Petrol – Energie Nouvelle (IFPEN) based in Solaize, Lyon, in the R12 Departement – Process conception and modelling, during the period March – August 2018.

This work is part of a wider project aimed to the production of second-generation biofuels, namely bioethanol, from lignocellulosic materials. The aim of this work is to numerically simulate the hydrodynamics inside stirred tank bioreactors, used to produce enzymes, to predict mixing performances, heterogeneities formations and substrate distribution in case of non – Newtonian fluids and gas – liquid multiphase systems. The work will present the following structure:

In chapter 2 the framework of the study will be exposed, explaining the increasing interest for biofuels, in particular with bioethanol, and the main difficulties encountered in the production process will be outlined. Finally, the process developed at IFP Energie Nouvelle will be presented;

In chapter 3 some theoretical aspects important to describe turbulent mixing in stirred tank reactors will be presented, with particular interest in global hydrodynamic parameters for single-phase and multiphase systems, with Newtonian and non-Newtonian fluids;

In chapter 4 will present numerical models for turbulence and multiphase systems. Some theoretical aspects of the methods used for numerical simulation will be presented as well;

Chapter 5 will present numerical simulations methods and set-up for single-phase, multiphase systems, with water and non-Newtonian fluids, including the methods used to modify the rheology. Moreover fed-batch system simulations methods and set-up will be outlined;

Chapter 6 will present the results of the simulations, analyse and compare them to experimental data of the system available from previous studies;

Chapter 7 will finally report a global synthesis of the results obtained and propose the direction of further investigations on the matter.

# 2 Bibliographic research

In a general context of a worldwide increasing energy demand, it is necessary to find a more sustainable alternative to fossil fuels such as oil, gas and coal, still the most used form of energy resources. The reasons behind this shift are mainly two (Kennes and Veiga, 2013):the production of greenhouse gases, carbon dioxide above all, whose accumulation in the atmosphere cause an increase of Earth temperature and thus a rise of the sea level; the expected depletion of fossil fuel resources during the next decades.

Biofuels produced from renewable or waste biomass can help decreasing $CO_2$ emissions both by reducing the use of fossil fuels and by the carbon dioxide depletion occurring during photosynthesis in plants growth. Currently bioethanol, along with biodiesel, is one of the most studied and industrially promising of such alternatives.

## 2.1 Bioethanol

Ethanol from renewable resources, inaccurately called *bioethanol*, is produced by alcoholic fermentation of simple sugars, mainly monosaccharides, and it could be classified in three different categories based on the source materials (Azadi et al., 2017; Joshi et al., 2017):

First generation bioethanol is obtained either from transformation of amylaceus cereals (corn, wheat), whose starch is converted into glucose, plants who are raw material for sugar production (sugarcane or sugar beet) or from by-product of sugar industry (molasses, beet pulp). The main drawback of this process is the use of crops that would be destined to meet food demand.

Second generation biofuels use non-food biomasses, namely lignocellulosic materials. These raw materials come from: agricultural wastes, which are the most abundant renewable resource on the planet and homogeneously spread worldwide; forest products or livestock wastes or dedicated energy grasses. These raw materials must be pre-treated, namely hydrolysed, to convert complex lignocellulosic components (long chain carbohydrates) into simpler sugars.

Third generation bioethanol from microalgae which can give much higher quality yields with respect to the previous ones, with the advantage of several choices in raw materials and growing media. A comparison between the first and second-generation processes is shown in “Figure 2.1”:

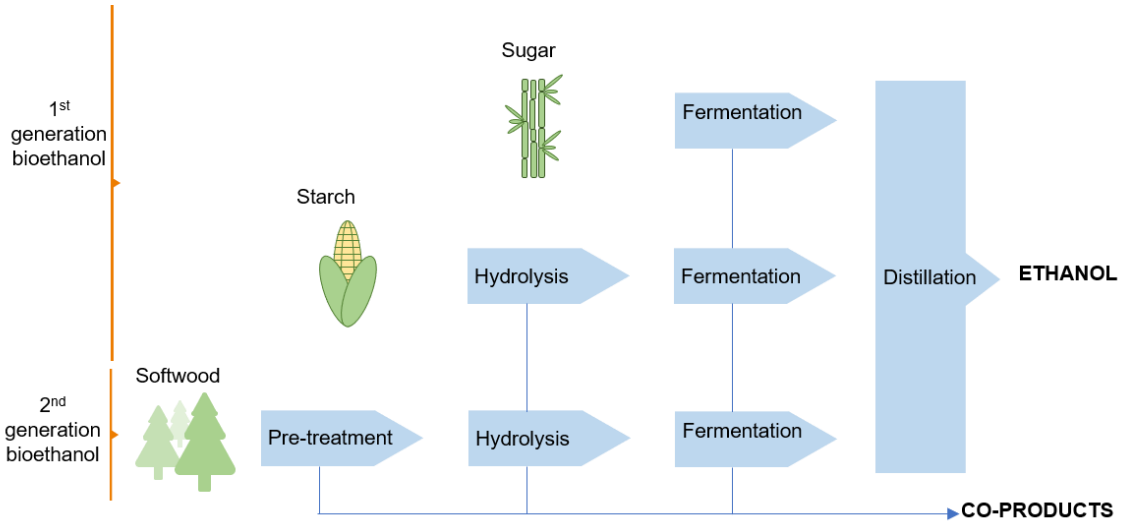


**Figure 2.1** Production processes for first- and second-generation bioethanol.

This thesis will focus on second generation bioethanol and in particular on hydrolyzation pre-treatments required by non-food biomasses prior to alcoholic fermentation.

## 2.2 Lignocellulosic biomass treatments

Lignocellulosic materials main components are polymeric carbohydrates (cellulose and hemicellulose) and the aromatic polymer lignin (Brandt et al., 2013) as shown in "Figure 2.2":

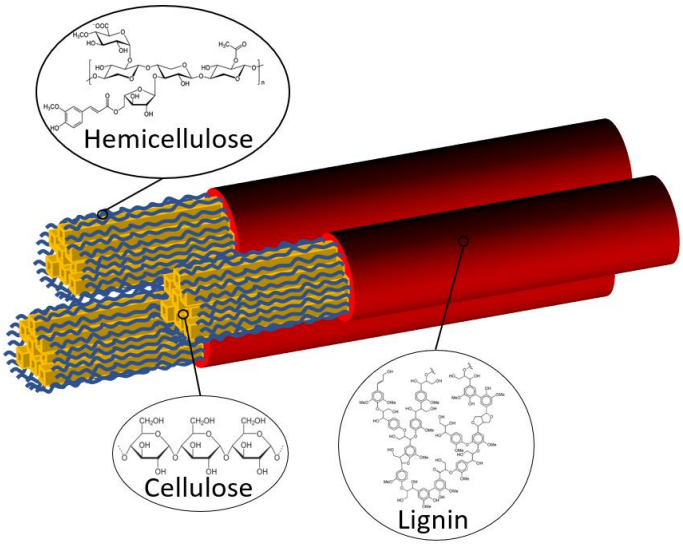


**Figure 2.2** Spatial structure of lignocellulosic materials (Brandt et al., 2013).

The monomers that compose cellulose and hemicellulose, glucose the former, mainly monosaccharides (glucose, mannose, galactose, xylose, arabinose) the latter, are the main source of sugars for the fermentation process. They are not directly exploitable but must be obtained from the degradation of the starting polymers.

Hydrolyzation of cellulose can be carried out by means of a specific class of enzymes, *cellulases*, produced by several microorganism in nature, but in the industrial domain the most used are filamentous fungi, such as the genera *Aspergillus*, *Penicillium* and *Trichoderma*. The latter is the most employed industrially, in particular the species *Trichoderma Reesei* is considered the "*king of cellulolytic fungi*" (Gusakov, 2011).

Between the whole bioethanol production process, pre-treatments to the biomass are the costliest step (Lynd et al., 2017), due to the cost of enzyme production, thus research efforts focused on the optimization of large-scale processes.

## 2.3 Filamentous fungi: morphology and fermentation issues

Filamentous fungi can have various morphologies depending on the culture environment. These differences can affect significantly the rheological properties of the cultivation medium and consequently the growth of the microorganism and the production of metabolites (Shang-Tian Yang, 2006).

Single unicellular or pluricellular filaments are called *hyphae*, which collectively forms the *mycelium*, the main vegetative body of these microorganism. Filamentous microorganism can be found as compact pellet of hyphae or dispersed mycelia (Shang-Tian Yang, 2006). Morphological behaviour is influenced by several factors such as the strain used, growth rate, medium composition, surfactants, shear force, aeration, agitation, temperature and sources of Carbon, Nitrogen and C/N ratio. *Trichoderma reseei* is mainly encountered in dispersed form (Hardy, 2016). In this case filamentous hyphae entangle with each other, making the fermentative broth very viscous and with a non-Newtonian rheological behaviour. The broth appears as a shear-thinning fluid which shows low viscosities in regions with high shear rates, close to the impeller, and high viscosities in region with low shear rates, such as close to the walls (Shang-Tian Yang, 2006). This behaviour has a direct effect on mixing performances increasing the heterogeneities in the bioreactor and decreasing the mass transfer as well as heat transfer. Moreover, the increase of input power, needed to improve the homogeneity, cause greater damage to the microorganism cell, due to higher shearing.

Hardy and co-workers (Hardy et al., 2015) in IFPEN characterized the rheological behaviour of an industrial strain of *T. Reesei* and the main results are shown in "Figure 2.3". As the biomass concentration increase over time during fermentation the apparent viscosity increase as well, at first linearly and then with a power relationship with concentration. At the beginning of the process the rheological behaviour is mainly influenced by interaction between biomass and broth, whereas further on, with higher concentration of microorganism, interactions within filamentous structures overcome the first effect.

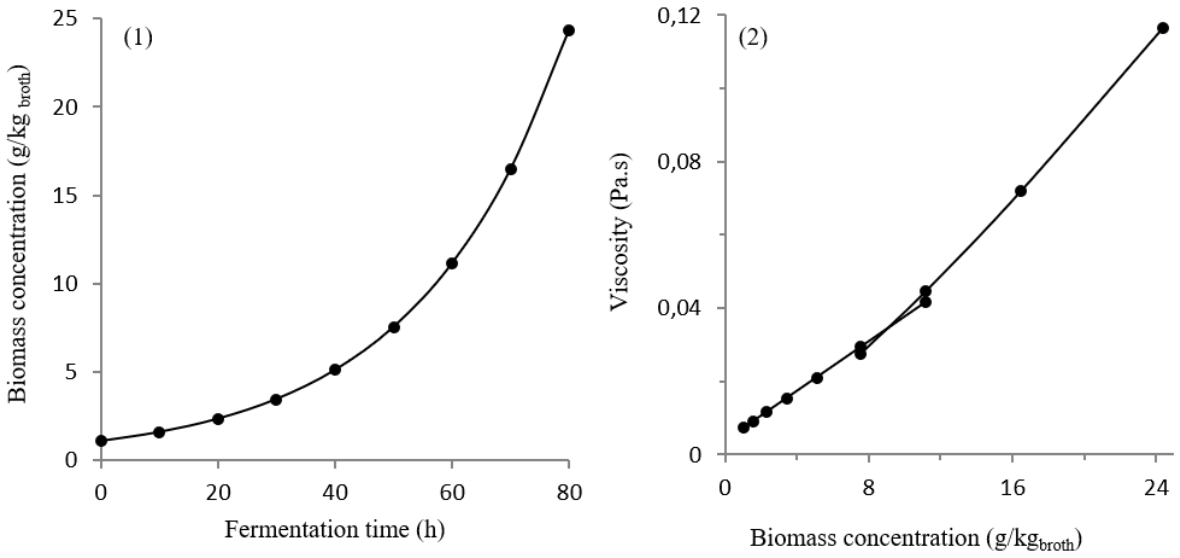


**Figure 2.3** Biomass concentration over time (1) and apparent viscosity (at constant shear rate =220 $s^{-1}$) over biomass concentration (2) (Hardy et al., 2015).

## 2.4 Outline of the process developed at IFPEN

Production of *cellulase* takes place in two main phases: first the growth of the strain then the production of the enzyme.

The growing phase begins with the inoculation of the strain in a batch stirred tank reactor, with excess of substrate and nutrients.

Nutrients concentration decreases whereas biomass concentration increases, thus the growing phase can be carried out in different reactor of growing sizes. This step is decisive in reaching the maximum concentration of microorganisms but entails several challenges due to the changes in the rheological behaviour. The constant supply of oxygen to *Trichoderma reseei*, which is a strictly aerobic species, is hindered by the rise of viscosity and subsequent variation of mass transfer coefficient.

The second phase of this process, that is the production of cellulase, must be carried out at low substrate concentration, otherwise the microorganism would grow instead of secreting the enzyme. This step occurs in an aerated stirred tank as the previous one but in *fed-batch* mode, that means sugars are supplied at a low and constant rate. Low gradients of substrate must be achieved in order to guarantee a homogeneous production of enzyme all over the tank. Finally, the broth is filtered to recover the enzyme and the biomass.

# 3 Theoretical aspects of stirred tank reactors

Mechanically stirred tanks reactors (*STR*) are widely used in many industrial applications, such as chemical, biochemical, food and pharmaceutical industries.

They are characterized by relatively low capital and operating costs, as well as by good mixing performances.

Common application of this kind of reactors includes mixing, polymerization, dissolution, fermentation and waste-water treatment.

The main features of a *STR* are:

- A cylindrical tank, which can have a flat or a rounded bottom;
- One or more impellers, which can differ in shapes depending on the desired mixing effect, clamped to a rotating shaft;
- Side baffles, which suppress the effect of natural swirling flow and improve the mixing by deviating the tangential flow to two opposite axial flow.

When this equipment is used as a gas-liquid contactor, e.g. as an aerobic fermenter, a gas sparger is present, usually at the bottom of the tank to provide the oxygen needed in the process.

Different geometries can be encountered depending on the process in exam, but, commonly, "squared" tanks are widely studied in academic literature and experimentally. These kinds of tanks are characterized by defined proportions within its parts shown in "Figure 3.1": tank height *H* is equal to the tank diameter *T*, the impeller diameter *D* is equal to one third of *T*, the impeller clearance from the bottom *C* is once again equal to one third of *T*.

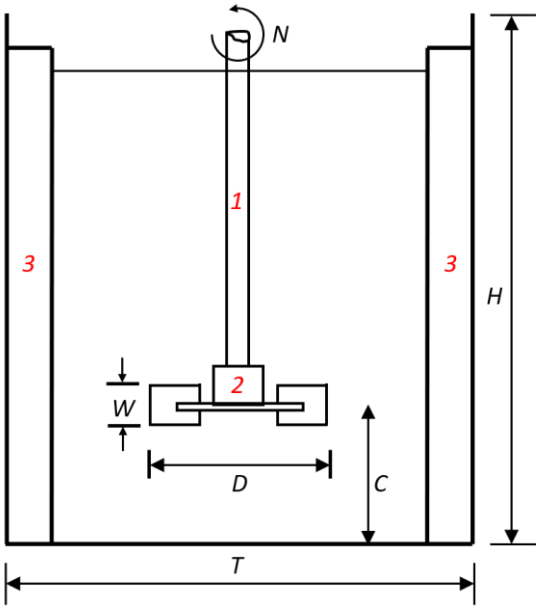


**Figure 3.1** Section of a *Squared* tank: (1) rotating shaft, (2) impeller, (3) side baffles.

As a general matter, scale-up of this kind of operating units is not an easy task, considering the great number of parameters to take into account and the multiscale phenomena occurring during mixing. Common procedure in industrial applications is, to derive empirical correlations after conducting an experimental campaign, but the intrinsic limit of this practice is that these correlations are usually valid only for a specific range of operating condition and/or tank geometries.

In this chapter will be firstly explained some theoretical aspects of STR hydrodynamics with a monophasic flow, either Newtonian and non-Newtonian fluids, then for a multiphasic gas-liquid flow with particular care to those parameters and physical quantities that indicate mixing performances or can be useful to the scale- up of the process.

## 3.1 Hydrodynamics

Single-phase liquid in stirred tanks is of limited industrial application, but its study is of interest in understanding the general behaviour during mixing. At first, it is helpful to briefly describe the flow patterns encountered in stirred tanks, generated by different kind of impellers which, as a general distinction, can be classified into two types: propellers and disk turbines (Edwards et al. 1992), as it is shown in “Figure 3.2”.

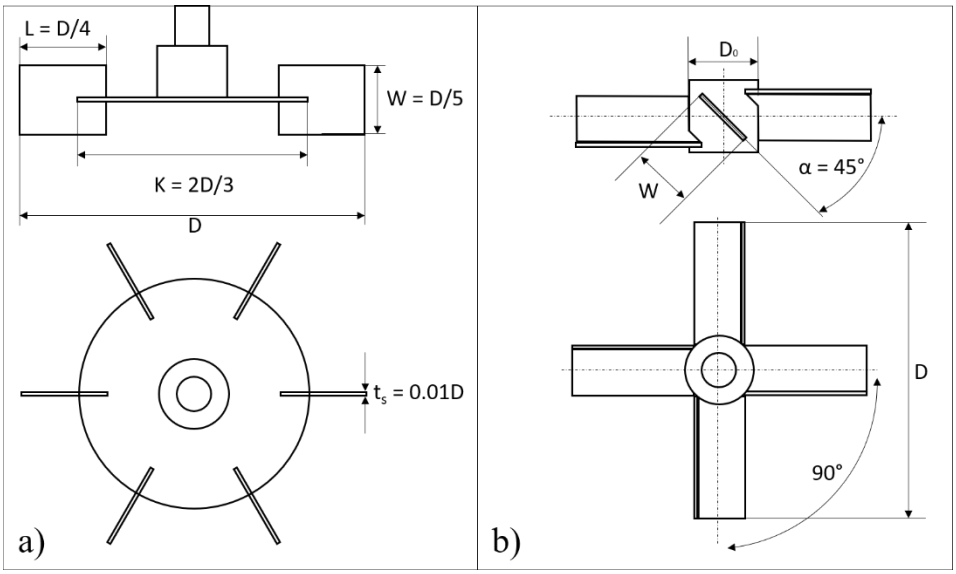


**Figure 3.2** Example of impellers. On the left a *Rushton turbine*, a flat disk impeller (a); On the right a *45° Pitch-blade turbine*, an axial propeller (b).

Propeller creates an axial flow pattern, characterized by two main fluid loops symmetric with respect to the rotating shaft, pumping up- or downward depending on the rotation direction. Flat disk turbines, instead, create a strong rotational flow outward from the impeller, with four circulation zones: two greater fluid loops above the impeller and two smaller loops below, as in “Figure 3.3”.

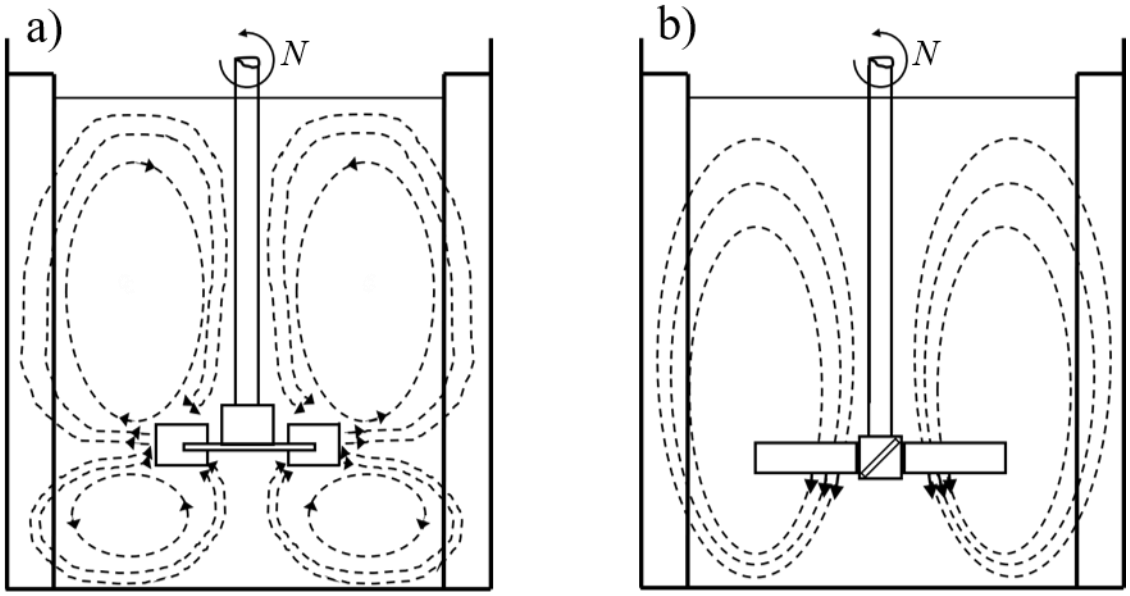


**Figure 3.3** Flow patterns generated by two different type of impeller. On the left a radial impeller (a); on the right an axial impeller (b).

The choice of the type of impeller and their number depends on the process itself. Axial impellers generate a more circulating flow pattern, more suitable for suspending solid particles, with higher pumping. Radial impellers, instead, create a flow pattern which has larger tangential velocities and higher shears, higher turbulence and lower pumping, thus are more suitable for gas-liquid dispersions (Edwards et al. 1992; Paul et al. 2004). If the mixing is not uniform, it may be necessary to add additional impellers clamped to the same shaft, in order to improve global mixing performances. For instance, this is what happen if the fluid has a non-Newtonian behaviour, such as shear-thinning fluids. In this case the area around the impeller is well mixed, further on, instead, the velocities are very low, and the mixing is poor. This behaviour is called "*cavern*" formation; between the cavern and the stagnant dead zone there is no exchange of material (Nienow 1998) and mass transfer is given only by diffusion phenomena.

The physical values generally used to describe the global hydrodynamics are *power input* and *mixing time*, whereas it is possible to find correlation for more local properties such as *velocities profiles*.

### 3.1.1 Power input

Power input $P$ is one of the key parameters in stirred tanks design and in the turbulent regime it is correlated to dissipation of turbulent kinetic energy $\varepsilon$. Power draw depends on the fluid properties ( density $\rho$ , viscosity $\mu$), tank geometry (height $H$, diameter $T$, impeller diameter $D$, blades width $W$), on the impeller type and rotational speed $N$:

$$P = f(\rho, \mu, N, g, H, T, D, W, impeller\ type) \tag{3.1}$$

It is necessary to introduce the following dimensionless quantity: the stirred tank *Reynolds Number*, which is the ratio between inertial and molecular phenomena

$$Re = \frac{\rho N D^2}{\mu} \tag{3.2}$$

The impeller *Power Number*, which is similar to the drag coefficient in cylindrical pipes

$$N_p = \frac{P}{\rho N^3 D^5} \tag{3.3}$$

The stirred tank *Froude Number*, that is the ratio between inertia and gravitational forces

$$Fr = \frac{N^2 D}{g} \tag{3.4}$$

It is possible to relate the power draw $P$ to mixing performances by means of dimensionless analysis (Edwards et al. 1992). For a given geometry and impeller type:

$$\frac{P}{\rho N^3 D^5} = f\left(\frac{\rho N D^2}{\mu}, \frac{N^2 D}{g}\right) \tag{3.5}$$

The *Froude number* is relevant only in case of great vortexes and swirling flow, which in common industrial condition, at high Reynolds number, are eliminated by the presence of the baffles, thus

$$N_p = f(Re) \tag{3.6}$$

A curve can be obtained plotting $N_p$ vs $Re$ in a double logarithmic scale, as shown in "Figure 3.4". For a given geometry, two universal regions can be identified: the laminar one ($Re$ <10), where the power number depends strongly on Reynold ($\propto Re^{-1}$), whereas in the turbulent one ($Re$ >$10^4$) $N_p$ becomes constant and independent from $Re$. In between of these two regions, in the transitional regime no simple mathematical relation exists between the two adimensional numbers.

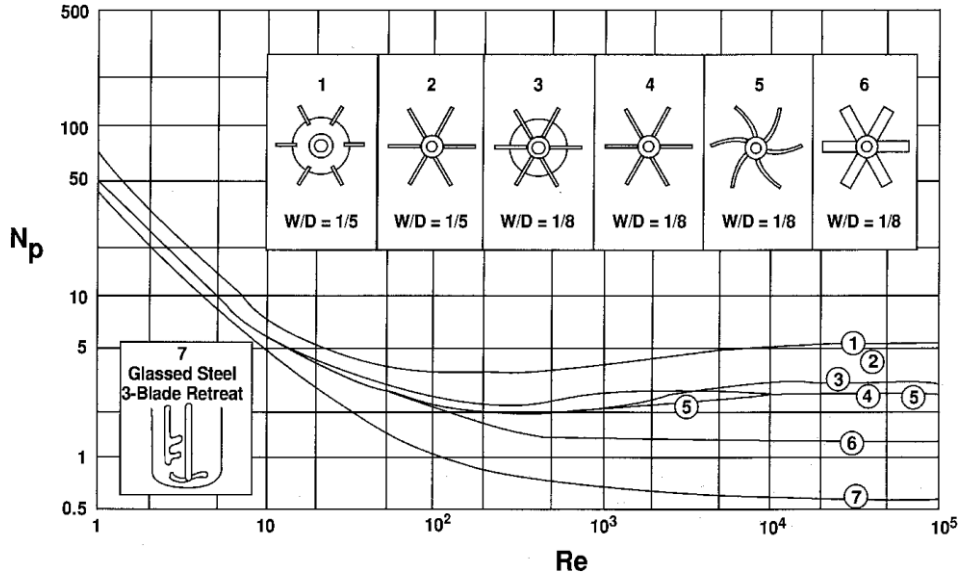


**Figure 3.4** Power number as a function of Reynolds number for seven types of impellers. From (Paul et al. 2004).

From "Table 3.1", which shows some values of $N_p$ for different type of impeller, it can be seen that Rushton turbine has the highest value of power number, whereas axial impellers have lower values.

**Table 3.1** Power number of different type of impeller in turbulent condition (Nienow 1998).

| **Impeller geometry** | **$N_P$** |
|---|---|
| Six-blade Rushton | 5.00 |
| Scaba 6SRGT | 0.45 |
| 4 blades inclined (45°) | 1.27 |
| 6 blades inclined (45°) | 1.70 |
| Lightnin A315 | 0.84 |

Since the power input of an impeller is related to the torque $\Gamma$ by the relationship:

$$P = 2\pi N\,\Gamma \tag{3.7}$$

Thus, substituting in Eq. (3.3) and rearranging:

$$\Gamma = \frac{N_p \rho N^2 D^5}{2\pi} \tag{3.8}$$

High $N_p$ correspond to high torque impeller, which means that for a given power input and size, it requires low speed and high torque (Nienow 1998). On the contrary an impeller with low $N_p$, operating at the same condition, requires lower power and are less expensive.

Despite this, it might be useful using a high $N_p$ impeller in fermentative application, because it allows to operate at lower rotational speed and thus at lower shear-rate, reducing the risk of damaging the microorganism cells.

### 3.1.2 Non-Newtonian fluids

Fermentative broths of filamentous fungi have usually a non-Newtonian shear-thinning behaviour, with viscosity that depends on the shear-rate $\dot{\gamma}$. The power-law model, or Ostwald model, can be applied to describe the broth behaviour:

$$\tau = K\dot{\gamma}^n \tag{3.9}$$

Where $\tau$ is the *shear-stress*, $K$ is the *consistency index* and $n$ is the *flow behaviour index*. A shear-thinning fluid has a value of $n$ <1, thus viscosity decreases as shear-rate increases. it is possible to define an *apparent viscosity* $\mu_a$ as:

$$\mu_a = \frac{\tau}{\dot{\gamma}} = K\dot{\gamma}^{n-1} \tag{3.10}$$

Knowledge of the average spatial shear rate is important to estimate the influence on apparent viscosity and thus on many aspects such as mixing, power draw and transfer

coefficients but also, as stated above, to estimate the potential damage on cells. Metzner and Otto (Metzner and Otto, 1957) made the assumption that in shear-thinning fluid, in laminar regime, an average shear-rate $\dot{\gamma}_A$ can be estimated and that it is proportional to the rotational speed of the agitator, deriving an empirical correlation:

$$\dot{\gamma}_A = k_s N \tag{3.11}$$

Coefficient $k_s$ is the Metzner-Otto constant of the impeller; for a Rushton turbine $k_s$=11.5. Substituting Eq. (3.11) in Eq. (3.10) and then again in Eq. (3.2) an average *Reynolds number* can be obtained, with which it is possible to make an estimation of the flow regime, comparing the shear-thinning fluid to a Newtonian fluid with the same apparent viscosity:

$$Re = \frac{\rho N^{2-n} D^2}{K k_s^{n-1}} \tag{3.12}$$

Formally, this Eq. (3.12) is valid only in the laminar regime, but it has been used successfully for the turbulent regime by several authors (Venneker et al., 2010; Ameur and Bouzit, 2012; Zhang et al., 2017; Khapre and Munshi., 2014). (Sánchez Pérez et al., 2006) derived Metzner-Otto equation in a rigorous analysis, Eq. (3.13), extending its use also to turbulent regime and non-Newtonian fluids, Eq. (3.14).

$$\dot{\gamma} = qN \tag{3.13}$$

$$\dot{\gamma} = q' N^{\frac{3}{1+n}} \tag{3.14}$$

The Eq. (3.13) is valid in laminar regime, whereas Eq. (3.14) can be used in turbulent regime. It defines the average shear rate in a stirred tank as a function of the rotational speed. The constant *q'* is function of rheological indexes, tank geometry and impeller type.

### 3.1.3 Mixing time

An ideal definition of *mixing time* $\theta_m$ is the amount of time that a tracer, injected in a stirred tank, takes to reach a certain degree of homogeneity inside the vessel. Experimentally it is determined using several different techniques, such as electrical conductivity variation, acid/base/chemical reactions as well as more direct ones, such as injecting a dye and establish which areas are more homogeneously coloured than others, revealing stagnant zones.

Mixing time is correlated to turbulent quantities, namely turbulent *integral scale* and turbulent *energy dissipation*. In his review, (Nienow 1998)) outlines the proportional relationship between mixing time and turbulent diffusion, Eq. (3.15), where $\varepsilon_T$ is dissipation of turbulent kinetic energy and $L_c$ is the integral scale of turbulence.

$$\theta_m \propto \left(\frac{\epsilon_T}{{L_c}^2}\right)^{-\frac{1}{3}} \tag{3.15}$$

The relationship between $\theta_m$ and $\varepsilon_T^{-1/3}$ then confirms that:

$$\theta_m \propto \frac{1}{N} \tag{3.16}$$

Several experimental studies also report (Nienow 1998) that mixing time decrease with the aspect ratio $(D/T)^{-2}$:

$$\theta_m \propto \left(\frac{D}{T}\right)^{-2} \tag{3.17}$$

Because the turbulent integral scale is directly proportional to the tank dimension, $L_c \propto T$, then:

$$\theta_m \propto T^{\frac{2}{3}} \tag{3.18}$$

So, a global proportional correlation between mixing time, turbulent quantities and vessel geometry is:

$$\theta_m \propto \left(\frac{\bar{\epsilon}_T}{T^2}\right)^{-\frac{1}{3}} \left(\frac{D}{T}\right)^{-\frac{\alpha}{3}} \tag{3.19}$$

$\bar{\epsilon}_T$ is the average dissipation rate inside the tank, which can be related to power input and to the power number:

$$\bar{\epsilon}_T = \frac{P}{\rho V} \propto \frac{N_p N^3 D^5}{T^3} \tag{3.20}$$

Thus, comparing Eq. (3.19) with Eq. (3.17), α =1 and with further rearrangements:

$$\theta_m \propto \frac{{N_p}^{-\frac{1}{3}}}{N} \left(\frac{D}{T}\right)^{-2} \tag{3.21}$$

Which is the prototype for several correlation for estimate the mixing time in stirred tank reactors.

Eq. (3.19) outline how *mixing time* can be decreased and, therefore, how to improve homogeneity inside the tank. Mixing performances improve by increasing power input and impeller speed, which is somewhat obvious, but also by increasing impeller/tank diameter ratio, which means either a bigger impeller, given a tank diameter, or by using smaller tanks.

## 3.2 Aerated stirred tank reactors

Introduction of gas in the vessel, by means of a sparger, induces changes in the global hydrodynamics of the system. Because of natural coalescence, air forms bubbles which increase in dimension during their rise in the tank. It is well known that transfer phenomena between gas and liquid increase with the contact area between the two phases, thus the desired aim is to keep bubble as small as possible all over the vessel. This is achieved by providing the right amount of energy to break up the larger bubbles. Interaction between the two phases depends, thus, on operating condition as well as on the tank geometry.

In the literature three different regimes are identified, named *"flooding"*, *"loading"* and *"fully recirculated"*, in "Figure 3.5" the transition of flow regime at constant flow rate is shown. They can be described by means of two dimensionless number (Lee and Dudukovic 2014): Froude number, see Eq. (3.4) and Gas Flow number, $Fl_G$.

$$Fl_G = \frac{Q_g}{ND^3} \tag{3.22}$$

*Fr* is the ratio between the acceleration induced by the impeller motion and gravity. $Fl_G$, instead, is the ratio between the gas flowrate and the impeller driven flowrate. In fact the action of the impeller can be compared to that of a radial or axial pump, and the whole stirred tank as a caseless pump (Edwards et al. 1992).

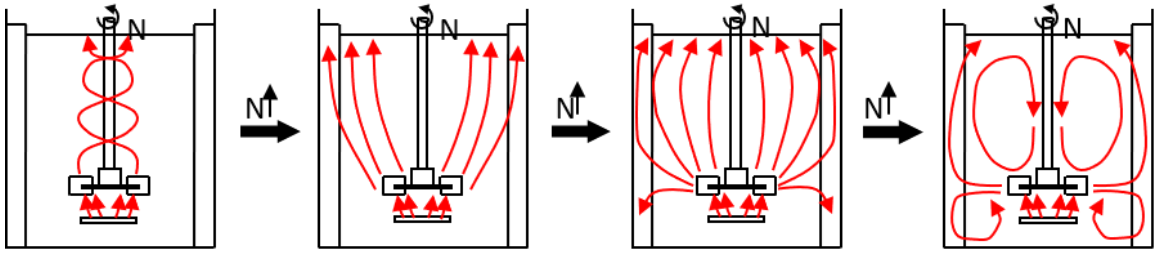


**Figure 3.5** Flow regimes in a fully baffled stirred tank with Rushton impeller, red lines representing the gas flow. The transition between the three behaviours is shown at increasing impeller speed, with constant gas flow rate (Edwards et al. 1992).

*Flooding* occurs when the energy provided by the impeller is not sufficient to break up air bubbles, which bypass the agitator and rise along the shaft, causing large reduction in power consumption, low gas hold up and poor mixing performances (Paul et al. 2004). By increasing *Fr* number, providing more agitation with higher rotational speed, the system becomes more dispersed. By decreasing $Fl_G$ number, either by increasing impeller rotational rate or by decreasing gas flow rate, the same results can be achieved. Thus, bubbles start to occupy the upper part of the vessel. If the agitation is high enough, then gas starts to be recirculated in the tank, reaching maximum dispersion conditions.

A flow map of the system, as a function of *Fr* and $Fl_G$ numbers can be derived, as in "Figure 3.6". Two line identifies the transition between "*flooding*" and "*loading*" regimes, at the velocity $N_{CD}$, and between "*loading*" and "*recirculated*" regime, at impeller velocity $N_R$, which is the rotational rate at which the system has homogeneous gas distribution inside the vessel (Lee and Dudukovic 2014; Nienow 1998).

Transition from *flooding* to *loading*

$$Fl_G = 30Fr\left(\frac{D}{T}\right)^{3.5} \tag{3.23}$$

Transition from *loading* to *recirculated regime*

$$Fl_G = 13Fr^2\left(\frac{D}{T}\right)^{5} \tag{3.24}$$

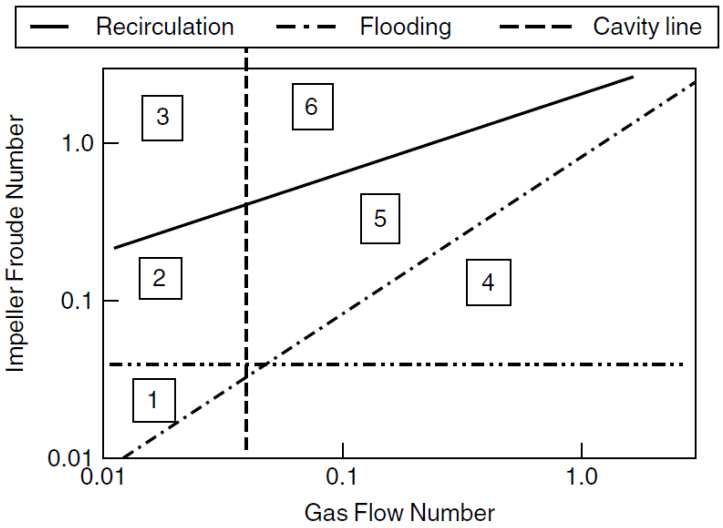


**Figure 3.6** Flow map for a single Rushton turbine. (1) below minimum dispersion; (2) vortex cavities, no recitculation; (3) vortex cavities with recirculation; (4) flooded; (5) loaded with large cavities; (6) large cavities with recirculation.

In addition to these relations:

- if $Fr < 0.04$ the impeller speed is too low to have any discernible action;
- if $Fl_G > 0.025(D/T)^{-0.5}$ large cavities forms behind the blades.

In the low-pressure regions behind impeller blades the air tends to accumulate, forming cavities which cause a sensible reduction of the power provided to the system and thus of the power number, up to a half of the single phase one. As gas flow-rate increase, the shape of these cavities changes from vortex-like to proper gas pockets, as shown in "Figure 3.7" and more in detail in "Figure 3.8".

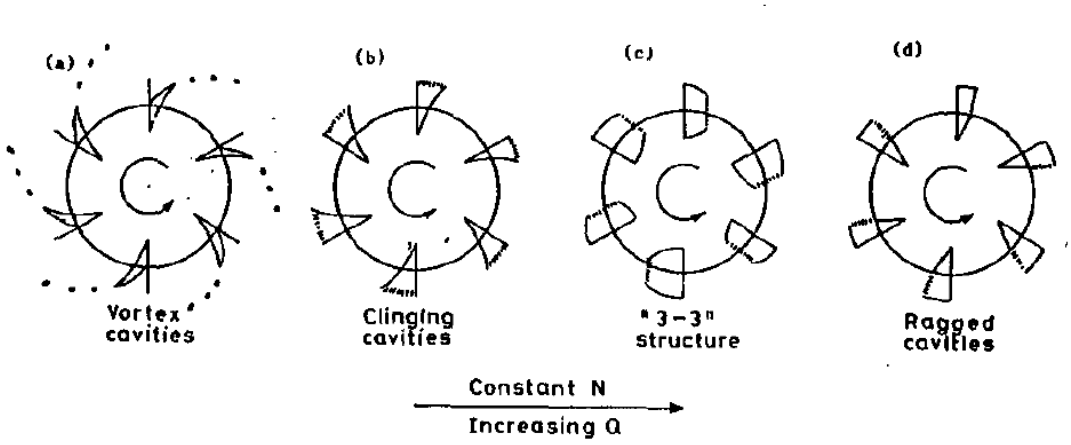


**Figure 3.7** Change in cavities shape at increasing gas flow-rate, with constant rotational rate (Nienow 1998).

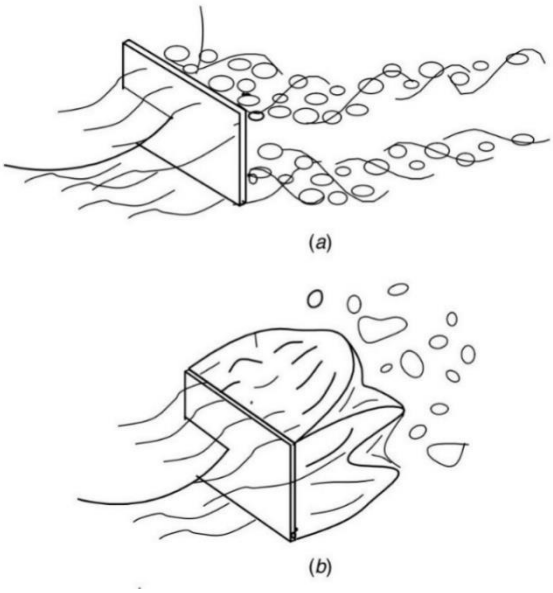


**Figure 3.8** Particular of gas cavities with a Rushton turbine : (a) vortex cavities (b) large cavities (Paul et al. 2004).

Because of all the aspects explained above, the power draw in aerated stirred tanks, $\mathbf{P_G}$, is lower than in ungassed systems and a common way to estimate this reduction is by means of the *"relative power demand (RPD)*". Several correlations have been proposed in literature by many authors (Bouaifi and Roustan 2001; Luong and Volesky 1979; Gabelle et al. 2011; Paul et al. 2004). The correlation proposed by (Gabelle et al. 2011) has been validated for a wide range of gas flowrates and could be used for the scale-up of bioreactors. It is the one used in the several works done at IFPEN on this subject. It expresses a strong influence of the geometry, in particular the tank diameter, and of the gas flow rate on the relative power draw:

$$\ln\frac{P_G}{P} = -15.36\ {Q_G}^{0.62} T^{-1.27} \left(\frac{D}{T}\right)^{0.51} {N_P}^{0.16} \tag{3.25}$$

# 4 Computational fluid dynamics theoretical

Until recent years, research for scale-up purposes in the field of stirred tanks focused on deriving empirical correlations. The use of these correlations, however, is subjected to limitation, for they are based on geometry constraint or particular operating conditions (Bach et al. 2017).

The exponential increase of computational power in the last 30 years allowed numerical modelling and simulations to become more valuable tools in applied research along with experimental methods. In addition, "C*omputational Fluid Dynamics"* (CFD) can provide valuable information about local properties not easily achievable with experimental methods.

## 4.1 Governing equation of turbulent flows

The hydrodynamics inside a stirred tank is described by the *continuity equation*, Eq. (4.1), which represent the conservation of mass inside the system and by *Navier-Stokes equations*, Eq. (4.2) which represents the conservation of momentum. The equations are presented in Eulerian form, with Tensor notation, in which subscripts $i,j = 1,2,3$ indicate three general spatial coordinates (Bird et al. 2002; Andersson et al., 2012):

$$\frac{\partial \rho}{\partial t} + \frac{\partial (\rho U_i)}{\partial x_i} = 0 \tag{4.1}$$

$$\frac{\partial (\rho U_i)}{\partial t} + \frac{\partial \left(\rho U_i U_j\right)}{\partial x_j} = -\frac{\partial p}{\partial x_i} + \frac{\partial d_{ij}}{\partial x_j} + \rho g_i \tag{4.2}$$

Where $\rho$ is the fluid density, $U_i$ is the fluid velocity $i$ component, $p$ is the fluid pressure, $g_i$ is the gravitational acceleration $i$ component and $d_{i,j}$ is the *viscous stress tensor* general component $i,j$, which for a Newtonian fluid can be written as:

$$d_{ij} = \mu \left[ \left( \frac{\partial U_i}{\partial x_j} - \frac{\partial U_j}{\partial x_i} \right) - \frac{2}{3} \frac{\partial U_i}{\partial x_i} \right] \tag{4.3}$$

Concerning the fluids that are treated in this work, they are liquids, which are assumed incompressible, i.e. density is constant with respect to time and space coordinates. Thus from Eq. (4.1):

$$\frac{\partial U_i}{\partial x_i} = 0 \tag{4.4}$$

Substituting Eq. (4.3) in Eq. (4.2) and rearranging:

$$\frac{\partial U_i}{\partial t} + U_j \frac{\partial U_i}{\partial x_j} = -\frac{1}{\rho} \frac{\partial p}{\partial x_i} + \frac{1}{\rho} \frac{\partial}{\partial x_j} \left[ \mu \left( \frac{\partial U_i}{\partial x_j} + \frac{\partial U_j}{\partial x_i} \right) \right] + g_i \tag{4.5}$$

And for Newtonian fluids with constant viscosity μ:

$$\frac{\partial U_i}{\partial t} + U_j \frac{\partial U_i}{\partial x_j} = -\frac{1}{\rho}\frac{\partial p}{\partial x_i} + \nu \frac{\partial}{\partial x_j}\left(\frac{\partial U_i}{\partial x_j} + \frac{\partial U_j}{\partial x_i}\right) + g_i \tag{4.6}$$

Moreover since :

$$\nu \frac{\partial}{\partial x_j}\left(\frac{\partial U_i}{\partial x_j} + \frac{\partial U_j}{\partial x_i}\right) = \nu \frac{\partial^2 U_i}{\partial x_j \partial x_j} \tag{4.7}$$

Than Eq. (4.6) becomes:

$$\frac{\partial U_i}{\partial t} + U_j \frac{\partial U_i}{\partial x_j} = -\frac{1}{\rho}\frac{\partial p}{\partial x_i} + \nu \frac{\partial^2 U_i}{\partial x_j \partial x_j} + g_i \tag{4.8}$$

An analytical solution for this set of equations is possible only for particular laminar flows, in which several assumptions can be made to simplify the problem. However, most industrial application has turbulent flows, therefore modelling of turbulence is necessary to acquire information concerning the hydrodynamics of the system.

## 4.2 Turbulent models

Turbulent flows are intrinsically chaotic, characterized by time-dependent fluctuation of relevant flows variables *U* and *p*, thus there are several computational methods developed to solve eq (4.4) and Eq. (4.8).

A first approach, which is to directly solve these equations without any model for turbulence, is called *direct numerical simulation* (DNS). This strategy is not feasible for engineering applications, because it requires huge computational resources. As a matter of fact, very fine time and space resolution are needed to characterize high Reynolds flows. Considering the smallest turbulent scale, the Kolmogorov space and time scale, respectively Eq.s (4.9) and (4.10) for a stirred tank they are about 50 μm and 5 ms (Andersson et al. 2012).

$$\eta = \left(\frac{\nu^3}{\epsilon}\right)^{\frac{1}{4}} \tag{4.9}$$

$$\tau_\eta = \left(\frac{\nu}{\epsilon}\right)^{\frac{1}{2}} \tag{4.10}$$

Turbulence is a multiscale phenomenon, energy being created at the biggest scale, namely *L*, and being dissipated at the smallest one, $\eta$. For an isotropic, steady turbulent flow, the energy created and the one dissipated are equal. By dimensional analysis it is possible to estimate the energy dissipation rate, since it is equal to the production of kinetic energy *k*, relating it with the macroscale *L*. Kinetic energy of the flow is proportional to $U^2$ and the time scale of large eddies is *L/U*. ε has dimension of ($m^2/s^3$), thus:

$$\epsilon \sim \frac{U^2}{L/U} \sim \frac{U^3}{L} \tag{4.11}$$

And substituting Eq. (4.9) into Eq. (4.7):

$$\eta \sim \left(\frac{\nu^3 L}{U^3}\right)^{\frac{1}{4}} \tag{4.12}$$

The ratio between the bigger and smaller scale represent a rough estimate of the number of grids element in each dimension necessary to have a good solution:

$$N_{grids} = \frac{L}{\eta} \sim \left(\frac{UL}{\nu}\right)^{\frac{3}{4}} = Re^{\frac{3}{4}} \tag{4.13}$$

Being turbulence a three-dimensional phenomenon, cell should than be $N^3$, thus the number of cells becomes:

$$N_{grids} \sim Re^{\frac{9}{4}} \tag{4.14}$$

It is clear that, for fully turbulent flows, the computational costs of DNS simulations exceed the capacity of any existing computer.

A less expensive formulation for turbulent problems is the *large eddy simulation* (LES), which models only the smallest scales, where turbulence is isotropic and viscous forces are relevant. Therefore, computational costs are reduced, for only the larger scales are directly solved. However, for most engineering application, the grids requirements are still burdening.

The most common way to deal with turbulent flows is by time-averaging the equations governing the system, obtaining a solution for the mean values of the flow properties in time and space.

Osborne Reynolds (Reynolds 1895) proposed to split instantaneous variables into the sum of a mean part and a fluctuating part. This is known as *Reynolds decomposition*:

$$U_i = \langle U_i \rangle + u_i' \tag{4.15}$$

The time averaging for a general variable $\Phi$ ($\mathbf{x}$,t) is defined as follow:

$$\langle \phi \rangle (\boldsymbol{x}) = \frac{1}{\Delta t} \int_t^{t+\Delta t} \phi(\boldsymbol{x}, t')\, dt' \tag{4.16}$$

$\Delta$t, the time of averaging, should be long enough to smooth the fluctuations, allowing to statistically describe the flow. Applying the decomposition to velocity and pressure in continuity and momentum Eq.s (4.1) and (4.2):

$$\frac{\partial(\langle U_i \rangle + u_i')}{\partial x_i} = 0 \tag{4.17}$$

$$\frac{\partial(\langle U_i \rangle + u_i')}{\partial t} + \left(\langle U_j \rangle + u_j'\right) \frac{\partial(\langle U_i \rangle + u_i')}{\partial x_j} = -\frac{1}{\rho} \frac{\partial(\langle p \rangle + p')}{\partial x_i} + \nu \frac{\partial^2(\langle U_i \rangle + u_i')}{\partial x_j \partial x_j} + g_i \tag{4.18}$$

Applying the operator of Eq. (4.16) gives a new set of equations, known *as Reynolds average Navier-Stokes* (RANS), expressed in Eq. (4.19) and (4.20):

$$\frac{\partial \langle U_i \rangle}{\partial x_i} = 0 \tag{4.19}$$

$$\frac{\partial \langle U_i \rangle}{\partial t} + \langle U_j \rangle \frac{\partial \langle U_i \rangle}{\partial x_j} = -\frac{1}{\rho}\frac{\partial \langle p \rangle}{\partial x_i} + \nu \frac{\partial^2 \langle U_i \rangle}{\partial x_j \partial x_j} - \frac{\partial \langle u_i' u_j' \rangle}{\partial x_j} + g_i \tag{4.20}$$

The last of which can be written:

$$\frac{\partial \langle U_i \rangle}{\partial t} + \langle U_j \rangle \frac{\partial \langle U_i \rangle}{\partial x_j} = -\frac{1}{\rho}\frac{\partial \langle p \rangle}{\partial x_i} + \frac{1}{\rho}\left[\mu\left(\frac{\partial \langle U_i \rangle}{\partial x_j} + \frac{\partial \langle U_j \rangle}{\partial x_i}\right) - \rho \langle u_i' u_j' \rangle\right] + g_i \tag{4.21}$$

Eq. (4.21) looks very similar to Eq. (4.6) except for the additional term $d_{ij}^t = -\rho \langle u_i' u_j' \rangle$, called *Reynolds stresses* or *Reynolds stress tensor* (RST). It represents the interaction between fluctuating parts and mean flows, that is the additional stress due to turbulent eddies. It is a second-order symmetric tensor, thus it contains six unknown terms that have to be modelled. A first approach would be to derive a transport equation for the Reynolds stresses, however this leads to a third-order unknown tensor. Deriving another equation for this term would yield to an equation that contains a fourth-order tensor and so on. Therefore, a more practical approach must be found to solve this problem, known as *closure problem*.

Boussinesq approximation (Andersson et al. 2012) suggest Reynolds stresses should be a function of the mean velocity gradient, implying that turbulence transfers momentum as a diffusivity process.

$$\frac{d_{ij}^t}{\rho} = -\langle u_i' u_j' \rangle = \nu_T \left(\frac{\partial \langle U_i \rangle}{\partial x_j} + \frac{\partial \langle U_j \rangle}{\partial x_i}\right) - \frac{2}{3} k \delta_{ij} \tag{4.22}$$

Where $k$ is turbulent kinetic energy and $\delta_{ij}$ is the Kroneker delta. An alternative form is:

$$\frac{d_{ij}^t}{\rho} = -\langle u_i' u_j' \rangle = \nu_T 2 S_{ij} - \frac{2}{3} k \delta_{ij} \tag{4.23}$$

Where $S_{ij}$ is the *strain rate* tensor:

$$S_{ij} = \frac{1}{2}\left(\frac{\partial \langle U_i \rangle}{\partial x_j} + \frac{\partial \langle U_j \rangle}{\partial x_i}\right) \tag{4.24}$$

The proportionality factor $\nu_T$ is called *turbulent viscosity* or *eddy viscosity* and its modelling is the aim of several turbulent models based on the Boussinesq approximation.

Eddy viscosity is dimensionally equal to a characteristic velocity $u$ times a length scale $l$, being ($m^2/s$), thus it can be written as:

$$\nu_T = C_\nu u l \tag{4.25}$$

$C_\nu$ is the proportionality constant. Because $\nu_T$ can vary with time and space, then additional transport equations are necessary to determine both $u$ and $l$. Turbulence models can have zero, one, two set of equation in addition to RANS and continuity.

Zero equation or algebraic models require no additional transport equations. Prandtl's *mixing length* model is the most renown, and it proposes an analogy between random walk of molecule

as treated in *kinetic theory of gases* and eddies chaotic motion. However, this model is reliable in predicting only very simple flows. One equation models, instead, relate turbulent viscosity to the transport of turbulent quantity. According Kolmogorov and Prandtl hypothesis, the characteristic velocity $u$ can be expressed as the root mean square of the time-averaged turbulent kinetic energy $k$, whose transport equation is added to the set.

Examples of these models are Prandtl's $k$-$l$ model and Spalart-Allmaras model. The length scale is still determined algebraically. In this work, two equations models have been used, thus a brief description of the different kinds will follow.

Two equation models make use of a further transport equation of a turbulent property $\chi$ to determine both $u$ and $l$. $\chi$ can be express with a power law, as a function of two exponent $\alpha$ and $\beta$:

$$\chi = k^{\alpha} l^{\beta} \tag{4.26}$$

**Table 4.1** Commonly used properties used in two equation models (Andersson et al. 2012)

| α | β | χ | Symbol of χ | Interpretation of χ |
|---|---|---|---|---|
| 0 | 1 | $l$ | $l$ | Length scale |
| 1 | -2 | $k/l^2$ | $\omega$ | Vorticity scale |
| 1/2 | -1 | $k^{1/2}/l$ | $f$ | Frequency scale |
| -1/2 | 1 | $k^{-1/2}l$ | $\tau$ | Time scale |
| 3/2 | -1 | $k^{3/2}/l$ | $\varepsilon$ | Dissipation rate |

In table 4.1 a list of commonly used properties used for transport equation is show. The energy dissipation rate $\varepsilon$ is the most used between these variables turbulent values and the $k$-$\varepsilon$ models are widely applied in many commercial software for numerical simulations of turbulent flows. They are three: Standard $k$-$\varepsilon$ model, RNG $k$-$\varepsilon$ model, Realizable $k$-$\varepsilon$ model. Along with these, also the $k$- $\omega$ model, with vorticity $\omega$ as the length scale determining quantity, plays an important role in common applications such as *enclosed* flows.

### 4.2.1 The *Standard k-ε* model

It is the first two equations closure model developed for turbulence and one of the most important for it was widely applied to interpret turbulence phenomena. The two additional transport equation describe the transport of turbulent kinetic energy $k$ and turbulent dissipation rate $\varepsilon$. The correlation between large-scale quantity $l$ and small-scale $\varepsilon$ follow the assumption that the flow is fully turbulent and isotropic. Kinetic energy $k$ is "extracted" from the mean flow, by mean velocity gradients, and then transferred through the inertial range to the smallest scale, Kolmogorov scale, where viscous forces are comparable with inertial one ($Re_{\eta}$= 1) and it is dissipated by $\varepsilon$. From Table 4.1, expressing $l$ as a function of transported turbulent properties:

$$l = \frac{k^{\frac{3}{2}}}{\epsilon} \tag{4.27}$$

Thus, it is possible to obtain an expression for eddy viscosity:

$$\nu_T = C_{\mu_T} \frac{k^2}{\epsilon} \tag{4.28}$$

The turbulent kinetic energy transport equations are here presented in their final form:

$$\frac{\partial k}{\partial t} + \langle U_j \rangle \frac{\partial k}{\partial x_j} = \nu_T \left[ \left( \frac{\partial \langle U_i \rangle}{\partial x_j} + \frac{\partial \langle U_j \rangle}{\partial x_i} \right) \frac{\partial \langle U_i \rangle}{\partial x_j} \right] - \epsilon + \frac{\partial}{\partial x_j} \left[ \left( \nu + \frac{\nu_T}{\sigma_k} \right) \frac{\partial k}{\partial x_j} \right] \tag{4.29}$$

Where $\sigma_k$ is a model constant. The first term in the right-hand side (RHS) of the Eq. (4.29) represent the production of *k*, appearing as a sink for it extract energy from the mean flow. The last term in RHS, instead, is the transport of due to molecular diffusion, velocity and pressure fluctuations. Dissipation rate, coming from interaction between velocity fluctuation, can be written as:

$$\epsilon = \left\langle \frac{\partial u_i'}{\partial x_j} \frac{\partial u_i'}{\partial x_j} \right\rangle \tag{4.30}$$

His transport equation is:

$$\frac{\partial \epsilon}{\partial t} + \langle U_j \rangle \frac{\partial \epsilon}{\partial x_j} = C_{\epsilon 1} \nu_T \frac{\epsilon}{k} \left[ \left( \frac{\partial \langle U_i \rangle}{\partial x_j} + \frac{\partial \langle U_j \rangle}{\partial x_i} \right) \frac{\partial \langle U_i \rangle}{\partial x_j} \right] - C_{\epsilon 2} \frac{\epsilon^2}{k} + \frac{\partial}{\partial x_j} \left[ \left( \nu + \frac{\nu_T}{\sigma_\epsilon} \right) \frac{\partial \epsilon}{\partial x_j} \right] \tag{4.31}$$

$C_{\varepsilon 1}$, $C_{\varepsilon 2}$, $\sigma_\varepsilon$ are constant of the model. The first term in the RHS is the production of ε, which is inversely proportional to the timescale of the system, being τ = k/ε. The second term represents the dissipation of the energy dissipation rate. The last term, similarly, to Eq. (4.29) is the diffusion of ε due to viscous stresses as well as turbulent fluctuations of *U* and *p*.

The values of the model coefficient, in Table 4.2, are assumed constant, though this is not always true. However, they are chosen as a compromise between accuracy and performance.

**Table 4.2** values of the *k-ε* model coefficient

| Constant | $C_{\mu_T}$ | $C_{\epsilon 1}$ | $C_{\epsilon 2}$ | $\sigma_k$ | $\sigma_\epsilon$ |
|---|---|---|---|---|---|
| Value | 0.09 | 1.44 | 1.92 | 1.00 | 1.3 |

The great merit of this model resides in its relatively low computational cost as well as its robustness, required in common CFD application. However, the assumption of a fully turbulent flow makes it not suitable for those systems characterized by swirling flows, curved streamlines or when the flow is not perfectly isotropic, for in those cases the energy cascade might not be in equilibrium with the production rate.

### 4.2.2 The *RNG k-ε* model

This model was developed by applying "re-normalization group" theory to the Navier-Stokes equations in order to account for the different scales at which the turbulent phenomenon takes place, and thus to consider zones where the flow is not completely turbulent. This led to a set of equations altogether similar to those of *k-ε* model, but for an additional term in the dissipation rate transport equation, which becomes:

$$\frac{\partial \epsilon}{\partial t} + \langle U_j \rangle \frac{\partial \epsilon}{\partial x_j} = C_{\epsilon 1} \nu_T \frac{\epsilon}{k} \left[ \left( \frac{\partial \langle U_i \rangle}{\partial x_j} + \frac{\partial \langle U_j \rangle}{\partial x_i} \right) \frac{\partial \langle U_i \rangle}{\partial x_j} \right] - C_{\epsilon 2} \frac{\epsilon^2}{k} + \frac{\partial}{\partial x_j} \left[ \left( \nu + \frac{\nu_T}{\sigma_\epsilon} \right) \frac{\partial \epsilon}{\partial x_j} \right] - S_\epsilon \tag{4.32}$$

$S_\varepsilon$ is a source term, equal to

$$S_\epsilon = \frac{C_\mu \eta^3 \left(1 - \frac{\eta}{\eta_0}\right) \epsilon^2}{(1 + \beta\, \eta^3) k} \tag{4.33}$$

Where, and $S_{ij}$ is the strain rate tensor:

$$\eta = \frac{k}{\epsilon} \sqrt{2 S_{ij} S_{ij}} \tag{4.34}$$

The model results more accurate in region with high strain rate and curved streamlines or swirling flows, for it tends to be less dissipative than the standard *k-ε*, which is known to overestimate turbulence. The model coefficients, reported in "Table 4.3" are all calculated explicitly, with the exception of $\beta$ which is obtained experimentally.

**Table 4.3** Standard coefficient for the RNG *k-ε* model

| Constant | $C_{\mu_T}$ | $C_{\epsilon 1}$ | $C_{\epsilon 2}$ | $\sigma_k$ | $\sigma_\epsilon$ | $\eta_0$ | $\beta$ |
|---|---|---|---|---|---|---|---|
| Value | 0.0845 | 1.42 | 1.68 | 0.7194 | 0.7194 | 4.38 | 0.012 |

### 4.2.3 The *Realizable k-ε* model

Both Standard and RNG *k-ε* models do not satisfy some physical constraint of the predicted stress tensor. In the *k* transport equation, the normal stress may become negative, $\langle {u'_i}^2 \rangle < 0$, if the mean velocity gradient is too large:

$$\langle u_i' u_i' \rangle = \sum_i \langle {u_i'}^2 \rangle = \frac{2}{3} k - 2 \nu_T \frac{\partial \langle U_i \rangle}{\partial x_j} \tag{4.35}$$

Being a square quantity, this is not mathematically possible. In addition, the stress tensor not always satisfy the Schwarz's inequality, $\langle {u'_i}^2 \rangle \langle {u'_j}^2 \rangle - \langle u'_i u'_j \rangle \geq 0$. Thus, it is said that both the above-mentioned models are not "realizable". The Realizable *k-ε* models has been developed in order to cope with these constraints

$$\frac{\partial \epsilon}{\partial t} + \langle U_j \rangle \frac{\partial \epsilon}{\partial x_j} = C_{\epsilon 1} \nu_T \epsilon \left[ \left( \frac{\partial \langle U_i \rangle}{\partial x_j} + \frac{\partial \langle U_j \rangle}{\partial x_i} \right) \frac{\partial \langle U_i \rangle}{\partial x_j} \right] - C_{\epsilon 2} \frac{\epsilon^2}{k + \sqrt{\nu \epsilon}} + \frac{\partial}{\partial x_j} \left[ \left( \nu + \frac{\nu_T}{\sigma_\epsilon} \right) \frac{\partial \epsilon}{\partial x_j} \right] \tag{4.36}$$

The turbulent viscosity is modelled as follow:

$$\nu_T = C_{\mu_T} \frac{k^2}{\epsilon} \tag{4.37}$$

And $C_{\mu_T}$ is computed from:

$$C_{\mu_T} = \frac{1}{A_0 + A_S \frac{kU^*}{\epsilon}} \tag{4.38}$$

Where

$$U^* \equiv \sqrt{S_{ij}S_{ij} + \widetilde{\Omega}_{ij}\widetilde{\Omega}_{ij}} \tag{4.39}$$

The variable $\widetilde{\Omega}_{ij}$ is defined:

$$\begin{aligned} \widetilde{\Omega}_{ij} &= \Omega_{ij} - 2\epsilon_{ijk}\omega_k \\ \Omega_{ij} &= \overline{\Omega_{\iota J}} - \epsilon_{ijk}\omega_k \end{aligned} \tag{4.40}$$

And with $\overline{\Omega_{\iota J}} = \frac{1}{2}\left(\frac{\partial\langle U_i\rangle}{\partial x_j} - \frac{\partial\langle U_j\rangle}{\partial x_i}\right)$ the mean vorticity of the flow. The parameter $A_S$ of Eq. (4.38) is given by:

$$\begin{cases} A_S = \sqrt{6}\cos\varphi \\ \varphi = \frac{1}{3}\cos^{-1}\left(\sqrt{6}W\right) \\ W = \frac{S_{ij}S_{jk}S_{ki}}{\tilde{S}^3} \\ \tilde{S} = \sqrt{S_{ij}S_{ij}} \\ S_{ij} = \frac{1}{2}\left(\frac{\partial\langle U_i\rangle}{\partial x_j} + \frac{\partial\langle U_j\rangle}{\partial x_i}\right) \end{cases} \tag{4.41}$$

The new feature of Realizable *k-ε* model makes it suited in case of large strain-rate flows, with rotation and strong curvature. Compared with standard model it performs better for swirling flows and in case of flow separation, however it results less stable and more computationally burdening. The model constant are reported in "Table 4.4".

**Table 4.4** Default Realizable *k-ε* model coefficient. Parameter $\eta$ is the same as in Eq. (4.34).

| Constant | $C_{\epsilon 1}$ | $C_{\epsilon 2}$ | $\sigma_k$ | $\sigma_\epsilon$ | $A_0$ |
|---|---|---|---|---|---|
| Value | $max\left(0.43; \frac{\eta}{\eta+5}\right)$ | 1.90 | 1.00 | 1.20 | 4.04 |

### 4.2.4 The *k-ω* model

This class of models use the specific dissipation rate $\omega$ as length scale determining quantity, defined as:

$$\omega = \frac{\epsilon}{k} \tag{4.42}$$

Being $\tau = k/\varepsilon$ the timescale of the turbulent flow, $\omega$ can be interpreted as the frequency of the turbulence. The transport equations of the model, for $k$ and $\omega$ are:

$$\frac{\partial k}{\partial t} + \langle U_j \rangle \frac{\partial k}{\partial x_j} = \nu_T \left[ \left( \frac{\partial \langle U_i \rangle}{\partial x_j} + \frac{\partial \langle U_j \rangle}{\partial x_i} \right) \frac{\partial \langle U_i \rangle}{\partial x_j} \right] - \beta k \omega + \frac{\partial}{\partial x_j} \left[ \left( \nu + \frac{\nu_T}{\sigma_k} \right) \frac{\partial k}{\partial x_j} \right] \tag{4.43}$$

$$\frac{\partial \omega}{\partial t} + \langle U_j \rangle \frac{\partial \omega}{\partial x_j} = \alpha \frac{\omega}{k} \nu_T \left[ \left( \frac{\partial \langle U_i \rangle}{\partial x_j} + \frac{\partial \langle U_j \rangle}{\partial x_i} \right) \frac{\partial \langle U_i \rangle}{\partial x_j} \right] - \beta^* \omega^2 + \frac{\partial}{\partial x_j} \left[ \left( \nu + \frac{\nu_T}{\sigma_\omega} \right) \frac{\partial \omega}{\partial x_j} \right] \tag{4.44}$$

Where $\beta$ and $\beta^*$ are closure coefficients and $\alpha$ is a damping factor, expressed as a function of *Re*, acting as a correction in case of low Reynolds number.

The advantages with respect to *k-ε* model are:

- In the ε transport equation the dissipation term has the factor $\varepsilon^2/k$ and when both the kinetic energy and the dissipation rate approach to zero, in low turbulent areas, they must do it in an appropriate rate, otherwise it becomes an indeterminate form;
- The k-ω model well predict low Reynolds areas and near wall flows, thus not requiring any particular treatment or modification.

As a drawback this model requires very fine grids near walls and boundary layers.

## 4.3 Transport of scalar quantities

Chemical engineering applications of numerical simulations require the resolution of extra scalar transport equations to describe, for instance, chemical species, system enthalpy, temperature or tracers. Therefore, it is worth to shortly describe the governing equation of scalar transport in turbulent flows. The generic transport equation for the scalar ϕ is:

$$\frac{\partial (\rho \phi)}{\partial t} + \frac{\partial (\rho U_i \phi)}{\partial x_i} = \frac{\partial}{\partial x_i} \left( \Gamma_\phi \frac{\partial \phi}{\partial x_i} \right) + S_\phi \tag{4.45}$$

Where $\Gamma_\phi$ is the diffusive coefficient and $S_\phi$ is the source or sink of the scalar. By applying Reynolds decomposition of Eq. (4.15) and the time-average operator of Eq. (4.15) to Eq. (4.45) it becomes:

$$\frac{\partial (\rho \langle \phi \rangle)}{\partial t} + \frac{\partial (\rho \langle U_i \rangle \langle \phi \rangle)}{\partial x_j} = \frac{\partial}{\partial x_j} \left[ \Gamma_\phi \frac{\partial \langle \phi \rangle}{\partial x_j} - \rho \langle u'_i \phi' \rangle \right] + \langle S_\phi \rangle \tag{4.46}$$

The $\rho \langle u'_i \phi' \rangle$ term, which comes from the time-averaging procedure and contains the fluctuation of the scalar quantity, has to be modelled. Following the same line of reasoning to

that used for the Reynolds stresses, it is possible to assume a turbulent diffusive term, proportional to the mean scalar concentration gradient (Combest et al. 2011):

$$-\rho\langle u'_i \phi' \rangle = \Gamma_{\phi,T} \frac{\partial \langle \phi \rangle}{\partial x_j} \tag{4.47}$$

This is a well-established practice, known as gradient-diffusion model, in simulations concerning scalar quantities (Marchisio and Fox 2016) and the simplest to be used. The turbulent diffusion $\Gamma_{\phi,T}$ is expressed as:

$$\Gamma_{\phi,T} = \frac{\nu_T}{Sc_T} \tag{4.48}$$

Where $Sc_T$ is the turbulent *Schmidt's number*, whose value is around the unity and for most applications it ranges between 0.7 and 1.

## 4.4 Multiphase model

Most common mixing applications for STR in the industrial field involve multiphase flows, such as gas-liquid system in fermentations, liquid-liquid mixing, solid particles dispersion in liquid solvents or emulsification of polar and non-polar substances.

At first it is useful to classify these flows based on the way the two or more phases interact, thus a multiphase system can be separated or dispersed. In a separated system the two phases have few, big interfaces, therefore resulting relatively segregated one from the other. In a dispersed flow, instead, one phase, called primary, is continuous, whereas the secondary one is in form of bubbles, droplets or solids particles. Stirred tanks are mainly applied for dispersion purposes, as the gas-liquid aerated vessel treated in this work.

The most important parameter to characterize a multiphase flow is the volume fraction (Andersson et al. 2012), determining distribution of phases in a certain volume. It is defined as in Eq. (4.49), with $N_k$ being the total number of phases and $V$ the total volume of the system.

$$\begin{cases} \alpha_k = \dfrac{\sum_i^{N_k} V_i}{V} \\ \sum_k \alpha_k = 1 \end{cases} \tag{4.49}$$

There are several multiphase models for dispersed systems and for sake of simplicity they can be summed up in: Euler-Lagrangian model and Euler-Euler model.

The Euler-Lagrangian model describe the primary phase as a continuum and the secondary phase as dispersed phase, the sum of a large number of individual particles. Thus, for the continuous phase the point of view is stationary, namely Eulerian, whereas for the dispersed one the observer moves with the particles. Trajectories are computed for all the particles, making this method computationally burdening, thus it can be only applied for system with low secondary phase volume fraction.

The Euler-Euler model, instead, describes both phases as continuous media for which the momentum and continuity equations are solved separately. The concept is to describe the two fluids as compenetrating, estimating a sort of average volume fraction in each position. This allows to describe even very complex system; however, closure models are necessary to

describe the interaction between fluids. This model is the one used in this work for the multiphase simulation. The governing equation are multiphase Continuity, Eq. (4.50), and Momentum balance equation for each phase, Eq. (4.51):

$$\frac{\partial \alpha_k \rho_k}{\partial t} + \frac{\partial (\alpha_k \rho_k U_{i,k})}{\partial x_i} = 0 \tag{4.50}$$

$$\frac{\partial (\alpha_k \rho_k U_{i,k})}{\partial t} + \frac{\partial (\alpha_k \rho_k U_{i,k} U_{j,k})}{\partial x_j} = -\frac{\partial \alpha_k p}{\partial x_i} + \frac{\partial \alpha_k \tau_{ij,k}}{\partial x_j} + \alpha_k \rho_k g_i + f_{i,k} \tag{4.51}$$

The last term of Eq. (4.49), $f_{i,k}$, represent the momentum exchanged between the two fluids at the interface. Usually it is expressed as the sum of the several interphase forces representing different physical phenomena (Oey 2005; Ranade 2001) for a gas-liquid system :

$$f_{i,k} = f_{D,i,k} + f_{L,i,k} + f_{VM,i,k} + f_{TD,i,k} \tag{4.52}$$

**Table 4.5** Definition of the terms composing the interphase forces in Eq. (4.52)

| | |
|---|---|
| $f_{D,i,k}$ | Drag force, due to the friction between bubbles and continuous phase |
| $f_{L,i,k}$ | Lift force, due to velocity gradient and particle rotation |
| $f_{VM,i,k}$ | Virtual mass, due to acceleration of the surrounding fluid |
| $f_{TD,i,k}$ | Turbulent dispersion force, due to turbulent fluctuations |

A brief summary of the equations models for these contribution, as reported in Fluent Theory guide (2017) and (Buffo and Marchisio 2014). For turbulent gas-liquid systems in stirred vessel, though, the main interaction contribution is given by the drag force (Petitti et al. 2010b), while the other forces can be neglected, at a first approximation.

### 4.4.1 Drag force

A Gas bubble rising is subject to buoyancy, which accelerates it upward, gravity and drag, between its surface and the fluid around, that decelerate it downward. Momentum transfer is, thus, the balance between those terms. Considering two phases *p*, dispersed, and *q*, continuous:

$$f_{D,i,k} = K_{pq}(U_{i,p} - U_{i,q}) \tag{4.53}$$

Where $K_{pq}$ is an interphase coefficient is expressed as:

$$K_{pq} = \frac{C_D Re_b A_{int} \mu_q}{8 d_b} \tag{4.54a}$$

$$Re_b = \frac{\rho_q |U_{i,p} - U_{i,q}| d_b}{\mu_q} \tag{4.54b}$$

$$A_{int} = \frac{6\alpha_p(1-\alpha_p)}{d_b} \tag{4.54c}$$

In which $Re_b$ is the relative Reynolds number, defined with respect to the relative velocity between phases, $d_b$ is the particle diameter and $A_{int}$ is the interfacial area concentration between phases per unit volume, expressed with the symmetric model, which is the default method for Ansys Fluent software.

Several methods are implemented in Ansys Fluent to model the $C_D$ coefficient, among which Grace et al. (1978), Tomiyama et al. (1998) and Schiller-Naumann (Ansys Theory Guide, 2013) were used.

Before describing these models, it is necessary to introduce two dimensionless number used to characterize the shape of bubbles, namely Eötvös and Morton number, the first representing the ratio between gravitational and interfacial forces, the second is similar but depends on the properties of the fluids:

$$Eo = \frac{g(\rho_p - \rho_q){d_b}^2}{\sigma} \tag{4.55a}$$

$$Mo = \frac{g{\mu_q}^4(\rho_p - \rho_q)}{{\rho_q}^2\sigma^3} \tag{4.55b}$$

Grace et al. (1978) model for the drag coefficient is:

$$C_D = max\left(min\left(C_{D_{ellipse}}, C_{D_{cap}}\right), C_{D_{sphere}}\right) \tag{4.56}$$

Where $C_{D_{ellipse}}$, $C_{D_{cap}}$ and $C_{D_{sphere}}$ are defined as:

$$C_{D_{sphere}} = \begin{cases} \dfrac{24}{Re}, & Re < 0.01 \\ \dfrac{24(1+0.15Re^{0.687})}{Re}, & Re \geq 0.01 \end{cases} \tag{4.57}$$

$$C_{D_{cap}} = \frac{8}{3} \tag{4.58}$$

$$C_{D_{ellipse}} = \frac{4}{3}\frac{g d_b}{{U_T}^2}\frac{(\rho_q - \rho_p)}{\rho_q} \tag{4.59}$$

Where:

$$U_T = \frac{\mu_q^4}{\rho_q d_b} Mo^{-0.149}(J - 0.857) \tag{4.60}$$

$$J = \begin{cases} 0.94H^{0.757}, & 2 < H \leq 59.3 \\ 3.42H^{0.441}, & H > 59.3 \end{cases} \tag{4.61}$$

$$H = \frac{4}{3} EoMo^{-0.149} \left(\frac{\mu_q}{\mu_{ref}}\right)^{-0.14} \tag{4.62}$$

And the standard value for $\mu_{ref}$ is $0.0009$ kg/m/s.

This model is suitable for system where bubbles can have a range of shapes (Bach et al. 2017).

Schiller-Nauman is the default method for Ansys Fluent. It was developed for rigid small spherical bubbles but is frequently used in numerical simulations with a range of shapes (Jahoda et al. 2009; Karimi et al. 2012; Valverde et al. 2016):

$$C_D = \begin{cases} 24(1 + 0.15Re_b^{0.687}), & Re < 0.01 \\ 0.44, & Re \geq 0.01 \end{cases} \tag{4.63}$$

Tomiyama et al. (1998), is a more also suited for system with a range of shapes, as for Grace model (Gradov et al. 2017):

$$C_D = max\left(min\left(\frac{24}{Re}(1 + 0.15Re_b^{0.687}), \frac{72}{Re_b}\right), \frac{8}{3}\frac{Eo}{Eo + 4}\right) \tag{4.64}$$

In some cases, it is necessary to take into account the effect of the turbulence on bubbles, for it may deeply affect results in terms of gas hold-up and dispersed phase distribution inside the system. Ansys Fluent has implemented the coefficient proposed by (Brucato et al. 1998). Originally, the Brucato modification was obtained for a liquid-solid system. Despite this, many authors empirically used it for gas-liquid systems, achieving good results. This drag modification coefficient ζ defines a new interphase coefficient as follow:

$$K'_{pq} = \zeta \, K_{pq} \tag{4.65}$$

And

$$\zeta = (1 + \lambda) \tag{4.66}$$

$$\lambda = K\left(\frac{d_b}{\eta}\right)^3 \tag{4.67}$$

Where $K$=6.5·10$^{-6}$ and is the Kolmogorov length-scale of Eq. (4.9).

### 4.4.2 Lift force

It represents the transverse force due to velocity gradients in the main flow field. It is equal to:

$$f_{L,i} = -C_L \alpha_p \rho_p (U_{i,p} - U_{i,q}) \omega_i \boldsymbol{\varepsilon}_{ijk} \tag{4.68}$$

With $\omega_i$ the vorticity, $\varepsilon_{ijk}$ the Levi-Civita operator and $C_L$ is the lift coefficient. For the latter several models exist, however a value of about 0.5 is quite common for spherical particles, both for bubbles and droplets.

### 4.4.3 Virtual mass force

The relative acceleration of a bubble with respect to the fluid around causes, in turn, an acceleration on the continuous phase, therefore, the inertia of the fluid to this motion acts as a force on the bubble.

$$f_{L,i} = -C_{VM}\alpha_p\rho_p\left(\frac{DU_{i,q}}{Dt} - \frac{DU_{i,p}}{Dt}\right) \tag{4.69}$$

This force becomes relevant when the difference between primary and secondary phase density is large.

### 4.4.4 Turbulent dispersion

As previously mentioned, turbulence can deeply affect a gas-liquid system, having strong effects on the interfacial forces and thus influencing bubble size, slip velocity and affecting turbulence intensity. Doing an averaging operation on the dispersion force, two terms emerge: the mean and the fluctuating one. The mean is expressed by modification of the drag coefficient, as done in §4.4., while the fluctuating part is the last term of Eq. (4.52), that can be expressed as (Buffo and Marchisio 2014):

$$f_{TD,i} = -C_{TD}\rho_q k_q \frac{\partial \alpha_p}{\partial x_i} \tag{4.70}$$

### 4.4.5 Turbulent multiphase models

The equations of motion and continuity, Eq. (4.50) and Eq. (4.51), of a turbulent system undergo the same procedure and operations used for the monophase system, reported in "subchapter 4.2". The additional equations for Standard *k-ε* model is also reported.

$$\frac{\partial \alpha_q\rho_q}{\partial t} + \frac{\partial \alpha_q\rho_q\langle U_{i,q}\rangle}{\partial x_i} = 0 \tag{4.71}$$

$$\frac{\partial\langle U_{i,q}\rangle}{\partial t} + \frac{\partial\left(\alpha_q\rho_q\langle U_{i,q}\rangle\langle U_{j,q}\rangle\right)}{\partial x_j} = -\frac{1}{\rho}\frac{\partial \alpha_q\langle p\rangle}{\partial x_i} + \nu_q\frac{\partial^2\langle U_{i,q}\rangle}{\partial x_j\partial x_j} - \frac{\partial\left(\alpha_q\rho_q\langle u'_{i,q}u'_j\rangle\right)}{\partial x_j} + \alpha_q g_{i,q} \tag{4.72}$$

$$\begin{aligned}\frac{\partial \alpha_q\rho_q k_q}{\partial t} + \frac{\partial\left(\alpha_q\rho_q\langle U_{i,q}\rangle k_q\right)}{\partial x_j} \\ = \nu_{T,q}\left[\left(\frac{\partial\langle U_{i,q}\rangle}{\partial x_j} + \frac{\partial\langle U_{j,q}\rangle}{\partial x_i}\right)\frac{\partial\langle U_{i,q}\rangle}{\partial x_j}\right] - \alpha_q\epsilon_q + \frac{\partial}{\partial x_j}\left[\alpha_q\left(\nu_q + \frac{\nu_{T,q}}{\sigma_k}\right)\frac{\partial k_q}{\partial x_j}\right]\end{aligned} \tag{4.73}$$

$$\frac{\partial \alpha_q \rho_q \epsilon_q}{\partial t} + \frac{\partial \left(\alpha_q \rho_q \epsilon_q \langle U_{i,q} \rangle\right)}{\partial x_j}$$

$$= C_{\epsilon 1} \alpha_q \nu_{T,q} \frac{\epsilon_q}{k_q} \left[ \left( \frac{\partial \langle U_{i,q} \rangle}{\partial x_j} + \frac{\partial \langle U_{j,q} \rangle}{\partial x_i} \right) \frac{\partial \langle U_{i,q} \rangle}{\partial x_j} \right] - C_{\epsilon 2} \alpha_q \rho_q \frac{\epsilon_q^2}{k_q} \tag{4.74}$$

$$+ \frac{\partial}{\partial x_j} \left[ \left( \nu_q + \frac{\nu_{T,q}}{\sigma_\epsilon} \right) \frac{\partial \epsilon_q}{\partial x_j} \right]$$

# 5 Numerical simulation set-up

The validation of the model was carried out using results from the PhD thesis of (Gabelle 2012) and Cappello (2019).

All the simulations of this work are 3D simulations and have been carried out with the commercial software ANSYS Fluent 18.2. The simulations were performed using a personal computer at IFPEN either locally with 16 GB of RAM and CPU with eight processors Intel® Xeon(R) CPU E5-1620 v2 @ 3.70GHz or in remote using the IFPEN cluster Ener 110. The cluster is made of 378 nodes, each one having two eight-core processors Intel Sandy Bridge 2.6 GHz and 64 Gb of memory. It was possible to select 16, 32 or 64 nodes for each simulation. the total power of calculation is 110 TFlops.

## 5.1 Computational grids

One of the main obstacles in systems such as stirred tanks is to find a method to simulate the impeller rotational motion, since it is the driving force of the all flow field.

Mesh models used to best describe systems in motion are *sliding mesh* (SM) and *multiple reference frame* (MRF) methods. In all these methods it is necessary to separate the impeller region from the surroundings, usually by detaching a cylinder which contains the turbine, as in "Figure 5.1".

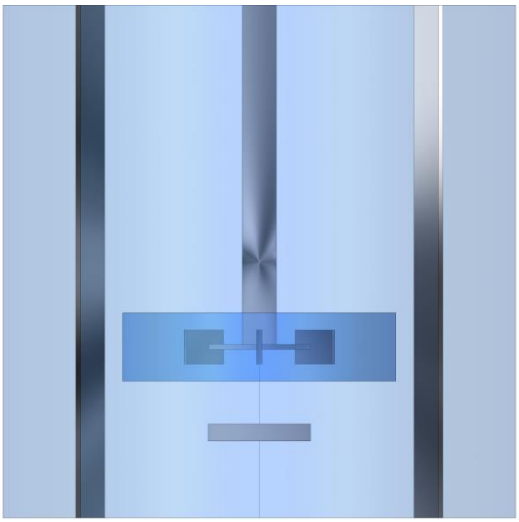

**Figure 5.1** STR geometry for CFD simulations with at the centre the moving area zone.

The sliding mesh method is an intrinsically transient method in which the computational grid containing the shaft, the impeller and its influenced region are in angular motion with respect to the stationary parts, such as the vessel walls, baffles and volume outside the moving part, and rotate of a small discrete step each time step. This method is able to accurately predict the flow field, the interaction between impeller and baffles as well as transitional phenomena inside the tank. However, the computational cost is high, and therefore less expensive method are preferred.

With the moving reference frame method, the cylinder containing the impeller and the shaft remains at rest while its reference frame is rotating with angular speed 2πN, the stationary parts are at rest as well. The motion of the reference frame generates forces, such as *Coriolis* force, which are included in the solution of the momentum equation, thus approximating a rotating system.

In the multiple reference frame, more than one reference frame is taken into account, considering only one positions of the impeller with respect to the baffles. Thus, even though this method is stationary, it is possible to approximate the interaction between moving parts and stationary one with a certain degree of accuracy, which was proven to depend on the interaction between the impeller and the baffles. To improve the accuracy a few different positions between impeller and baffles could be considered, but it would be necessary to create different meshes and then use an average value between all the configuration as results. This process would be time consuming.

The MRF method is far less computationally burdening respect to the SM method, allowing good prediction of the stationary behaviour of a STR. This is the methods used for all the simulations of this work.

### 5.1.1 Experimental equipment geometry

For this work, simulations were carried out using both single impeller configuration and double impeller configuration. Single impeller stirred tanks with liquid height H equal to tank diameter *T*, commonly referred or "square tanks, are widely used in several studies found in literature. Experimental data from PhD thesis of Gabelle (2012) and Cappello (2019), used for validating numerical simulations, were available for two diameters ($T$ =0.3 m, $T$ =0.6 m), all of whom equipped with a Rushton turbine, with six flat blades and four baffles. Impeller diameter $D$= 1/3 $T$ and the clearance between the bottom of the tank and the impeller $C$= 1/3 $T$, as in "Figure 3.1" and "Figure 3.2", impellers blade has a thickness of 2mm, which is also the minimum length of the geometry.

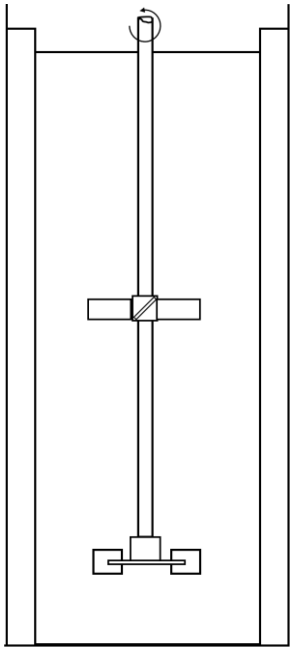

**Figure 5.2** Double impeller geometry simulated, with tank diameter $T$= 0.3 m.

The double impeller configuration, with liquid height $H = 2T$, more common in industrial applications, is the one used in the PhD thesis of Gabelle (2012) and from which hydrodynamics data for non-Newtonian fluids were used for validations. It has a diameter $T$=0.3 m, provided with one Rushton turbine at the bottom and 45° pitched blades at the top, with the same proportions as the single impeller configurations and four baffles.

### 5.1.2 Meshes used at IFPEN

Numerical grids can be divided in structured and unstructured meshes, the first ones are characterized by a uniform pattern, usually made of hexahedrons, whereas unstructured meshes have a more random pattern following the computational domain geometry, mainly formed by tetrahedrons and wedges.

Structured meshes usually have superior computational qualities, for they make solutions more stable and requires less cell per volume, compared to unstructured ones. However, implementation of good meshes requires long periods of time to be developed and specific software. In this work unstructured meshes were the most used, developed with the software Ansys Meshing, contained in the Ansys Workbench suite, with which it is possible to create quite straightforwardly good unstructured meshes. The parameters taken into account to evaluate mesh quality were mesh *skewness* and *orthogonal quality*. The first, which varies from 0 to 1, tell how cells are close to ideal shape, with 0 representing ideal shape, that is cube for hexahedral mesh and equiangular tetrahedrons for tetrahedral meshes, and 1 the most distorted shape. *Skewness* must be kept below 0.9 in order to have a stable solution but usually in order to reach good solutions it should be lower than 0.6-0.7. *Orthogonal quality* varies from 0 to 1 as well, with 0 representing the poor shaped cells and 1 being ideal conditions. The use of several mesh sizing in different areas of the mesh could greatly increase the distortion of cells and thus undermine stability and accuracy of the solution.

On a general basis when starting a simulation campaign, it is important to assess the independence of the solutions from the numerical grid, in order to minimize errors due to discretization of governing equations, especially with first order schemes. This is achieved by simulating the same system with the same operating conditions with an increasing number of cells. From a certain number on, the solutions won't change significantly, reaching a plateau. Thus, the optimal number of cells constituting the computational domain are determined.

For this work, however, this procedure was already done by previous works, and has already established that around 3 million cells were well enough to predict the hydrodynamics of turbulent monophasic system with water with an error below 5%. The grids used in this work are here presented in the following paragraphs.

#### a Tetrahedral mesh – single impeller tank

This mesh, shown in "Figure 5.3" has $2.90 \cdot 10^6$ cells, with mesh size in the stationary zone of 5 mm and of 2 mm in the MRF zone, impeller surface and sparger top wall with cells of 1 mm.

At boundary layers such as baffles, bottom and side walls three layer of small hexahedral cells, called inflation, were used. The cells in proximity of a boundary layer, should give a value of $y^+$, the dimensionless distance from the wall, between 30 and 300 to improve the accuracy of the predictions. Maximum skewness is equal to 0.67 and minimum orthogonal quality is 0.42.

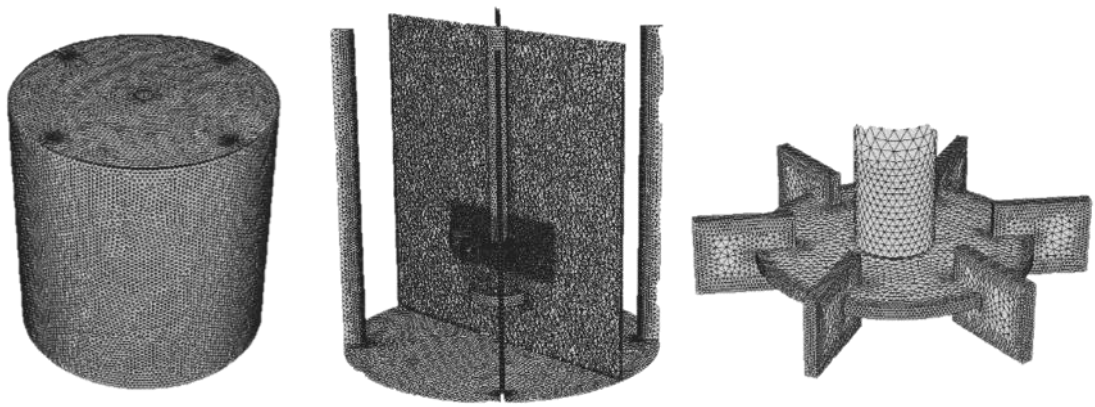

**Figure 5.3** Tetrahedral mesh – single impeller tank with $2.91 \cdot 10^6$ cells.

### b Tetrahedral mesh – double impeller tank

This mesh, shown in "Figure 5.3", has $4.24 \cdot 10^6$ cells, with mesh size in the stationary zone of 8mm, of 2mm in the MRF zone and impeller surface and sparger top wall with cells of 1mm. At boundary layers such as baffles, bottom and side walls three layer of inflation, were used. Maximum skewness is equal to 0.63 and minimum orthogonal quality is 0.45

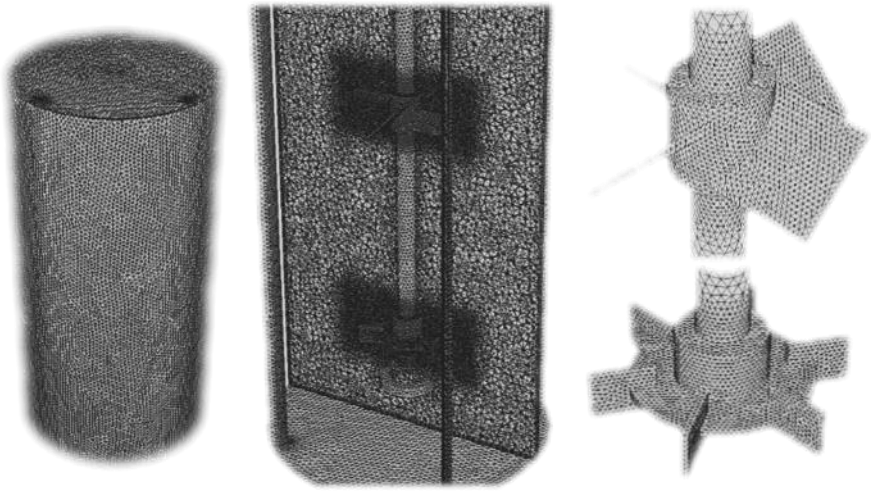

**Figure 5.4** Tetrahedral mesh – double impeller tank with $4.24 \cdot 10^6$ cells.

### c Hexahedral mesh – single impeller tank

This mesh, shown in "Figure 5.4" created at IFPEN by eng. Lionel Gamet of department R15, has $2 \cdot 10^6$ cells. It was mainly used for comparison with tetrahedral meshes and for scale-up simulations. In fact, obtaining results from a tetrahedral mesh comparable to those of a hexahedral, computationally more reliable, allows to use the former for more complex geometries. Additional simulations were performed with bigger diameters ($T$ =1 m, $T$ =4 m) for

scale-up purposes, by proportionally enlarging this mesh. Results could be only interpreted as an indication of what might be the hydrodynamic behaviour at much bigger scale.

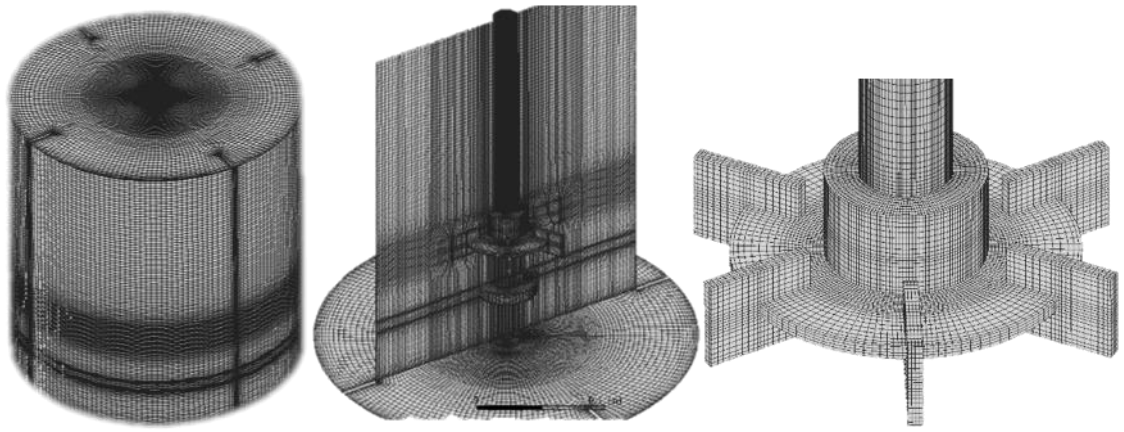

**Figure 5.5** Hexahedral mesh – single impeller tank with $2 \cdot 10^6$ cells.

In "Table (5.1)" the characteristics of the meshes are summarized:

**Table 5.1** Characteristics of the meshes used in this manuscript.

| Configuration | Single impeller tetrahedral mesh | Single impeller hexahedral mesh | Double impeller tetrahedral mesh |
|---|---|---|---|
| N° grid cells | $2.90 \cdot 10^6$ | $2 \cdot 10^6$ | $4.24 \cdot 10^6$ |
| Skewness | 0.67 | - | 0.63 |
| Orthogonal quality | 0.42 | - | 0.45 |
| Inflation at boundary layers | Three layers | No | Three layers |
| Minimum cell size | 2 mm in MRF zone, 0.75 mm on impeller surface, 5 mm in static zone | Structured mesh, 0.75 mm on impeller surface | 2 mm in MRF zone , 1.5 mm on impeller surface, 8 mm in static zone |

## 5.2 Models and methods

Both single phase and multiphase gas-liquid 3D simulations were performed with Ansys Fluent standard physical properties at 20°C, gathered in "Table 5.1":

**Table 5.2** Physical properties of materials

| Phase (substance) | Density ρ (kg $m^{-3}$) | Viscosity μ (Pa s) | Bubble diameter d (m) | Surface tension γ (N $m^{-1}$) |
|---|---|---|---|---|
| Liquid (water) | 998.2 | $1.003\times10^{-3}$ | - | 0.072 |
| Gas (air) | 1.225 | $1.7894\times10^{-5}$ | $3\times10^{-3}$ | - |

### 5.2.1 Turbulent methods and simulations set-up

The single-phase simulations were carried out in steady-state mode with *Realizable k-ε* model, Coupled algorithm with pseudo-transient under-relaxation coefficients enabled, to improve the computational time, the stability and convergence of the systems (Keating M. 2011) which is intrinsically time-dependent. Some comparisons with the standard *k-ε* model with SIMPLE algorithm were also performed.

The differencing schemes used were always second order Upwind in tetrahedral meshes and QUICK in the hexahedral one. The solutions were considered converged by combination of two factors: when normalized residuals value dropped below $10^{-6}$ for water and $10^{-4}$ for non-Newtonian fluids and when the value of a specific quantity, monitored during the simulation, were considered stable, e.g. for the flow field when *torque* or *dissipation rate* reach an asymptotic value.

### 5.2.2 Boundary conditions

At stirred tank walls (namely sides, bottom, shaft and impeller walls) the standard *no-slip velocity* condition was applied, that is fluid velocity vector is equal to zero at solid boundary. The top wall was considered a level at which the fluid has a stable free surface with a flat profile, thus a no shear, symmetry conditions was chosen. The impeller wall, being included in the MRF zone, was set as a moving wall with zero velocity with respect to the surrounding area, thus moving with same velocity as the moving reference frame. The impeller shaft, instead, was set as a moving wall with the same angular velocity as the impeller in the absolute frame of reference.

It was chosen to use the *enhanced wall treatment* as wall function, because since the first results it was noticed that dimensionless wall distance *y+* values were inferior to 10 along many areas of the walls of the stirred tank, whereas in turbulent layer it should be larger.

### 5.2.3 Multiphase set-up and boundary conditions

For the multiphase system were used the same turbulent models, both in transient and steady-state mode. Gas-liquid systems simulations can be very unstable and lead to divergence thus it is necessary, at least at the beginning, to use less restricting methods constraint in order to achieve more stable solutions. First order upwind with SIMPLE algorithm was the setup chosen

for transient simulations, increasing time steps from $10^{-6}$ to $10^{-3}$. Steady-state simulations setup used a first order at first and then second order UDS scheme and a Coupled algorithm, increasing Courant number to very low values, around $10^{-5}$ or less, in order to achieve more stable solutions.

Regarding gas-liquid interactions it was chosen the Euler-Euler dispersed model, mainly with Grace and Tomiyama drag law and Brucato drag modification coefficient enabled.

For gas bubbles was chosen the *slip* conditions, that is no shear between gas and the walls. Three different options were tried for the top surface: *pressure outlet*, *degassing* and *pressure outlet* at the top boundary of an extra air volume, added to the domain. The upper boundary conditions are important to ensure conservation of both phases and thus continuity equation solution. Using a *pressure outlet* require to specify the secondary phase backflow, namely the gas phase, to be one, imposing that all the mass eventually entering the computational domain from the top surface is air. *Degassing* conditions define a free surface at which only gas bubbles are allowed to escape. The last method, often used for bubble columns, is to add and additional computational domain, coarsely meshed, filled with only gas. The top surface is set as a *pressure outlet* with backflow equal to 1. This strategy, contrary to the previous ones, guarantees secondary phase mass conservation and results closer to real conditions, however, not only add computational cost to the simulations but could cause stability issues due to the distorted cells between the tank domain and the additional air pocket domain.

The top surface of the sparger was set as a *velocity inlet,* defining the velocity of the incoming secondary phase. The gas flow rate chosen, $Q_G$ = 1 $m^3/h$, is the same used during the experimental campaign. The inlet was configured by turbulence intensity, with a standard value of 5% and by *hydraulic diameter*, the ratio between the inlet cross section and its perimeter. The software allows to specify the velocity and the volume fraction of the input flow rate. Gas inlet velocity was calculated as the ratio between the sparger inlet area and the volumetric flow rate of the gas. The volume fraction indicates the fraction of computational cells which inputs the secondary phase. This parameter should be low, between 10% and 50%, at least as far as the gas flow is well established, because higher values often results in unstable simulations.

## 5.3 Validation parameters

As already stated in "Chapter 3" the values used to compare the experimental data with numerical results were mainly the impeller *power number* $N_p$ and the tank *mixing time* $\theta_{95}$.

### 5.3.1 Power number

From Eq. (3.8) a first expression for the power number, directly calculated from the value of the torque computed by the software is obtained:

$$N_{p,\Gamma} = \frac{2\pi\,\Gamma}{\rho N^2 D^5} \tag{5.1}$$

This expression is very commonly used to validate hydrodynamics, for instance in (Petitti et al. 2010a), and although values of $N_{p,\Gamma}$ thus calculated is often coherent with experimental data, it might not give right information regarding the turbulent flow inside the tank.

On a general basis it is well know the relationship between the energy dissipation rate and the power globally dissipated in a turbulent system:

$$\epsilon = \frac{P}{\rho V} \tag{5.2}$$

It is crucial to correlate the results of numerical solutions with the turbulent parameters because good accordance of these quantities give also god prediction of the flows inside the computational domain.

Thus, the power number is also calculated from the value of ε:

$$N_{p,\epsilon} = \frac{\int_V \rho\epsilon \, \mathrm{d}V}{\rho N^3 D^5} \tag{5.3}$$

### 5.3.2 Mixing time

This method was implemented in order to simulate the injection of a tracer inside the tank (a dye or a reactive substance) as reported in 3.2.1. During experiments by (Gabelle 2012) a defined volume of tracer was injected at a specified height of the vessel and one or more probes are then used to calculate the homogeneity of this specie, in particular conductometry was used for pure water system, whereas colorimetric essays were used for non-Newtonian fluids.

In CFD simulation an instantaneous injection is used, then the standard deviation is computed from the results. A scalar quantity, *user defined scalar* (UDS), is defined inside a fixed volume at a specified position of the tank, resembling the real injection position. It was seen that the normalized concentration ($C(t)/C_\infty$) profile of the scalar is independent from the volume injected, thus usually a volume equal to that of a sphere with 1 cm radius was marked inside the domain, and then it was patched with a constant value of 1 of $C(t)/C_\infty$.

Using the solutions of a previous simulation, the flow field is frozen and only the scalar transport equation is computed in a transient simulation, interrupting the simulation when the average standard deviation of the normalize concentration reaches a value equal to 5%, that is when the logarithm of the variance $\sigma^2$ is equal to -2.60. This method is known as the variance method (Paul et al. 2004).

The time step of the simulation is arbitrary but should be equal or inferior to the inverse of the radio velocity of the impeller N, namely the intrinsic frequency of the system.

Logarithm of the variance:

$$\log(\sigma^2) = \log\left[\left(\frac{C(t)}{C_\infty} - 1\right)^2\right] \tag{5.4}$$

Which can be implemented as follow:

$$\log(\sigma^2) = \log\left[\frac{1}{N_{cells}} \sum_{i=1}^{N_{cells}} \left(\frac{C_i}{C_\infty} - 1\right)^2\right] \tag{5.5}$$

With $C_i$ being the concentration at the *i*-th cell at the time step *n*-th, $C_\infty$ the volume average concentration of scalar in the computational domain and $N_{cells}$ is the total number of cells in the computational domain.

Ansys Fluent requires the definition of some *custom field function (CFF)*, defined as follow:

$$CFF_1 = \left(\frac{C_i}{C_\infty} - 1\right)^2 \tag{5.6}$$

$$CFF_2 = \sum_{i=1}^{N_{cells}} \left(\frac{C_i}{C_\infty} - 1\right)^2 \tag{5.7}$$

The results of $CFF_2$ are easily exported on Microsoft Excel where following Eq. (5.5) the value of $\theta_{95}$ can be extrapolated.

The final concentration $C_\infty$, is supposed to remain constant during the simulation, under the assumption of mass balance and absence of sink or sources for the scalar and being a batch system; indeed, the value slightly decreases but with a negligible effect on the final result.

The diffusivity of the UDS was implemented with a *user defined function* (UDF), reported in appendix B, which defines an isotropic effective diffusivity being the sum of the laminar term and the turbulent term, as explained in "Section 4.3". The turbulent Schmidt number $Sc_T$ was taken equal to 0.7, a default value for this kind of systems.

## 5.4 Complex rheology

The experimental data for non-Newtonian fluids where available for two different kind of substances, *xanthan gum* (XG), and *carboxymethyl cellulose* (CMC), both produced by Sigma-Aldrich, at different concentrations in order to reproduce peculiar operating conditions occurring during the fermentation. In particular, XG has a rheological behaviour closer to the real fermentation broth, but even in small concentrations create opaque solutions in water, thus making it less easy to observe flow pattern. CMC, on the other hands, despite being less similar, creates clearer solutions. Results of experiments are presented in “Figure 5.5” and Figure “5.6”.

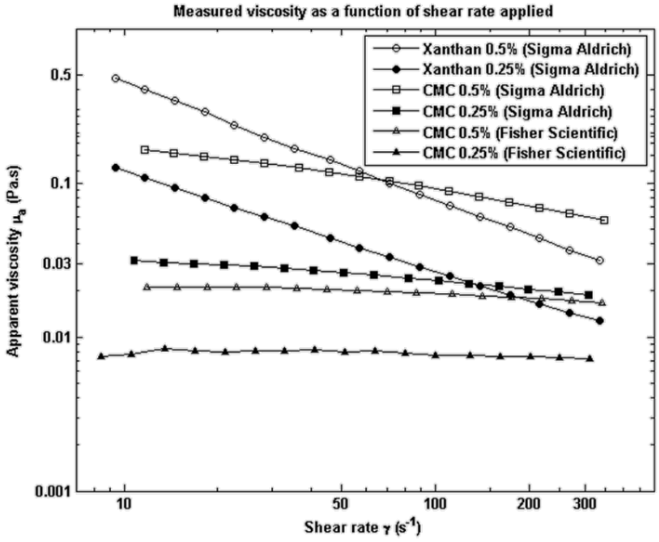


**Figure 5.6** Rheological experimental curves for Xanthan gum and Carboxymethyl Cellulose ( 0.25% and 0.5% by weight solutions with water ). Gabelle (2012).

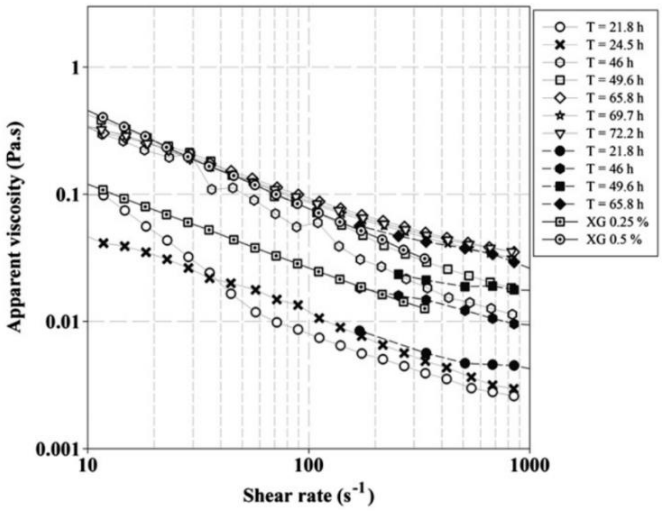


**Figure 5.7** Comparison between the rheology of the fermentation broth at different time in the process and model fluids. (Gabelle 2012).

### 5.4.1 Viscosity modification in transport equation

A complete set of experimental data for power number and mixing time was available only for the double impeller system, described in "Section 5.1.2". Ansys Fluent allows to modify the rheology by changing the viscosity from constant to a power law. The software computes the shear-stress τ and the shear-rate $\dot{\gamma}$ from the velocities obtained solving the transport equation, with Eq.s (3.9) and (3.10). In particular:

$$\dot{\gamma} \equiv \sqrt{2(\boldsymbol{D}:\boldsymbol{D})} \tag{5.8}$$

Where $\boldsymbol{D}$ is the rate of strain tensor, whose components $d_{i,j}$, already introduced in (§4.2) are defined as:

$$\boldsymbol{D} = \begin{bmatrix} \frac{\partial U_x}{\partial x} & \frac{1}{2}\left(\frac{\partial U_x}{\partial y}+\frac{\partial U_y}{\partial x}\right) & \frac{1}{2}\left(\frac{\partial U_x}{\partial z}+\frac{\partial U_z}{\partial x}\right) \\ \frac{1}{2}\left(\frac{\partial U_x}{\partial y}+\frac{\partial U_y}{\partial x}\right) & \frac{\partial U_y}{\partial y} & \frac{1}{2}\left(\frac{\partial U_z}{\partial y}+\frac{\partial U_y}{\partial z}\right) \\ \frac{1}{2}\left(\frac{\partial U_x}{\partial z}+\frac{\partial U_z}{\partial x}\right) & \frac{1}{2}\left(\frac{\partial U_z}{\partial y}+\frac{\partial U_y}{\partial z}\right) & \frac{\partial U_z}{\partial z} \end{bmatrix} \tag{5.9}$$

With this method were carried out the simulations on the double impeller system to investigate the coherence with experimental data.

The main issue with this procedure is that the velocities contained in Eq. (5.9) are mean values obtained through time-averaging of Eq.s (4.15) and (4.16), thus representing the mean flow. This method is effective when treating small geometries, but when proportions increase during scale-up, this could lead to errors, not predicting possible heterogeneities due to bigger dimensions of the system. An alternative, more locally oriented, was investigated.

### 5.4.2 Alternative viscosity computation method

A rigorous approach to address the modification of the transport equations for complex fluids was proposed by (Gori and Boghi 2011, 2012) which obtained a new complete set of transport equations for a turbulent system using a generalized expression for apparent viscosity. The approach is certainly interesting giving the opportunity to acquire data locally, but it requires to implement the whole new set in the software and potentially seemed computationally burdening. In (Sánchez Pérez et al. 2006) the shear rate is expressed as:

$$\dot{\gamma} \equiv \left(\frac{1}{\mu}\frac{P}{V}\right)^{\frac{1}{2}} \tag{5.10}$$

Thus, being power input $P$ related to dissipation rate ε from Eq. (5.2) and $\mu_a$ expressed with Eq. (3.10), the expression becomes:

$$\dot{\gamma} \equiv \left(\frac{\rho\epsilon}{K}\right)^{\frac{1}{n+1}} \tag{5.11}$$

This expression is related to the dissipation rate, which is a value the software compute for each cell of the grid, thus a local value which modify the *molecular viscosity*. Thus, a UDF, reported in appendix B, was implemented in the software and a comparison at large dimensions with the solution calculated with the standard Ansys Fluent method was done. These simulations were done using the single impeller hexahedral mesh of "Section 5.1.3". The setup used during simulations was the same as for the single-phase mono impeller tank, described in "Section 5.2", except for the modifications of the liquid viscosity.

## 5.5 Fed-batch and particle tracking simulations

During industrial fed-batch fermentations in large-scale bioreactors the non-ideal mixing, due to the heterogeneities in the flow field enhanced by the non-Newtonian behaviour of the broth, can result in sharp gradients of substrate concentration inside the tank. The lack of a homogeneous distribution of glucose affects the desired product yield since microorganisms, which circulate in the vessel following the main hydrodynamic loops, are subject to a time-varying intake of substrate, with a direct impact on their metabolism. Therefore, acquiring a deeper understanding of the extracellular environment which microorganisms experience allows to reproduce these conditions in a small-scale reactor in laboratory, in what is called a *scale-down* approach and thus investigate their behaviour.

In literature first Lapin et al. (Lapin et al. 2004; Lapin et al. 2006) proposed a Euler-Lagrange analysis by treating the flow field as a continuum with a Eulerian approach and the microorganisms as discrete particles with a Lagrangian one. The work highlights the importance of tracking the trajectories of individual particles, which ideally represent cluster of microorganisms, in the vessel, comparing them to the *lifelines* of cells crossing different substrate concentration zones. The metabolism of the microbial population is deeply dependent to their previous *history*, meaning the behaviour in a determined point in the tank at a certain time is the consequence of initial conditions. Further on Haringa et al. used this method (Haringa et al. 2016; Haringa et al. 2017) to simulate an industrial bioreactor for the production of penicillin, introducing a good methodology for this kind of analysis.

### 5.5.1 Description of the methods

The flow field must be solved with the same methods as reported in "Sections 5.2, 5.3, 5.4". A *source* and a *sink* of the substrate are implemented in the simulation, representing respectively the feed at the top of the vessel and the microorganism sugar depletion kinetics. Then, after freezing the momentum and continuity equations, the transport of the substrate is solved, allowing to assess the sugar concentration distribution throughout the vessel and to identify different areas in the bioreactor. Three different zones can be defined, namely *excess (E)*, *limitation (L)* and *starvation (S)* areas. Usually high concentration of substrate promotes growing of the population, inhibiting production of metabolites, such as enzymes. Very low concentration, instead, lead to starvation of the microorganism and reduction of the total productive biomass. In between these thresholds, the cells produce the desired product, thus it is important that most of the microbial population spend large amount of time in this area. The thresholds are identified based on the microorganism own kinetic of growth and production of secondary metabolites.

Lifelines of cluster of microorganisms are tracked by means of a discrete particle Lagrangian simulation. The number of particles simulated is arbitrary and it can be assumed that, by rule of thumb, the bigger the size of the vessel the greater the number of particles. The starting

position can be arbitrarily assumed, although a good assumption could be to distribute the starting point evenly throughout the tank or to use a single point at the level of the impeller. The time-step and physical time of the simulation are set by comparing them to *recirculation time* $\tau_c$ of the vessel as well as to the *mixing time* $\theta_{95}$ and the characteristic time constant of the substrate consumption kinetic. These three quantities can largely differ from one another, thus, trade off values between accuracy and simulation time must be chosen.

The particles motion, then, will be inherently a random walk but strongly influenced by the turbulent flow inside the tank, with simulated organisms being entrapped by the main recirculating loops.

Lifelines trajectories in function of the time can be then processed to obtain a statistic of the results.

A useful method is that of keeping track of the time elapsed between two subsequent passages from a certain region of the bioreactor, namely those ones previously defined on the base of their concentration of substrate (*E, L, S*). Finally, a passage frequency distribution as a function of the time spent can be made.

### 5.5.2 Kinetic model and discrete particle simulation set-up

The simulations carried out for this work were not meant to give complete results but can be regarded as a first approach to the methodology.

The substrate depletion was simulated on a previously solved flow field for a non-Newtonian fluid, namely CMC 0.5%. The glucose concentration is computed as a scalar quantity with the same chemical properties, that is density ρ and diffusivity $D_G$. Microorganism kinetics used is based on previous studies conducted at IFPEN on *T. reesei*.

Defining *X* and *S*, respectively the mass concentration of biomass and of substrate in the bioreactor, the metabolism of the *fungi* depends on S. Above a critical value, $S_{crit}$, the microorganism grows whereas below this value it produces enzyme. The split in metabolism is described by the empirical function *y*:

$$y = \frac{1}{2}\tanh(A(S - S_{crit})) + \frac{1}{2} \tag{5.13}$$

Where the constant $A$= 20 and the $S_{crit}$= 0.3 kg/m$^3$. The growth rate is expressed with an equation similar to the Monod model:

$$\mu = \mu_{max}\frac{S}{(K_{S,\mu} + S)} \cdot y \tag{5.14}$$

With $\mu_{max}$= 0.08 s$^{-1}$ being the maximum growth rate at the asymptote and $K_{S,\mu}$= 0.05 kg/m$^3$ the half-velocity concentration, namely the concentration of sugar at which $\mu/\mu_{max} = 0.5$ . The enzyme production $q_p$ is expressed as:

$$q_p = \left(q_{p,max}(1 - y) + q_{p,min}\right)\frac{S}{(K_{S,P} + S)} \tag{5.15}$$

With $q_{p,max}$=0.015 and $q_{p,\min}$= 0.002 kg/kg/s being the unit mass of enzyme per unit mass of biomass per second maximum and minimum production. $K_{S,P}$= 0.001 kg/m$^3$ being the analogous to $K_{S,\mu}$ referred to the enzyme. The consumption of sugar is described by:

$$q_S = \frac{\mu}{Y_{X,S}} + \frac{q_p}{Y_{P,S}} \tag{5.16}$$

With $Y_{P,S}$ and $Y_{X,S}$ representing the efficiency of conversion of sugar into enzyme or biomass. Both efficiencies are assumed equal to 0.5 kg/kg respectively of unit mass of enzyme or biomass per unit mass of sugar.

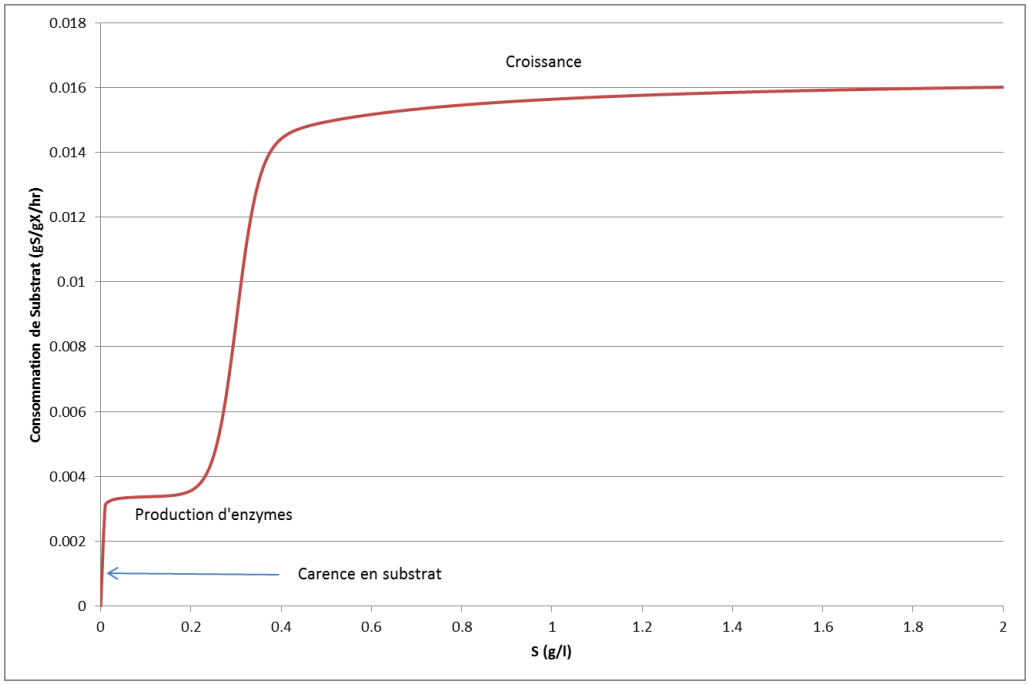


**Figure 5.8** *T.reesei* metabolism vs. substrate concentration.

Combining Eq. (5.13 – 16) to the consumption of sugar:

$$\frac{dS}{dt} = -X \cdot \left[ \frac{\mu_{max} \cdot S \cdot y}{Y_{X,S} \cdot (K_{S,\mu} + S)} + \frac{S \cdot (q_{P,max} \cdot (1 - y) + q_{P,min})}{Y_{P,S} \cdot (K_{S,P} + S)} \right] \tag{5.17}$$

Thus, the total substrate consumption is described by a kinetic law taking account of all these processes, Eq. (5.17), the one implemented as a UDF in the software, reported in "Appendix C". The *source* of sugar is defined as a surface detached from the computational domain in which there is a constant flowrate of substrate. Each computational cell contained in the *source* surface provides an input flow of scalar with constant velocity and volume fraction. These two parameters were chosen in order to represent the effect of a very low flowrate as in the fed-batch fermentation, thus it does not affect the global and local flow field. To simulate the depletion, in each of the remaining cells of the computational domain a *negative source* of scalar was set, following Eq. (5.17).

Microorganisms trajectories can be calculated directly by the software Ansys Fluent with a discrete Lagrangian simulation. The microorganisms are set as massless, with *random walk* motion and influenced by turbulence.

The sampling area, crossed by the particles, was first defined as an iso-surface having a concentration of scalar above the threshold value and detached by marking it. The volume incorporated inside the surface was defined as a new zone in the computational domain. The solver, then, tracks the instants the particles cross the detached surface in and out. Finally, the results are written in a text file that can be analysed with Microsoft Excel.

# 6 Results

In the following paragraphs the numerical simulations results will be presented and confronted with experimental data or correlations for validation.

## 6.1 Validation of the turbulent model

The validation of the hydrodynamics was carried out by simulating mixing of water in the smaller tank $T_{30}$ with volume of 0.021 $m^3$ and diameter of 0.3 m. The computational grid consists of a tetrahedral mesh of $2.9 \cdot 10^6$ elements. The turbulent model is *Realizable k-ε*, in steady state mode and pseudo-transient underrelaxation coefficients enabled. In all the following simulations the normalized residuals for continuity and momentum equations were well below $1 \cdot 10^{-6}$, thus, to be considered converged.

### 6.1.1 Power number

The power number, both $N_{P,T}$ and $N_{P,\varepsilon}$ of Eq.s (5.1) and (5.3), are compared with the experimental value, $N_{P,exp} = 3.93$ (Gabelle et al. 2012), obtained for the same tank. Simulations were performed at increasing impeller speed $N$, from 25 rpm, at which the system is at the threshold of the turbulent regime, to 800 rpm, point at which the turbulence is fully developed throughout the vessel. "Figure 6.1" shows the values of power number calculated as a function of the impeller speed, namely in function of increasing value of Reynolds number for the tank of Eq. (3.2).

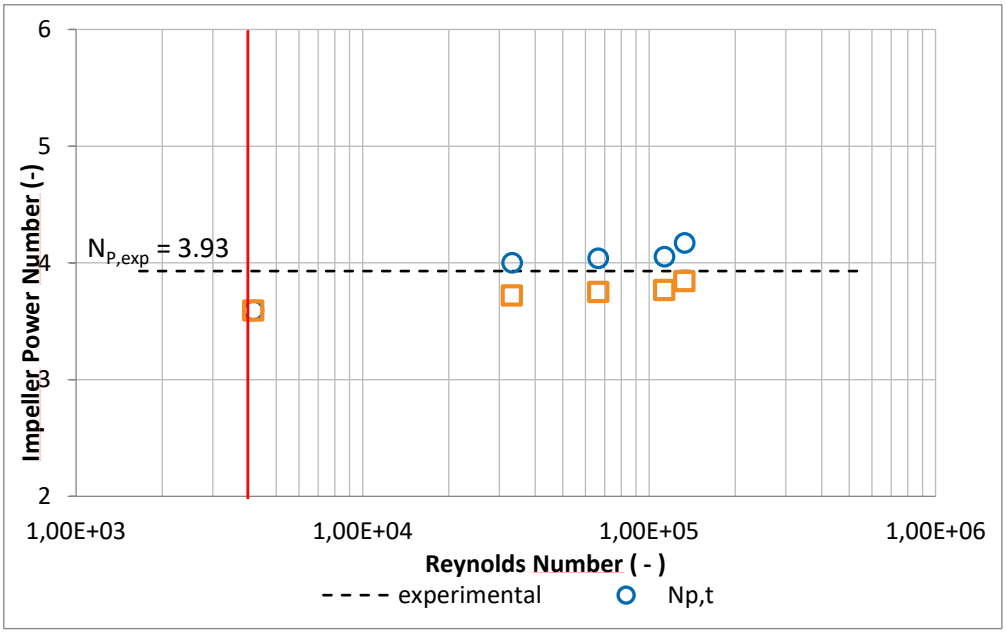


**Figure 6.1** Estimated power number NP at different Reynolds number. – ○ $N_{P,T}$ □ $N_{P,\varepsilon}$. Dashed horizontal line representing $N_{P,exp}$= 3.93, red line representing $Re$ = 4000.

The value of $N_{P,T}$ calculated from the torque on the shaft tends to overestimate the experimental value, whereas $N_{P,\varepsilon}$, on the contrary, tends to underestimate it. This gap between the two quantities is expected but both their relative difference and the error with respect to the experimental $N_p$ fall below a tolerated error of 15% – 20 %. Thus, the *Realizable k-ε* model is capable of well predict the global hydrodynamics with water. The accuracy, as well, tends to increase with the intensity of the turbulence and this is in accordance with the fact that all *k-ε* models hypothesizes a fully developed turbulent regime.

### 6.1.2 Mixing time

No direct experimental values were available for $\theta_{95}$ in the mono impeller configuration. Thus, the results of the simulations were interpreted using one of the several correlations found in literature, specifically developed by *Ruszkowski* for square tanks with Rushton mono impeller configuration (Grenville et al. 1992):

$$\vartheta_{95} = 5{,}91 T^{\frac{2}{3}} \left(\frac{\rho V}{P}\right)^{1/3} \left(\frac{T}{D}\right)^{1/3} \tag{6.1}$$

The injection point of the scalar quantity, namely the tracer, following the methods of "Section 5.3.2", was implemented by marking a spherical area of the tank, identifying the venter by its cartesian coordinates with a radius of about 0.01 – 0.015 m. The cells belonging to the area were set with a fraction of tracer equal to 1. "Figure 6.2" shows the point of injection of the scalar tracer with respect to the computational domain. Turbulent *Schmidt number* was set equal to 0.7.

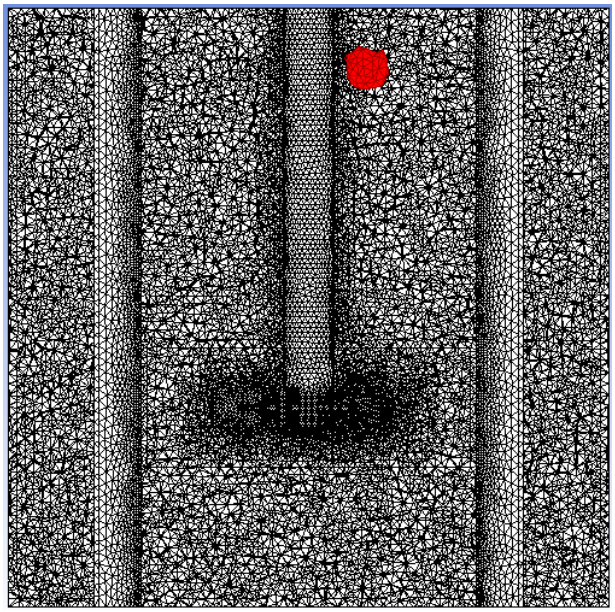

**Figure 6.2** The injection point (in red) of the scalar tracer inside the computational domain representing the simulated tank.

The simulation were performed in transient mode, using a time step equal to 0.01 s, with a frozen flow field, that is the algorithm solves only the scalar transport equation. A comparison between the results given by the models *Realizable k-ε* and *Standard k-ε* was done.

The results obtained with both models show good accordance with the empirical correlation, in particular the values of mixing time calculated with *Realizable k-ε* has relative errors below 10%. Overall both models are capable of good prediction of the system global dynamics with water as simulated fluid.

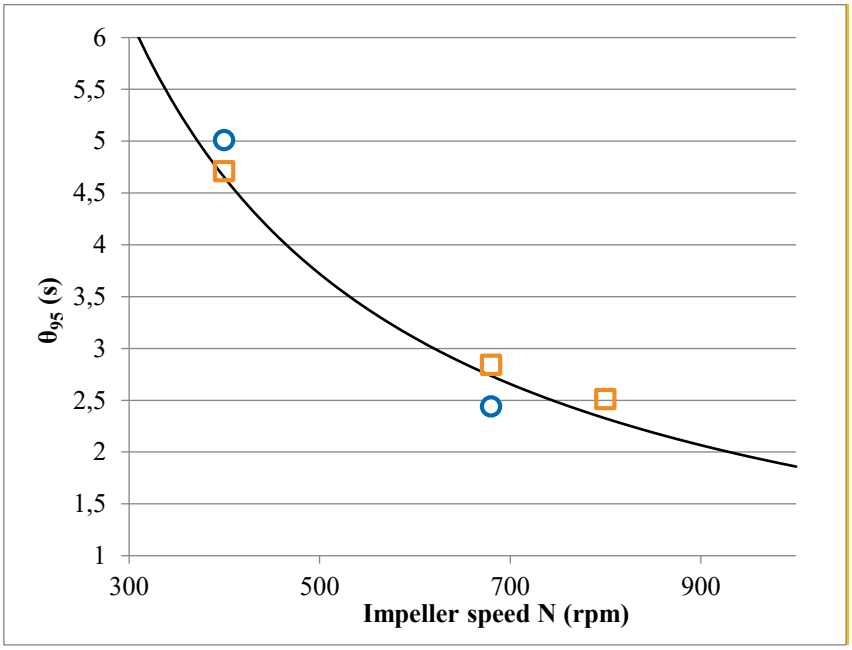


**Figure 6.3** Estimated mixing time $\theta_{95\%}$ at different impeller speed.
○ STANDARD k-ε; □ REALIZABLE k-ε; — Ruszkowski correlation.

## 6.2 Non-Newtonian fluids simulations

Simulations with CMC and XG were done on the double impeller tank configuration, described in "Section 5.1.2", to validate experimental data available. *Power number* ($N_{P,exp}$= 5.22) and *mixing time* were used to investigate the validity of the model chosen to describe those systems. Further simulations were carried out to investigate the behaviour of non-Newtonian fluids in the single impeller system with different dimensions.

Overall, these simulations were able to reproduce peculiar features of non-Newtonian systems such as: the *"cavern"* developed at low impeller speed and stagnant areas distant from the impeller, the global trends of *power number* and *mixing time* and changes with respect to water simulation, despite the fact that not all the results were in complete agreement with the experiments. Simulations were considered converged when normalized residuals for continuity and momentum equation were below $1 \cdot 10^{-5}$ and the values of *torque* and *dissipation rate* computed reach a steady value.

### 6.2.1 Power number

The double impeller tank was simulated with Water, CMC 0.5% and XG 0.25% at different impeller speed, with the same method as in "Section 6.1.1" and using the rheological

modification to the turbulent model provided by the software Ansys Fluent, described in "Section 5.4".

"Figure 6.4" shows that the results of the simulations are consistent with those obtained for the double impeller system. The model chosen seems to be able to give a good estimation of the power dissipated by the stirred tank. This is in accordance with the fact that most of the energy dissipation occur in the area around the impeller, area at which the apparent viscosity of both the non-Newtonian fluids, because of the great turbulence, is very close to viscosity of water. In fact, at lower velocities, namely 200 rpm, values of $N_P$ for both CMC and XG have larger errors. At that impeller speed, both the non-Newtonian fluids are in between transient and turbulent regime so that the turbulent models are probably not well representative of the system.

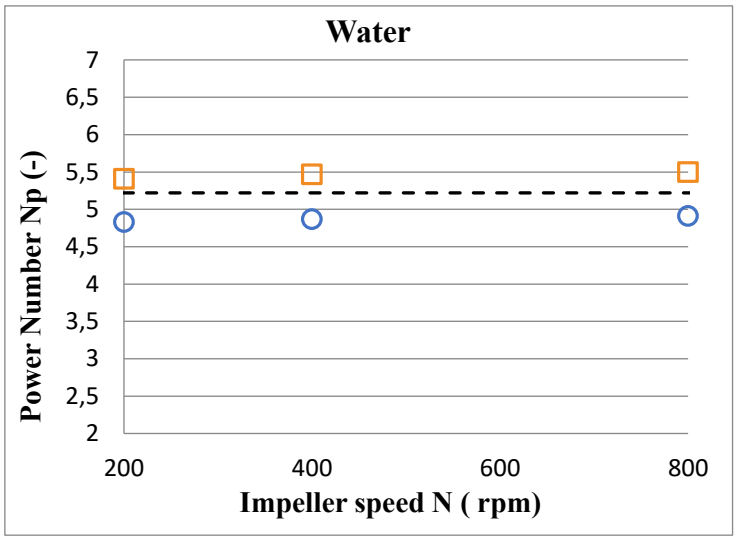


**Figure 6.4A** Power number in function of impeller speed – water. --- $N_{P,exp}$ ; ○ $N_{P,\varepsilon}$ ; □ $N_{P,T}$.

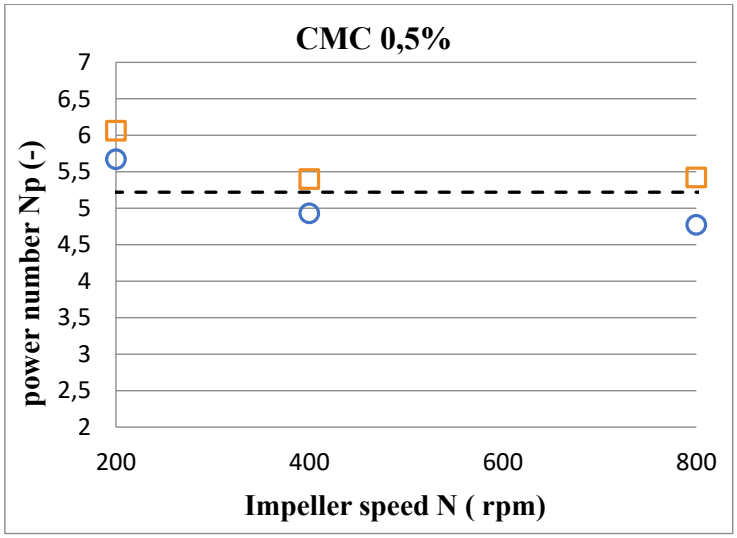


**Figure 6.4B** Power number in function of impeller speed – CMC 0.5%. --- $N_{P,exp}$ ○ $N_{P,\varepsilon}$ □ $N_{P,T}$.

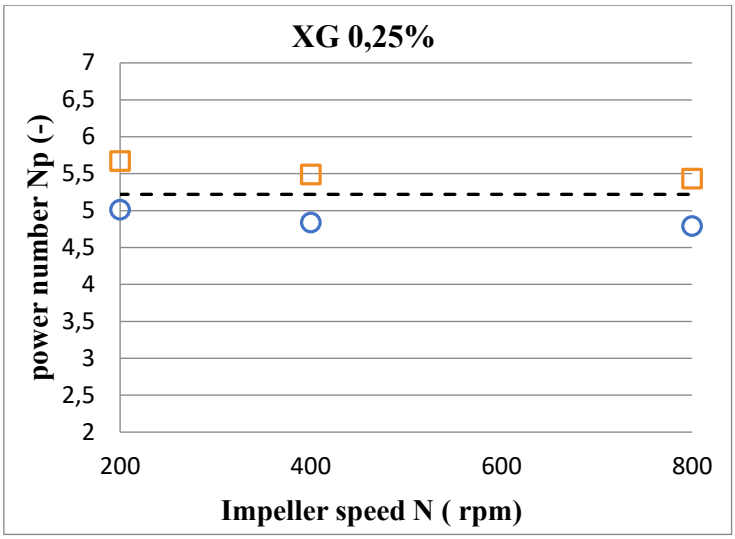


**Figure 6.4C** Power number in function of impeller speed – XG 0.5%. --- $N_{P,exp}$ ○ $N_{P,\varepsilon}$ □ $N_{P,T}$.

### 6.2.2 Mixing time

The methods of the simulation are the same as in "Section 6.1.2". The injection point was chosen in order to mimic the experimental one right above the pitch blade top impeller, as shown in "Figure 6.5":

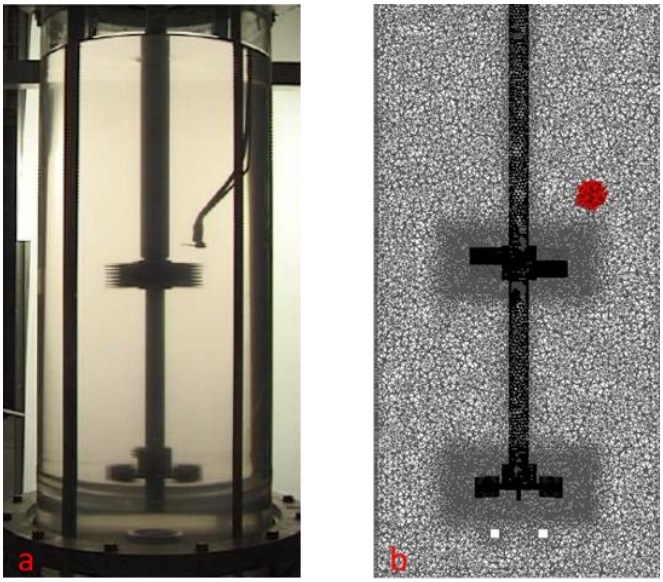


**Figure 6.5** a) the experimental apparatus with the syringe injector; b) the computational grid with the injection point, in red.

The same velocity range as in the previous section was applied. The results obtained, shown in "Figure 6.6", show that the simulated mixing time is not in complete accordance with experimental data. Firstly, considering water, at low speed (200rpm, 400rpm) the relative error, compared to the experimental values, are around 30%. Moreover, considering non-Newtonian fluids, the difference between the experimental values and the simulated ones is even wider. CMC results are closer to water ones, whereas XG simulations show the greatest gap. Instead, at the highest velocity (800 rpm) the values are consistent with experimental data.

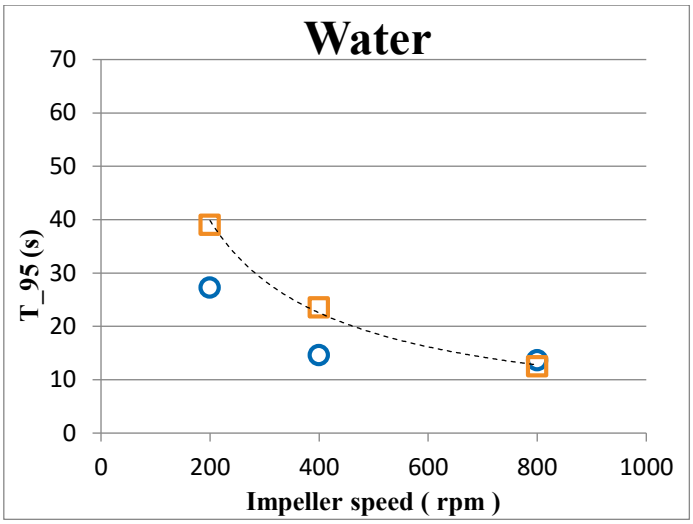


**Figure 6.6A** Mixing time in function of impeller speed – Water. ○ $\theta_{95,sim}$ □ $\theta_{95,exp}$.

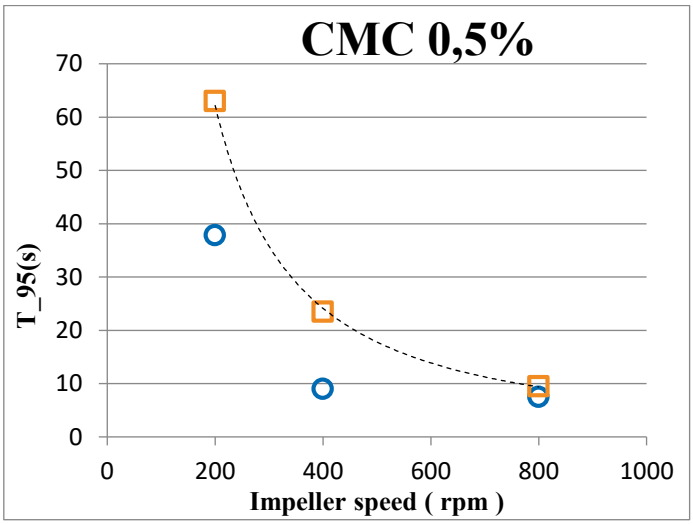


**Figure 6.6B** Mixing time in function of impeller speed – CMC 0.5%. ○ $\theta_{95,sim}$ □ $\theta_{95,exp}$.

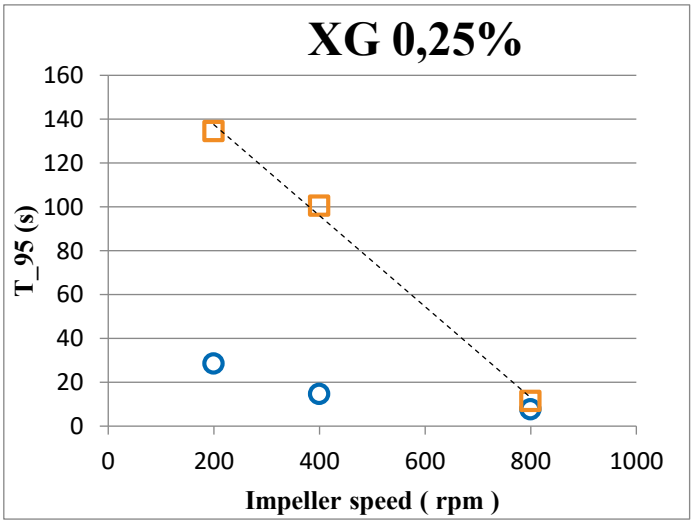


**Figure 6.6C** Mixing time in function of impeller speed – XG 0.25%. ○ $\theta_{95,sim}$ □ $\theta_{95,exp}$.

Although the poor performances in terms of precise values of mixing time, the model is able to predict their overall trend of decreasing time $\theta_{95}$ at increasing velocities. The reason behind these inconsistencies at low speed is due to the fact that $k$-$\varepsilon$ models assume the system to be homogeneously turbulent throughout the whole vessel, whereas in double impeller configuration, in particular with non-Newtonian fluids, this assumption is not valid for large part of the bioreactor, which, because of low shear rate, are stagnant.

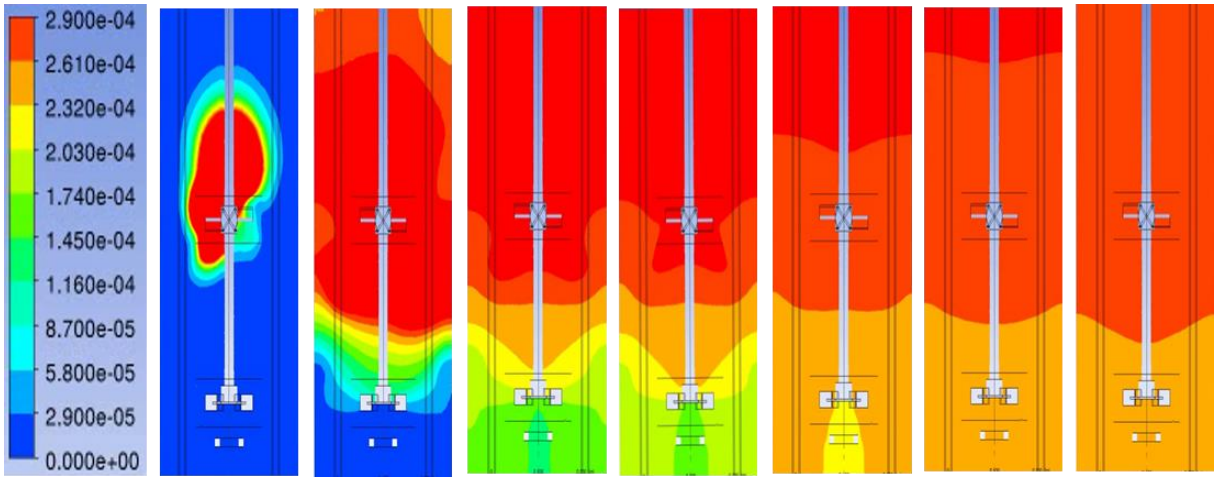


**Figure 6.7** snapshot of the scalar concentration field for CMC 0.5% at 400 rpm with *Realizable k-ε* .

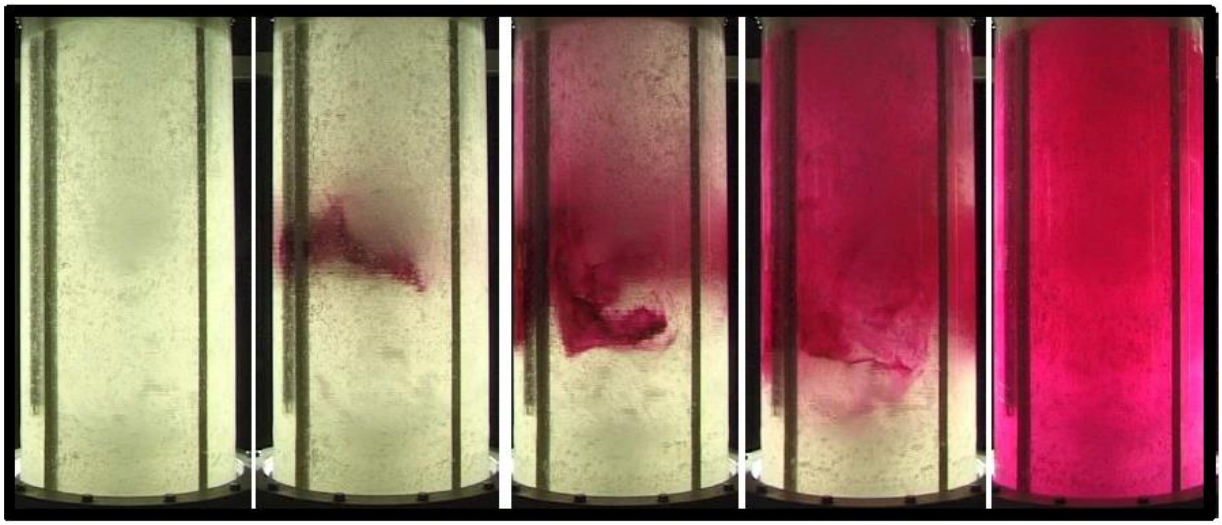

**Figure 6.8** picture of the experimental tank during mixing time test with dye tracer with CMC 0.5%

"Figure 6.7" compared with the experimental system of "Figure 6.8" indicate how the overall mixing process is simulated, showing the same stagnant area at the bottom of the tank with a lower concentration of tracer throughout the mixing.

An additional set of simulations were carried out on the monophasic system, despite the fact that no experimental data were available, to investigate the behaviour of such a system with non-Newtonian fluid and compare it to water simulations.

### 6.2.3 Mono-impeller system

An additional set of simulations were carried out on the monophasic system, despite the fact that no experimental data were available, to investigate the behaviour of such a system with non-Newtonian fluid and compare it to water. For these simulations the hexahedral mesh, with 2 million cells, was used, in steady-state mode, *Realizable k-ε* model, *pseudo-transient* underrelaxation coefficient enabled with Coupled velocity-pressure algorithm. *Power number* and *mixing time* were the parameters investigated for both 0.021 $m^3$ and 0.170 $m^3$ tanks, called respectively $T_{30}$ and $T_{60}$ with CMC 0.5%.

A complete set of simulations of flow field to determine the *power number* as a function of impeller speed $N$ were done only on the $T_{30}$ tank, whereas the few simulations of the $T_{60}$ tank confirmed the same values. The *power number* theoretically should be not affected by the rheology, especially with shear-thinning fluids, which around the impeller behave approximately as water, thus the reference value was $N_{P,exp}$= 3.93 was used for comparison. Results of "Figure 6.9" show the same trend as with the double impeller system, although the relative error of both $N_{P,T}$ and $N_{P,\varepsilon}$ with the experimental value is wider and $N_{P,T}$, which is usually higher than $N_{P,exp}$, results lower. Despite these facts, the errors, below 20%, were still considered acceptable, thus no further investigation were done in this direction.

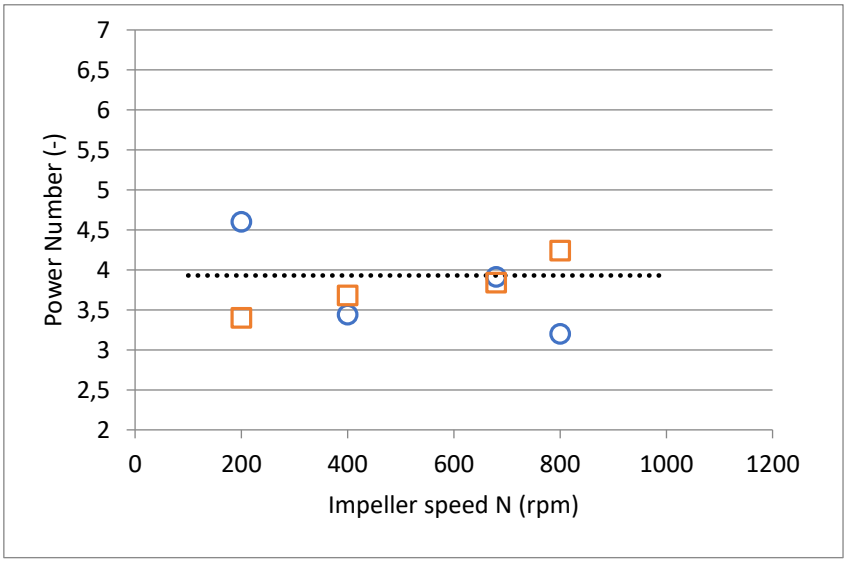


**Figure 6.9** Estimated *power number* at increasing impeller speed for CMC 0.5% in $T_{30}$ (T=0.3 m) tank. ○ $N_{P,\varepsilon}$ □ $N_{P,T}$

Also, the *mixing time* gave similar results, shown in "Figure 6.10", confirming the trend of an increase of $\theta_{95}$ with the complex rheology. Regarding the values of $\theta_{95}$, no confirmation with experiments was possible. Comparison of the two histograms of "Figure 6.10", confirms that increasing the scale of the tank makes more challenging the mixing and thus the *mixing time* in $T_{60}$ with CMC 0.5% increases more than in $T_{30}$. Impeller speed was set respectively at 680 rpm for $T_{30}$ and 170 rpm $T_{60}$ to achieve the same Reynolds number Re = 113333.

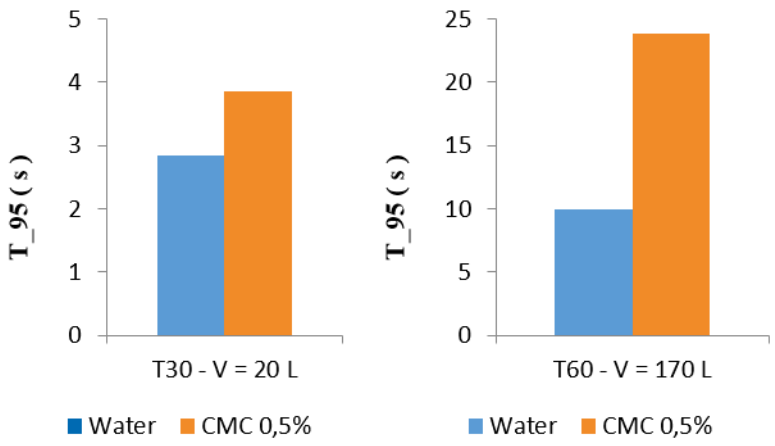


**Figure 6.10** Mixing time for $T_{30}$ and $T_{60}$, respectively on right and left.

Finally, a last set of qualitative simulations on the $T_{60}$ tank were run at very low speed, N= 35 rpm. At this speed the system with water is already in fully developed turbulent regime, whereas with XG 0.5% Reynolds number Re = 29, thus theoretically laminar. The comparison was done in order to verify if the turbulent model was able to simulate the presence of the "*cavern*" ("Section 3.1") at low Reynolds number.

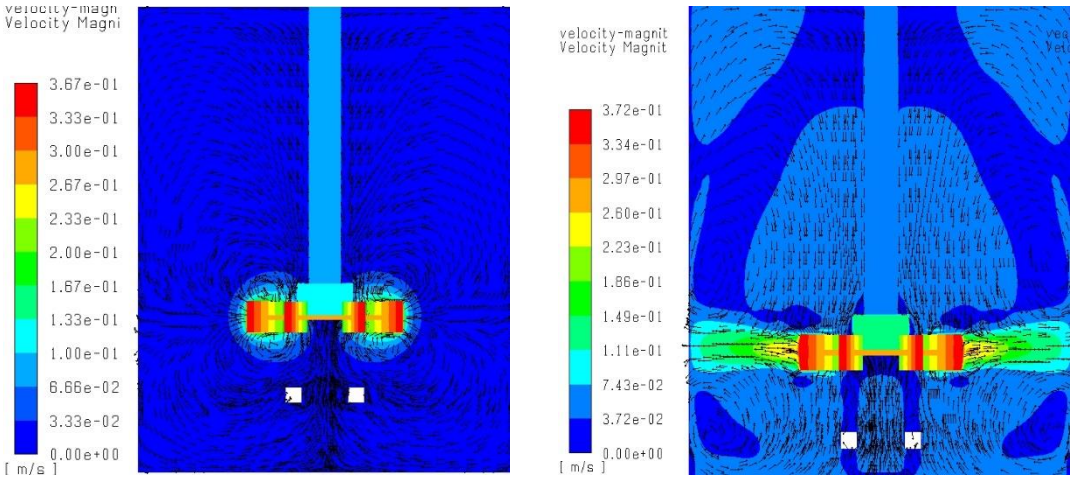


**Figure 6.11** Contour of the velocity magnitude field in the $T_{60}$ tank at 35 rpm. XG 0.5% on the left side, water on the right side.

"Figure 6.11", showing the contour of the *velocity magnitude* field, confirms that the model is able to predict the formation of a caver of moving liquid around a stagnant area in the presence of a shear -thinning fluid such as XG.

### 6.2.4 Modification of molecular viscosity

By means of a UDF the molecular viscosity was modified, following the method reported in "Section 5.4.2", allowing to compute the shear-rate $\dot{\gamma}$ from the local value of ε, following Eq. (5.11), thus providing a more local approach.

Simulations were carried out on the hexahedral mesh ( “Section 5.1.3”) comparing results obtained with the standard Ansys Fluent method, used in previous sections “6.2.1,6.2.2,6.2.3”.

The mesh was proportionally scaled up to obtain larger tanks, in order to investigate the effects of rheology at larger scale, where, it was supposed the standard Fluent method could, eventually, fail to give good prediction, because of its reliance on the mean velocities of the flow (obtain with method of “Appendix A”), instead of local ones.

The system was scaled up using the same dissipated power per unit volume $P_0/V$ (kW/m$^3$) as scaling parameter. Common industrial conditions for power dissipation are in the range between 2-3 kW/m$^3$ to 5-6 kW/m$^3$. The value chosen for these simulations was $P_0/V$ = 2.7 kW/m$^3$. The volume of the tank is 50 m$^3$, with a diameter T= 4 m.

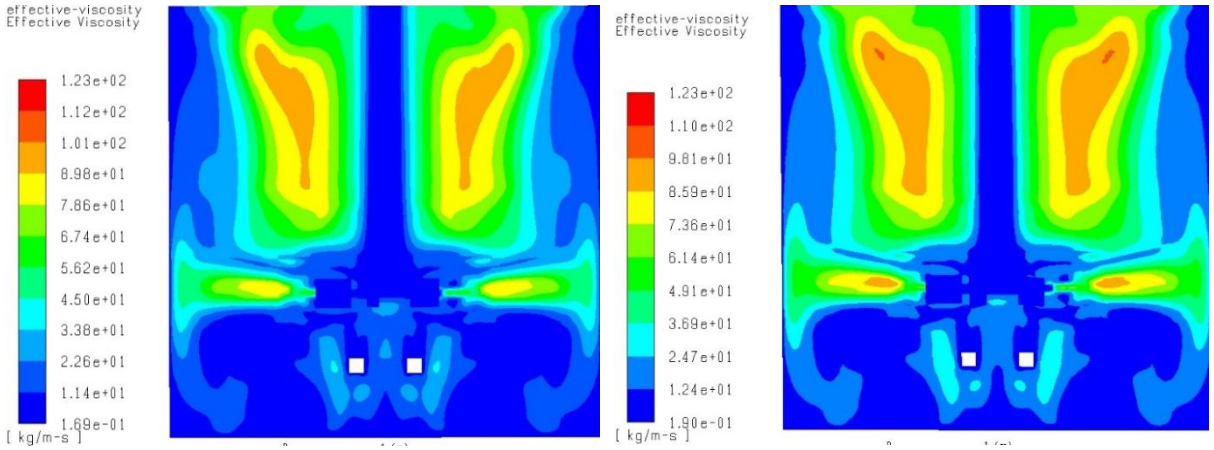


**Figure 6.12** Contour of effective viscosity distribution in the tank V= 50 m$^3$, T=4 m. On the left: standard Ansys Fluent method; on the right: UDF method.

“Figure 6.12” shows the comparison between the contour of the *effective viscosity* $\mu_{eff}$ calculated with the standard Ansys Fluent method (on the left) and using the UDF to compute the viscosity (on the right). *Effective viscosity* is defined as the sum of the molecular viscosity and the turbulent viscosity, as reported in eq (6.2):

$$\mu_{eff} = \mu_{mol} + \mu_T \tag{6.2}$$

Both contours look almost equal, showing no particular differences between the two methods. A further comparison between *molecular viscosity* and *effective viscosity* (“Figure 6.13”) shows how the $\mu_{mol}$ is approximately two order of magnitude smaller than the overall $\mu_{eff}$, thus meaning $\mu_T$ is far greater than molecular one, at least not at these high-power dissipating operating conditions, thus not influencing the overall mixing.

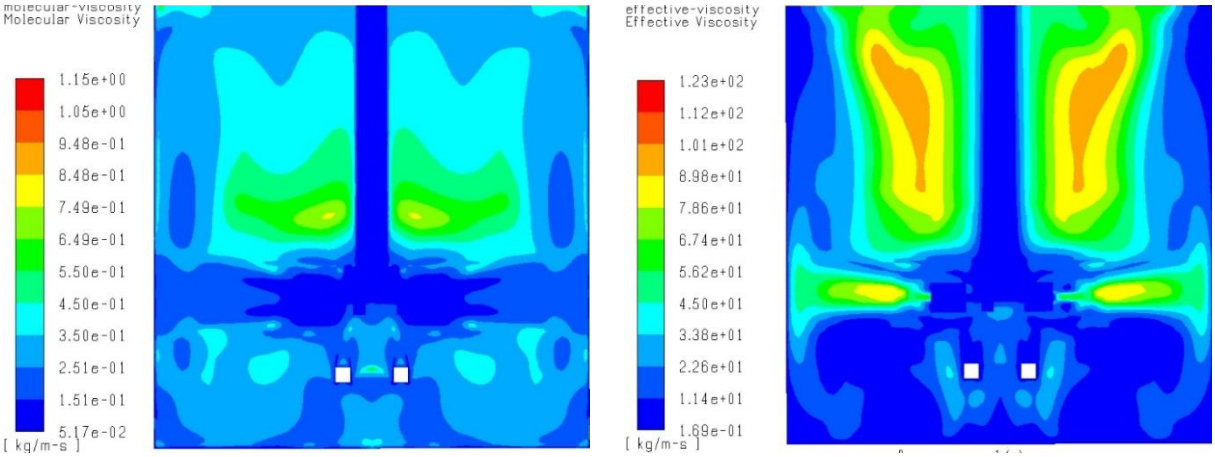


**Figure 6.13** Contour of effective viscosity distribution compared to the molecular distribution, both with standard Ansys Fluent method. Tank V= 50 m$^3$, T=4 m. On the left: *molecular viscosity* $\mu_{mol}$; on the right: *effective viscosity* $\mu_{eff}$.

Further investigation should be carried out to investigate the effect that local turbulence, in shear-thinning fluids, have on the shape and dimensions of the gas bubbles.

## 6.3 Multiphase tracking simulations

Multiphase simulations were performed with Euler-Euler multiphase model, with water as primary phase and air as secondary, with a bubble constant diameter $d_b$= 0.003m. Unfortunately, the results achieved can be describe more in qualitative way because it took almost all the time dedicated to the subject to find a good set-up to have reliable prediction of the system.

The turbulent model initially selected was *Realizable k-ε* with "*Dispersed"* option enabled, in order to take into account, the not negligible difference between phases density. The interphase interactions enabled were, initially, (see "Section 4.4.3"), *drag law* and *surface tension* ($\sigma$= 0.073 Nm), to be specified with Grace and Tomiyama models. The *drag law* chosen was Grace (see "Section 4.4.1"). The air inlet was set as a *velocity inlet* and thus it required to specify the gas velocity. The experimental flow-rate $Q_g$= 1 Nm$^3$/h was divided by the sparger top surface $A_{sparger}$, to obtain the velocity. The gas fraction at the inlet $\alpha_{g,IN}$ was set very low, around 0.2 in order to improve the stability of the simulations. The definitive velocity setting follows Eq. (6.3):

$$v_{g,sparger} = \frac{Q_g}{A_{sparger} \cdot \alpha_{g,IN}} \tag{6.2}$$

The top surface condition used was *degassing* at a height equal to 0.3 m from the bottom of the tank.

At first, single phase solved flow field, with water was used as initial condition for the simulations. The tank initially used was the $T_{30}$, with three values of impeller speed: $N$= 400, 800 and 1000 rpm. These speeds were chosen to be sure to solve a well dispersed system, according to experimental results,

Using a steady-state mode, the simulations diverged almost immediately. It was not clear if the divergence was due to the steady-state mode, *degassing* boundary condition or the interpolation of the flow field from previous simulations.

The second set-up chosen was a transient mode, with the same parameter and settings as the previous one, but it diverged quickly as well. Thus, no interpolation with previously solved flow field was used further on.

The transient simulations were performed starting with a time-step of $1 \cdot 10^{-6}$ s and then gradually increased, up to $1 \cdot 10^{-3}$, as soon as the system showed to be stable. *Normalized residuals* were set at $1 \cdot 10^{-3}$ with *first order upwind* differencing scheme. On average, with around 72 hr of simulations in the cluster, described in "Sections 5", the elapsed *physical time* simulated was around 6 s. Iterations per time step were set at 50. Every change in time-step resulted great instabilities and loss in accuracy, with normalized residuals at the end of the simulations ranging around $1 \cdot 10^{-2}$.

The results obtained were very unreliable, with gas *holdup* less than 1%, with an expected value of 2.7%, and *power number* of less than half of the expected value, ranging 0.9-1.5. Normally, multiphase gas-liquid stirred tank system have a $N_{P,gas}$ between 0.5 – 0.8 with respect to the single-phase system.

A third set-up was implemented, changing the top surface condition. In addition, Tomiyama *drag law* (see "Section 4.4.1"), being previously validated at IFPEN for bubble columns, was chosen and *virtual mass* disabled, a parameter known for adding instabilities to the system. The top surface was modified, adding a gas volume at the top, a very common condition when simulating bubble columns.

The geometry of the tank was modified, adding the additional volume, increasing dimension of around 0.1 m of the wall height. This additional volume was meshed coarsely with respect to the rest of the system, in order to minimize the computational burden to the simulation. The new domain was imposed as air, by defining the additional volume with a secondary phase fraction $\alpha_{g,IN} = 1$. The same setting and procedure for time-step size, iterations and differencing schemes were used.

Again, results for this system were very unreliable and similar to those previously obtained. In particular air appeared to remain inside the tank, forming large cavities behind impeller blades and around the shaft. Moreover, non-physical gas distribution formed above and below the impeller, without normal coalescence towards the upper surface, as expected. The predicted gas *holdup* was far below expected value, around 0.7 to 1%, and similarly the *power number* was too small, compared to the expected one.

"Figure 6.14a" shows the contour of the distribution of gas volume fraction $\alpha_g$ throughout the tank, the white arrows represent the water velocity magnitude flow field. The interphase contact layer at the top of the vessel is reasonably well predicted, for the shape of the interface follow the expected parabolic shape. The gas distribution above and below the impeller are non-physical features, because air should coalesce towards the upper boundary layer, not remain entrapped inside the tank. A similar analysis could be done for the gas around the shaft. Instead, the air cavities behind the impeller blades to some extent are expected, because of the inherent local depression common to this type of impeller (see "Section 3.2"). Nevertheless, the size of these is too large to be regarded as normal and it seems to the reason behind the very low power number predicted by the simulation. In fact, the impeller results almost completely surrounded, shown in detail in "Figure 6.14b", by gas, thus decreasing sensibly the power provided to the whole system and consequently dissipated.

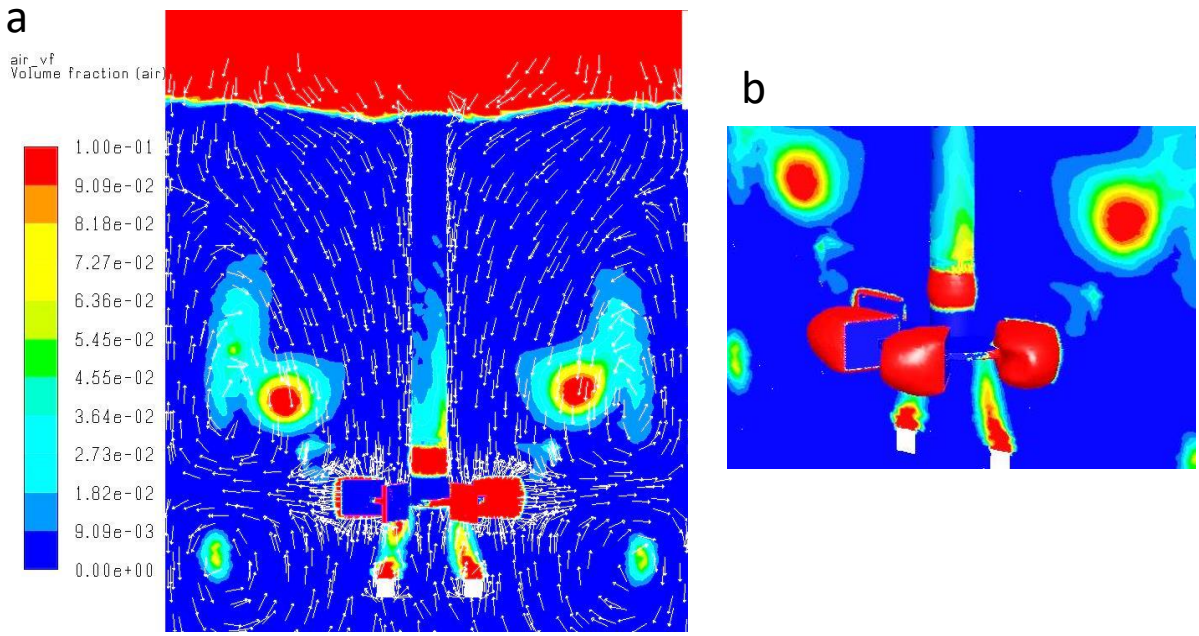


**Figure 6.14** a) Contour of air volume fraction inside the $T_{30}$ tank at $N$= 1000 rpm, with the air pocket at the top surface. White arrows represent the water velocity magnitude field. b) A detailed view of the impeller area surrounded by large gas cavities.

The reasons of this phenomenon can be attributed especially to the turbulent multiphase model, the drag law and in a minor extent to the size of the MRF. As reported by (Buffo and Marchisio 2014)) in their review, the turbulence has a great influence on the shape, size of the bubble and distribution of the gas. It may be possible that the centrifugal forces of the system are too weak to overcome the attraction due to the low-pressure zone in the impeller zone, thus preventing the water to escape. It is also possible that the MRF area is too large, thus exerting centripetal forces to far from the impeller zone, with analogous consequences as previously reported.

Furthermore, it has to be noted that the computational mesh has a huge influence on the calculation and the solution, heavily affecting the stability of the simulation.

Finally, a fourth set-up was found to give reliable prediction in terms of gas holdup. The system was simulated using *Standard k-ε* turbulent model, with Euler-Euler *dispersed* multiphase model, Grace drag law and adding the Brucato coefficient for turbulent system (see "Section 4.4.1" ). The MRF area was slightly reduced in size. The simulation was run first in steady-state, to establish the primary phase flow field and then transient mode to improve solution, using an adaptative time-step increase, starting from $1 \cdot 10^{-6}$ s to 0.02 s, with 40 iteration/time-step. The gas flow-rate was increased gradually during the simulation, starting from a very low one to the standard $Q_g$= 1 $Nm^3/h$. The mesh of the top surface of the sparger was refined, using cell with characteristic dimension equal to 0.001 m. The upper surface is set with degassing boundary condition. These changes improved sensibly the solution of the system, both in stability and in accuracy.

The system shown in "Figure 6.15" is the $T_{60}$ tank, with a superficial velocity of the gas $U_G$= 4 mm/s, equivalent to $Q_g$= 1 $Nm^3/h$, and $N$= 250 rpm, inside the dispersed regime

($Fl_G$= 0.03 > $Fl_{G,CD}$= 0.007). “Table 6.1” summarizes the results of the simulation in comparison with the experimental ones.

**Table 6.1** Results CFD for multiphase system and comparison with experimental results. $T$=0.6 m, $U_G$= 4 mm/s, $N$= 250 rpm.

| | $\alpha_G$ (-) | $P_G/P_0$ |
|---|---|---|
| **Exp.** | 2.7% | 0.676 |
| **CFD** | 2.4% | 0.684 |

The gas distribution is more uniform and physically correct, with air flowing upward, as expected, and without an excessive concentration of the gas around the impeller area. Good results are also obtained in term or $P_G/P_0$, namely the ratio between power dissipated in the multiphase system and that of the unaerated system, with a relative error around 10%.

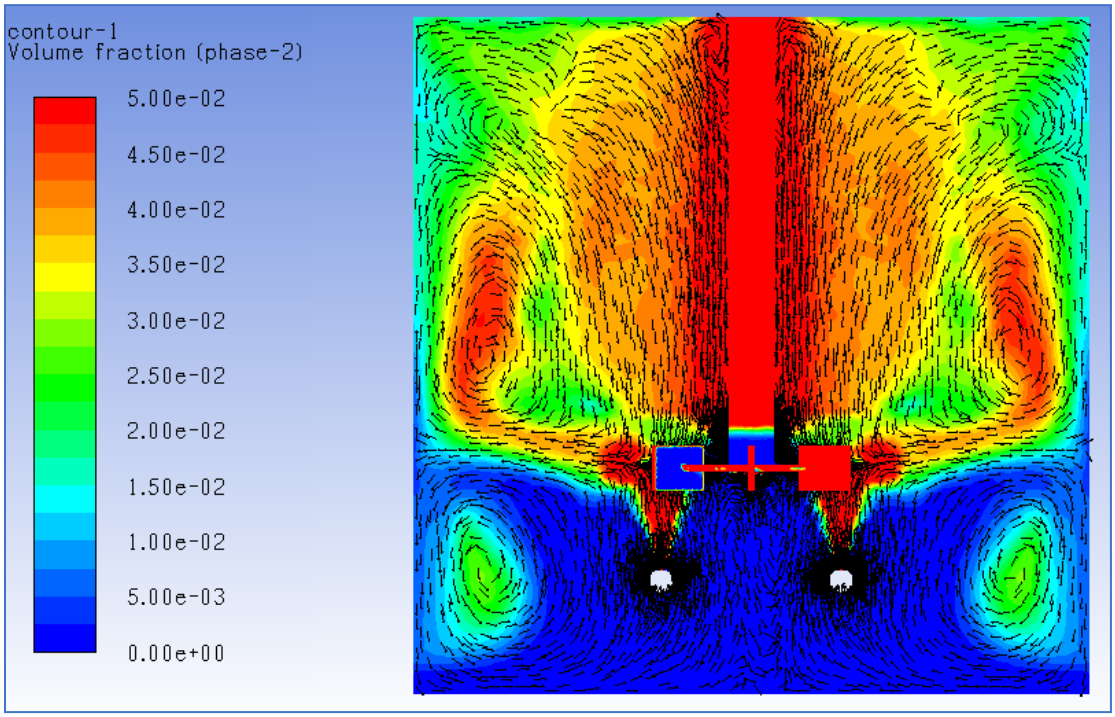


**Figure 6.15** Liquid velocity vectors and gas fraction distribution inside the tank $T_{60}$ (D=0.2 m). $N$ = 250 rpm, $U_G$ = 4 mm/s.

The use of second order upwind differencing scheme, though, created heavy numerical instabilities, thus making still impractical to achieve good prediction of the turbulent dissipation rate $\varepsilon$, with values of $N_P$ of about a half of the expected value.

## 6.4 Fed-batch and particle tracking simulations

Fed-batch simulations were carried out using both the structured hexahedral mesh and the tetrahedral one, scaling dimension of the tank from the T= 0.6 m up to T= 4 m, setting velocities in order to obtain the same power dissipated into the system, $P_0/V$ = 2.7 kW/m$^3$. The fluids simulated were Water, CMC 0.5% and XG 0.5%. First, the flow field was solved, using steady-state formulation, with pseudo-transient option enabled, *Realizable k-ε* turbulent model. The substrate inlet and the kinetics of sugar consumption follow the method illustrated in "Section 5.5.1". The substrate flowrate was calculated using parameters investigated at IFPEN.

The concentration of microorganism equal to $X$= 10 – 20 kg/m$^3$, a concentration of sugar in the inlet flow equal to 500 kg/m$^3$ and the flowrate of sugar equal to $q_{s,IN}$ = 0.03 kg *sugar*/kg *biomass*/hr. For the $T_{60}$ tank (V= 0.168 m$^3$) the volume flowrate of sugar solution at the inlet is, then, equal to $Q_{sugar}$=5.61·10$^{-8}$ m$^3$/s. It can be noted that the inlet flowrate is negligible compared to the total volume of the system, thus it can not cause any perturbation to the flow field. Being the process intrinsically transient, it was necessary to solve numerically the Eq. (5.17) in order to know the order of magnitude of the time the process requires to reach the steady-state. This was done with a simple calculation with Microsoft Excel. Discretizing the equation with a simple finite difference method and imposing a time step *dt*, the value of substrate concentration *S* and the time elapsed was determined. "Figure 6.16" shows the plot of the solution of the equation for three different concentration of biomass, referred to the $T_{60}$ tank.

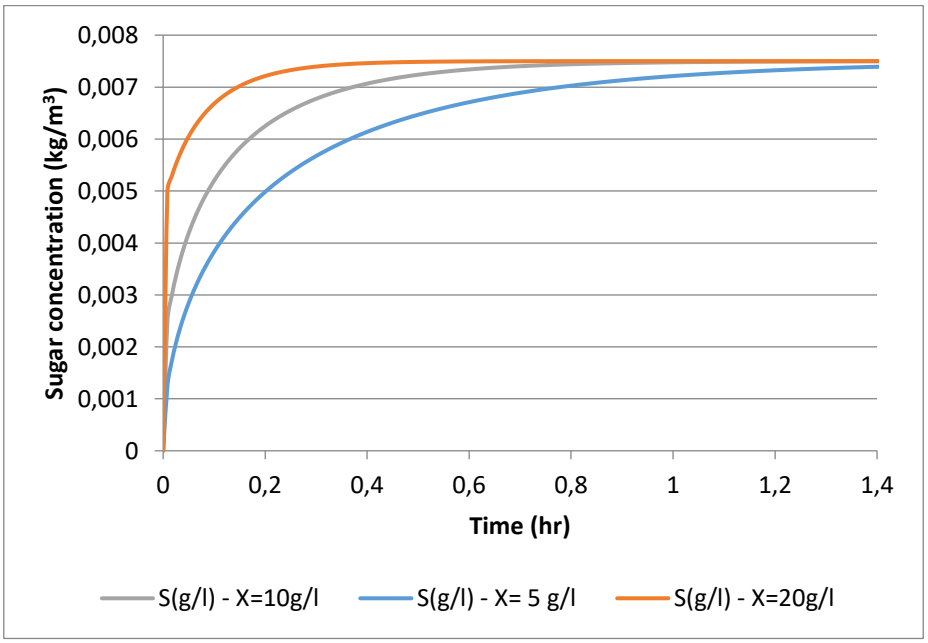


**Figure 6.16** Solution of eq (5.17) for three different concentration of biomass.

The time constant of the depletion process is of the order of magnitude of half an hour, thus way bigger than the mixing time of the tank, which is of the order of magnitude of seconds. Thus, it can be supposed that the rich area would be very small compared to the total volume.

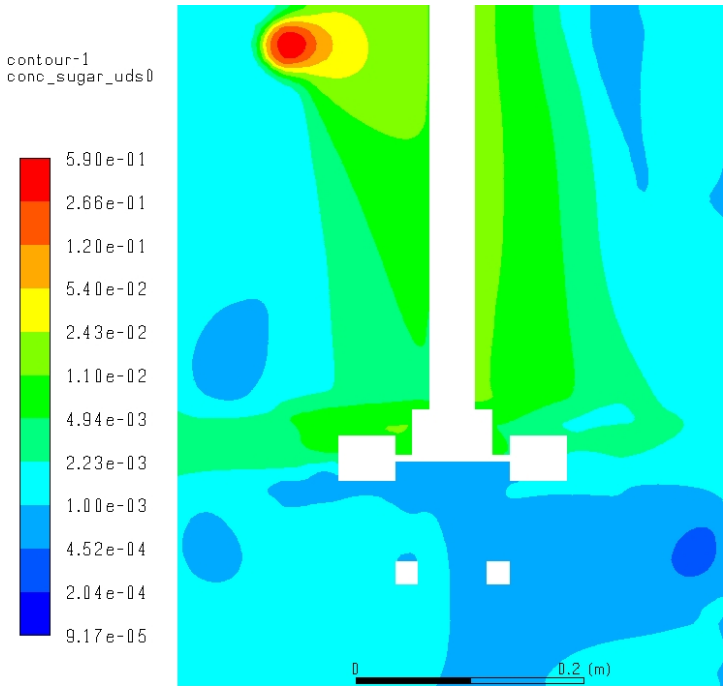


**Figure 6.17** Contour of the substrate distribution throughout the vessel in water, T= 0.6m, N= 35 rpm.

"Figure 6.17" shows the contour of the sugar concentration in the vessel, with water as fluid. The average concentration of sugar is $2.5 \cdot 10^{-3}$ kg/m$^3$, but the distribution is quite diverse throughout the tank, with the lower part and the side having smaller concentration, whereas in proximity of the inlet and around the impeller, results lower. The contour confirms the classic pattern of Rushton impeller mixing, shown in "Figure 3.3", with the lower part being almost isolated from the main upper side loop, as well as the main loop being concentrated around the shaft, with the area near the wall being more stagnant.

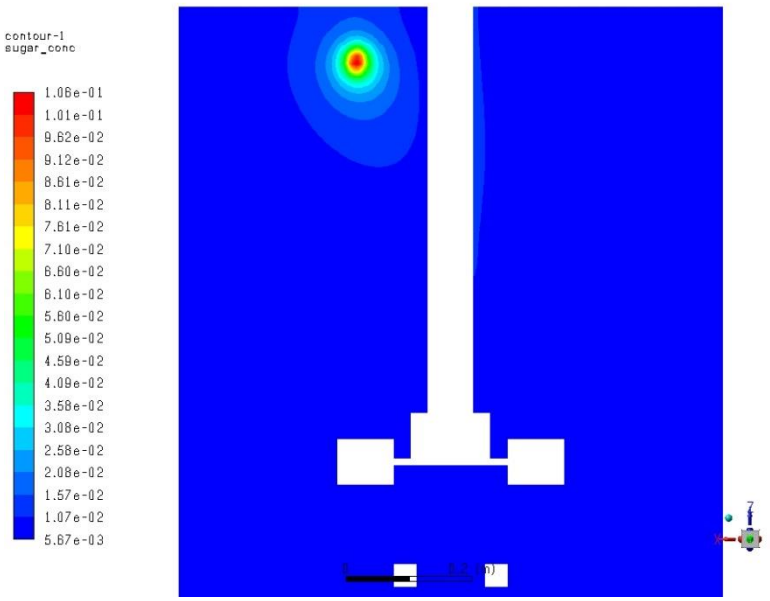


**Figure 6.18** Contour of the substrate distribution in CMC 0.5%, T= 1 m, N= 290 rpm.

"Figure 6.18" shows the contour of sugar concentration for the 1 $m^3$ tank, at N= 290 rpm ($P_0/V$ = 2.7 $kW/m^3$). The pattern of the distribution is similar, with a small area with larger concentration and the rest of the tank with concentration around that of equilibrium. The mixing time is so small compared to the dynamic of depletion that microorganism has the time to consume most of the excess of substrate, thus entering in "poor" sugar area, where the enzyme is produced.

The *Probability Density Function* (PDF) of sugar, shown in "Figure 6.19", relative to the $T_{60}$ tank with water (see "Figure 6.18"), can be compared to a *log-normal* distribution, with most of the volume at very low concentration, namely the *production* and *starvation* areas and a very small *rich* area close to the inlet of the fed-batch.

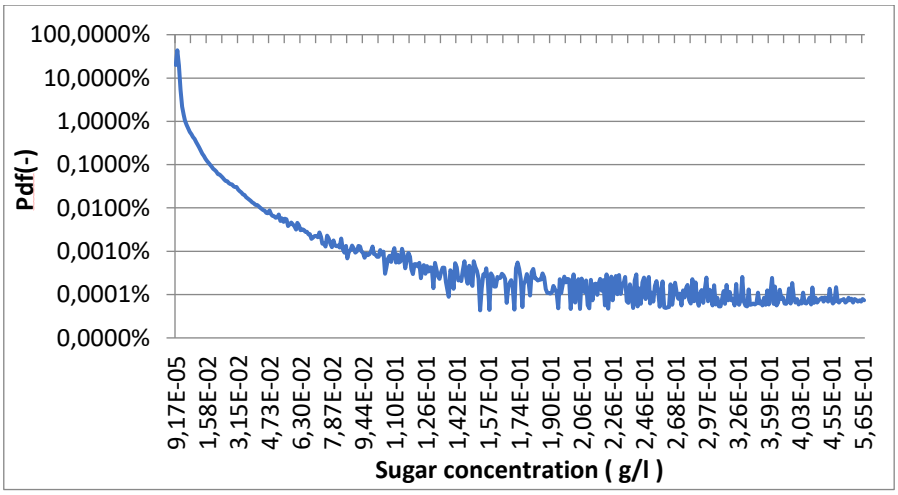


**Figure 6.19** Probability density function of the sugar distribution inside the tank.

The last part needed to validate the tracking methodology, the one involving the discrete particle simulation, was only outlined. For reason of simplification, no division between *excess*, *limitation* and *starvation* was carried out, but a simple cylindrical surface at the same level as the impeller was considered as sampling area. 40000 *massless* particles in *free random walk* were simulated.

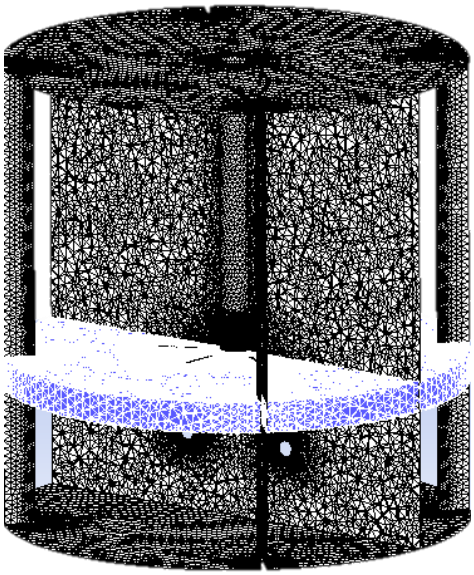

**Figure 6.20** Sampling are used to track the particles frequency of passage

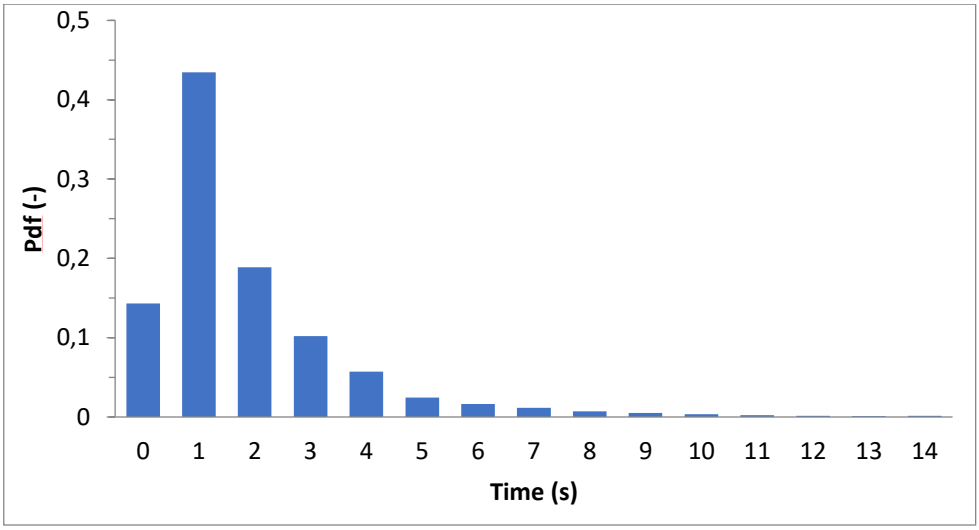


**Figure 6.21** Frequency of passage through the sampling area distribution PDF for 40000 particles

The area is shown “Figure 6.20”, whereas the results of the discrete particle trajectories are summarized in “Figure 6.21”. A *frequency of passage* distribution, a PDF, was made, taking account of the percentage of particles that had crossed the sampling area for a certain period of time. Again, the PDF shows a similarity with a log-normal distribution, with most of the particle, and thus the microorganism, spending no more than few seconds in the sampling area, thus in a potential area with excess of substrate.

# 7 Conclusions

In this work, single-phase and multiphase CFD simulations on a stirred tank bioreactor were performed using the commercial code Ansys Fluent 18.2. Numerical results were compared to experimental data, acquired for different tank diameter sizes (0.3 m, 0.6 m) and with different impeller configurations, or correlation found in literature.

The objective of the study was to find the best CFD model to describe the hydrodynamics and the mixing of the system, at increasing reactor sizes, and to reliably predict the heterogeneities occurring during operations, with a reasonable computational time.

At the beginning, the hydrodynamics was validated by simulating a simple single-phase water system, with a single impeller "square" section tank, in the fully turbulent regime. Two-equations *k-ε* turbulent models were chosen among those present in Ansys Fluent 17.2, *Standard* and *Realizable k-ε,* and compared to find the most reliable. In "Section 5.1" and "Section 5.2" the computational grids used in the work and the methods and set-ups for simulations were presented. "Section 6.1" describe the results obtained, showing that both models can well predict both *power number* and *mixing time*, global hydrodynamics parameters related respectively to power dissipation and homogeneity in the tank. *Realizable k-ε* has shown to be the model giving results which are in good agreement with the experimental data. The reason relies on the fact that this model has physical constraints that best apply to swirling flows, although slightly more computational burdening.

The real fermentation broth has a non-Newtonian shear thinning behaviour; thus, simulations were performed using Carboxymethyl Cellulose (0.5% w/w) and Xanthan Gum (0.25% and 0.5% w/w) as model fluids. For this work, the *power law* model was chosen, and the parameters *K* and *n* used were obtained from experimental data, which were available only for an industrial double impeller configuration tank. "Section 5.4.1" describe how software Ansys Fluent 18.2 allows to modify the rheology, according to the model of choice, calculating the shear rate from the mean velocities of the turbulent flow. In "Section 5.4.2" an alternative calculation method, based on the local value of the *turbulent dissipation rate* was applied to investigate the influence of the local turbulence on the rheology. The results presented in "Section 6.2" show how the default method is able to predict in good agreement with experimental data the power dissipation of the system, whereas mixing time results underestimated when the system is not in fully turbulent regime. This is consistent with the fact that by using *k-ε* models, the hypothesis of fully turbulent system is made, whereas with shear-thinning fluids many areas in the tank are stagnant, so characterized by a transitional or even laminar Re. Modification of the molecular viscosity, instead, has shown that in such turbulent systems, the influence of the local turbulence on the rheology is negligible, but it could be of some importance in characterizing multiphase systems.

In "Section 5.2.3" set-up and method for the multiphase system were presented. Euler-Euler model was applied, and several simulations were performed with different turbulent models and boundary conditions in order to find the best set-up in terms of time of calculation and stability of the solution. Results, presented in "Section 6.3", shows the importance of the choice of the drag law model and the addition of Brucato modification coefficient in order to obtain a stable simulation and good solution, in terms of gas hold-up and power dissipated. Instead, the use of first order differencing scheme, for reason of stability of the solution, has prevented to obtain accurate values of power number and energy dissipation. Moreover, it is shown how the

outlet boundary condition, the size of the MRF zone, the flow rate of the gas and the mesh can deeply influence the outcome of multiphase simulations. Thus, all this aspect should be analysed thoroughly in simulating a gas-liquid multiphase system.

Finally, fed-batch mode fermentation was simulated to analyse the distribution of the substrate inside the vessel and a method to track the trajectories of microorganism inside such a system was investigated. In “Section 5.6” the methodology to implement the sugar depletion kinetics and to simulated discrete particles with Lagrangian-Euler approach was described. Results of “Section 6.3” show how the rheology and the impeller speed influence the substrate distribution, creating rich and poor areas of sugar in the vessel. Moreover, discrete particles Lagrangian-Euler simulations resulted a viable method to investigate the frequency of passage of microorganism through different sugar concentration zones. Thus, CFD simulation can be useful to gather information to be used in subsequent *scale-down* studies in order to investigate the effect of scarcity and excess of substrate on the yield of the process.

Further investigations of the system with CFD simulations should concentrate on the multiphase system, specifically: using second order differencing scheme to improve accuracy of the solution, to investigate the influence of higher gas flow rates, with superficial velocity $U_G$ ranging 8 – 15 mm/s, which corresponds to common industrial set-up, to assess the effect of complex rheology on the drag coefficient $C_D$ and, therefore, on bubble shape and size distribution and finally to consider the influence of turbulence and shear-thinning behaviour on gas hold-up and mass transfer.

Finally, a thorough analysis should be carried on with discrete particles tracking regarding the distribution of frequency of passage and residence time of microorganism, in starvation and excess areas to generate data for scale-down studies.

# List of figures

# List of tables

# Notations

| | | |
|---|---|---|
| $a$ | Specific interfacial area | $m^2/m^3$ |
| $C_{A,i}$ | Concentration in the liquid at the interface | $mol/m^3$ |
| $C_A$ | Concentration in the liquid | $mol/m^3$ |
| $C_A^*$ | Equilibrium concentration | $mol/m^3$ |
| $d_{ij}$ | Viscous stress tensor | $kg/m.s^2$ |
| $D$ | Impeller diameter | m |
| $d_{32}$ | Sauter mean diameter | m |
| $d_b$ | Bubble diameter | m |
| $D_L$ | Molecular diffusion coefficient | $m^2/s$ |
| $Fl_G$ | Gas flow number | (-) |
| $Fr$ | Impeller Froude number | (-) |
| $g$ | Gravitational acceleration | $m/s^2$ |
| $H$ | Liquid height in the tank | m |
| $H_A$ | Henry constant | $mol/(m^3\ Pa)$ |
| $J_{A,G}$ | Mass flux in the gas phase | $mol/s.m^2$ |
| $J_{A,L}$ | Mass flux in the liquid phase | $mol/s.m^2$ |
| $K_{S,\mu}$ | Half-velocity constant referred to biomass growth | $kg/m^3$ |
| $K_{S,p}$ | Half-velocity constant referred to enzyme production | $kg/m^3$ |
| $K$ | Consistency index | $(kg/m.s)\ s^n$ |
| $k_G$ | Mass transfer coefficient in the gas phase | m/s |
| $k_L$ | Mass transfer coefficient in the liquid phase | m/s |
| $K_L$ | Global mass transfer coefficient | m/s |
| $k_s$ | Metzner-Otto constant | (-) |
| $n$ | Flow behavior index | (-) |
| $N$ | Impeller rotation speed | $s^{-1}$ |
| $N_P$ | Impeller power number | (-) |
| $P$ | Power | $kg.m^2/\ s^3$ |
| $P_G$ | Power draw in aerated conditions | $kg.m^2/\ s^3$ |
| $p_{A,i}$ | Partial pressure at the gas-liquid interface | Pa |
| $p_A$ | Partial pressure | Pa |

| | | |
|---|---|---|
| $q_P$ | Enzyme production | kg/kg.s |
| $q_{p_{min}}$ | Minimum enzyme production | kg/kg.s |
| $q_{p_{max}}$ | Maximum enzyme production | kg/kg.s |
| $q_S$ | Consumption of substrate | kg/kg.s |
| $Q_G$ | Gas flow rate | $m^3/s$ |
| $Re$ | Reynolds number | (-) |
| $S$ | Substrate concentration | $kg/m^3$ |
| $S_{crit}$ | Critical substrate concentration | $kg/m^3$ |
| $S_{ij}$ | Strain-rate tensor | $s^{-1}$ |
| $T$ | Diameter of the tank | m |
| $U_i$ | Local velocity vector component *i* | m/s |
| $u_{slip}$ | Relative slip velocity | m/s |
| $X$ | Biomass concentration | $kg/m^3$ |
| $Y_{X,S}$ | Substrate conversion efficiency in biomass | kg/kg |
| $Y_{P,S}$ | Substrate conversion efficiency in product | kg/kg |
| $y$ | Metabolism split function | (-) |

Greek letters :

| | | |
|---|---|---|
| $\dot{\gamma}$ | Shear rate | $s^{-1}$ |
| $\Gamma$ | Torque | $kg.m^2/ s^2$ |
| $\varepsilon$ | Turbulent energy dissipation rate | $m^2/s^3$ |
| $\mu$ | Growth rate | $s^{-1}$ |
| $\mu_{max}$ | Mximum growth rate | $s^{-1}$ |
| $\mu_L$ | Viscosity of the liquid | kg/m.s |
| $\mu_a$ | Apparent viscosity | kg/m.s |
| $\nu$ | Kinematic viscosity | $m^2/s$ |
| $\rho$ | Density | $kg/m^3$ |
| σ | Interfacial tension | N/m |
| $\tau$ | Shear stress | $kg/m.s^2$ |

# Bibliography


Ameur H., Bouzit M., 2012, Mixing in shear thinning fluids. In *Braz. J. Chem. Eng.* **29** (2), pp. 349–358. [DOI: 10.1590/S0104-66322012000200015]

Andersson B., Andersson R., Håkasson L., Mortensen M., Sudiyo Ra. van Wachem B., 2012, Computational Fluid Dynamics for Engineers. Cambridge University Press, Cambridge, UK.

ANSYS Inc., 2013. *ANSYS Fluent theory guide.* 15th ed. s.l.:SAS IP, Inc..

Azadi P., Malina R., Barrett S. R.H., Kraft M., 2017, The evolution of the biofuel science. In *Renewable and Sustainable Energy Reviews* **76**, pp. 1479–1484. [DOI: 10.1016/j.rser.2016.11.181]

Bach C., Yang J., Larsson H., Stocks S. M., Gernaey K. V., Albaek M. O., Krühne U., 2017, Evaluation of mixing and mass transfer in a stirred pilot scale bioreactor utilizing CFD. In *Chemical Engineering Science* **171**, pp. 19–26. [DOI: 10.1016/j.ces.2017.05.001]

Bird R. B., Stewart W. E., Lightfoot E. N., 2002, Transport Phenomena. Second Edition. John Wiley & Sons, Incorporated New York, USA.

Bouaifi M. and Roustan M., 2001, Power consumption, mixing time and homogenisation energy in dual-impeller agitated gas–liquid reactors. In *Chemical Engineering and Processing: Process Intensification* **40** (2), pp. 87–95. [DOI: 10.1016/S0255-2701(00)00128-8]

Brandt A., Gräsvik J., Hallett J. P., Welton T., 2013, Deconstruction of lignocellulosic biomass with ionic liquids. In *Green Chem.* **15** (3), p. 550. [DOI: 10.1039/c2gc36364j]

Brucato A., Grisafi, F., Montante G., 1998, Particle drag coefficients in turbulent fluids. In *Chemical Engineering Science* **53** (18), pp. 3295–3314. [DOI: 10.1016/S0009-2509(98)00114-6]

Buffo A., Marchisio D. L., 2014, Modeling and simulation of turbulent polydisperse gas-liquid systems via the generalized population balance equation. In *Reviews in Chemical Engineering* **30** (1). [DOI: 10.1515/revce-2013-0015]

Combest D. P., Ramachandran P. A., Dudukovic M. P., 2011, On the Gradient Diffusion Hypothesis and Passive Scalar Transport in Turbulent Flows. In *Ind. Eng. Chem. Res.* **50** (15), pp. 8817–8823. [DOI: 10.1021/ie200055s]

Clift R., Grace J. R., Weber M. E., 1978, Bubbles, drops, and particles. Academic Press, New York, London.

Edwards M. F., Baker M. R., Godfrey J. C., 1992, Mixing of liquids in stirred tanks. In *Mixing in the Process Industries*( Harby N., Edwards M. F., Nienow A. W., Eds.), Elsevier Ltd., Amsterdam, NLD, pp. 137–158. [ISBN978-0-7506-3760-2]

Gabelle J.-C., 2012, Analyse locale et globale de l'hydrodynamique et du transfert de matière dans des fluides à rhéologie complexe caractéristiques des milieux de fermentation. Ph.D Thesis. IFPEN - Institute Français du Petrol Energie Nouvelle; INSA - I, Lyon, France.

Gabelle J.-C., Augier F., Carvalho A., Rousset R., Morchain J., 2011, Effect of tank size on kLa and mixing time in aerated stirred reactors with non-Newtonian fluids. In *Can. J. Chem. Eng.* **89** (5), pp. 1139–1153. [DOI: 10.1002/cjce.20571]

Gori F. and Boghi A, 2011, Two new differential equations of turbulent dissipation rate and apparent viscosity for non-newtonian fluids. In *International Communications in Heat and Mass Transfer* **38** (6), pp. 696–703.[DOI: 10.1016/j.icheatmasstransfer.2011.03.003]

Gori F. and Boghi A, 2012, A three-dimensional exact equation for the turbulent dissipation rate of Generalised Newtonian Fluids. In *International Communications in Heat and Mass Transfer* **39** (4), pp. 477–485. DOI: 10.1016/j.icheatmasstransfer.2012.02.010.

Gradov D.V., Laari A., Turunen I., Koiranen T., 2017, Experimentally Validated CFD Model for Gas-Liquid Flow in a Round-Bottom Stirred Tank Equipped with Rushton Turbine. In *International Journal of Chemical Reactor Engineering* **15** (2), p. 171. [DOI: 10.1515/ijcre-2015-0215]

Grenville R. K., Mak A. T. C., Ruszkowski S. W., 1992, Blending of fluids in mixing tanks by re-circulating turbulent jets. In *Proceeding 1992 Institution of Chemical Engineers Research Events*, pp. 128–130.

Gusakov A. V., 2011, Alternatives to Trichoderma reesei in biofuel production. In *Trends in biotechnology* **29** (9), pp. 419–425. [DOI: 10.1016/j.tibtech.2011.04.004]

Hardy N., Henaut I., Augier F., Béal C., Ben Chaabane F., 2015, Rhéologie des champignons filamenteux. un outil pour la compréhension d'un procédé de production de biocatalyseurs utilisés pour la production de bioéthanol. In *Rhéologie* (**27**), pp. 43–48.

Hardy N., 2016, Identification des critères d'extrapolation du procédé de production de cellulases par Trichoderma reesei en utilisant l'approche `` scale-down ". In *Biotechnologies*. Université Paris-Saclay.

Haringa C., Deshmukh A. T., Mudde R. F., Noorman H. J., 2017, Euler-Lagrange analysis towards representative down-scaling of a 22 m 3 aerobic S. cerevisiae fermentation. In *Chemical Engineering Science* **170**, pp. 653–669. [DOI: 10.1016/j.ces.2017.01.014]

Haringa C., Tang W., Deshmukh A. T., Xia J., Reuss M., Heijnen J. J. et al., 2016, Euler-Lagrange computational fluid dynamics for (bio)reactor scale down: An analysis of organism lifelines. In *Engineering in life sciences* **16** (7), pp. 652–663. [DOI: 10.1002/elsc.201600061]

Jahoda M., Tomášková L., Moštěk M., 2009, CFD prediction of liquid homogenisation in a gas–liquid stirred tank. In *Chemical Engineering Research and Design* **87** (4), pp. 460–467. [DOI: 10.1016/j.cherd.2008.12.006]

Joshi G., Pandey J. K., Rana S., Rawat D. S., 2017, Challenges and opportunities for the application of biofuel. In *Renewable and Sustainable Energy Reviews* **79**, pp. 850–866. [DOI: 10.1016/j.rser.2017.05.185]

Karimi M., Akdogan G., Dellimore K. H., Bradshaw S. M., 2012, Comparison of different drag coefficient correlations in the CFD modelling of a laboratory-scale Rushton-turbine flotation tank. In *Ninth international conference on CFD in the mineral and process industry*, 10-12 December 2012, CSIRO, Melbourne, Australia.

Keating M., 2011, Accelerating CFD solutions. In *ANSYS Advantage* **V** (1), pp. 48 – 49.

Kennes C., Veiga M. C., Eds., 2013, Air Pollution Prevention and Control. In *Bioreactors and Bioenergy*, 1st ed., John Wiley & Sons, Incorporated, New York, USA.

Khapre A., Munshi B., 2014, Numerical Comparison of Rushton Turbine and CD-6 Impeller in Non-Newtonian Fluid Stirred Tank. In *International Journal of Chemical and Molecular Engineering Nuclear, Materials and Metallurgical Engineering* **8** (11). World Academy of Science, Engineering and Technology 1231-1232.

Lapin A., Müller D., Reuss M., 2004, Dynamic Behavior of Microbial Populations in Stirred Bioreactors Simulated with Euler−Lagrange Methods: Traveling along the Lifelines of Single Cells †. In *Ind. Eng. Chem. Res.* **43** (16), pp. 4647–4656. [DOI: 10.1021/ie030786k]

Lapin A., Schmid J., Reuss M., 2006, Modelling the dynamics of E. coli populations in the three-dimensional turbulent field of a stirred-tank bioreactor—A structured–segregated approach. In *Chemical Engineering Science* **61** (14), pp. 4783–4797. [DOI: 10.1016/j.ces.2006.03.003]

Lee B. W. and Dudukovic M. P., 2014, Determination of flow regime and gas holdup in gas–liquid stirred tanks. In *Chemical Engineering Science* **109**, pp. 264–275. [DOI: 10.1016/j.ces.2014.01.032]

Luong H. T., Volesky B., 1979, Mechanical power requirements of gas-liquid agitated systems. In *AIChE Journal* **25** (5), pp. 893–895. [DOI: 10.1002/aic.690250520]

Lynd L. R., L. X., Biddy M. J., Allee A., Cai H., Foust T. et al., 2017, Cellulosic ethanol: status and innovation. In *Current opinion in biotechnology* **45**, pp. 202–211. [DOI: 10.1016/j.copbio.2017.03.008]

Marchisio D. and Fox R., 2016, Reacting Flows and the Interaction between Turbulence and Chemistry. In *Reference Module in Chemistry, Molecular Sciences and Chemical Engineering*. Ed. J. Reedijk, Elsevier [DOI: 10.1016/B978-0-12-409547-2.11526-4]

Metzner A. B. and Otto R. E., 1957, Agitation of non-Newtonian fluids. In *AIChE Journal* **9** (4), p. 555. [DOI: 10.1002/aic.690090427]

Nienow A. W., 1998, Hydrodynamics of Stirred Bioreactors. In *Appl. Mech. Rev.* **51** (1), p. 3. [DOI: 10.1115/1.3098990]

Oey R. S., 2005, Gas-liquid flows in a two-fluid formalism. Modelling and validation of closure relations. Doctoral Thesis. Technische Universiteit Delft, Delft, Netherlands. Aerospace Engineering.

Paul E. L., Atiemo-Obeng V. A., Kresta S. M., 2004, Handbook of industrial mixing. Science and practice. Wiley-Interscience, Hoboken N.J, USA.

Petitti M., Nasuti A., Marchisio D. L., Vanni M., Baldi G., Mancini N., Podenzani F., 2010a, Bubble size distribution modelling in stirred gas-liquid reactors with QMOM augmented by a new correction algorithm. In *AIChE Journal* **56** (1), pp. 36–53. [DOI: 10.1002/aic.12003]

Petitti M., Nasuti A., Marchisio D. L., Vanni M., Baldi G., Mancini N., Podenzani F., (2010b): Bubble size distribution modeling in stirred gas-liquid reactors with QMOM augmented by a new correction algorithm. In *AIChE Journal* **56** (1), pp. 36–53. [DOI: 10.1002/aic.12003]

Ranade V. V., 2001, Computational Flow Modeling for Chemical Reactor Engineering. Volume 5, Elsevier Science Publishing Co Inc, San Diego, USA.

Reynolds O., 1895, On the Dynamical Theory of Incompressible Viscous Fluids and the Determination of the Criterion. In *Philosophical Transactions of the Royal Society of London*. A, pp. 123–164.

Sánchez Pérez J. A., Rodríguez Porcel E. M., Casas López J. L., Fernández Sevilla J. M., Chisti Y., 2006, Shear rate in stirred tank and bubble column bioreactors. In *Chemical Engineering Journal* **124** (1-3), pp. 1–5. [DOI: 10.1016/j.cej.2006.07.002]

Shang-Tian Y. (Ed.) (2006): Bioprocessing for Value-Added Products from Renewable Resources. New Technologies and Applications. Chapter 9. Filamentous Fungal Cultures - Process characteristic,products and application. With assistance of Hesham A. El-Enshasy. 1st edition. 1 volume: Elsevier Science.

Tomiyama A., Kataoka I., Zun I., Sakaguchi T., 1998, Drag Coefficients of Single Bubbles under Normal and Micro Gravity Conditions. In *JSME International Journal Series B* **41**(2), pp. 472-479. [DOI: 10.1299/jsmeb.41.472]

Valverde M. R., Bettega R., Badino A. C., 2016, Numerical evaluation of mass transfer coefficient in stirred tank reactors with non-Newtonian fluid. In *Theor. Found. Chem. Eng.* **50** (6), pp. 945–958. [DOI: 10.1134/S0040579516060178]

Venneker B. C. H., Derksen J. J., van den Akker H. E. A., 2010, Turbulent flow of shear-thinning liquids in stirred tanks—The effects of Reynolds number and flow index. In *Chemical Engineering Research and Design* **88** (7), pp. 827–843. [DOI: 10.1016/j.cherd.2010.01.002]

Zhang C., Gu J., Qin H., Xu Q., Li W., Jia X., Zhang J., 2017, CFD analysis of flow pattern and power consumption for viscous fluids in in-line high shear mixers. In *Chemical Engineering Research and Design* **117**, pp. 190–204. [DOI: 10.1016/j.cherd.2016.10.013]

# A. Reynolds averaging rules

Taking into account a general variable Φ(**x**,t):

$$\langle \phi \rangle (\boldsymbol{x}) = \frac{1}{\Delta t} \int_{t}^{t+\Delta t} \phi(\boldsymbol{x}, t')\, dt' \tag{A.1}$$

The operator is expressed with ⟨ ⟩ and applying it to a variable decomposed following Reynold decomposition:

Average of a mean quantity

$$\langle \langle \phi \rangle \rangle = \langle \phi \rangle \tag{A.2}$$

Average of a fluctuating quantity

$$\langle \phi' \rangle = 0 \tag{A.3}$$

Average of a derivative

$$\langle \frac{\partial \phi}{\partial x_i} \rangle = \frac{\partial}{\partial x_i} \langle \phi \rangle \tag{A.4}$$

Average of the product of two fluctuating quantities

$$\begin{cases} \langle \phi' \cdot \psi' \rangle = 0 \ \rightarrow if\ the\ two\ quantities\ are\ uncorrelated \\ \\ \langle \phi' \cdot \psi' \rangle \neq 0 \ \rightarrow if\ the\ two\ quantities\ are\ correlated \end{cases} \tag{A.5}$$

# B. Scalar quantity diffusivity UDF

```
#include "udf.h"
#define sct 0.7;

DEFINE_DIFFUSIVITY(sct07,cell,thread,i)
{
    Thread *thread_l, *thread_g, *tmix;
    real epsg,mutl,rhol,db,A,n,coeff;
    real u_eau,u_air,v_eau,v_air,urx,ury,ur2,ur;
    real d_eff,diff_zero;

    if (NULL == THREAD_SUPER_THREAD(thread)){
    tmix = thread;
    }
    else{
    tmix = THREAD_SUPER_THREAD(thread);
    }
    thread_l=THREAD_SUB_THREAD(tmix, 0);
    thread_g=THREAD_SUB_THREAD(tmix, 1);

    epsg=C_VOF(cell, thread_g);
    rhol=C_R(cell,thread_l);
    mutl=C_MU_T(cell,thread_l);
    db=C_PHASE_DIAMETER(cell,thread_g);
    u_eau=C_U(cell,thread_l);
    u_air=C_U(cell,thread_g);
    v_eau=C_V(cell,thread_l);
    v_air=C_V(cell,thread_g);

    /*vitesse relative*/
    urx=fabs(u_air-u_eau);
    ury=fabs(v_air-v_eau);
    ur2=pow(urx,2)+pow(ury,2);
    ur=pow(ur2,0.5);

    /*constantes*/
    A=20.0;
    n=0.5;
    coeff=A*ur*db*pow(epsg,n);

    diff_zero=1e-8*rhol+mutl/sct;
    d_eff=diff_zero;
    return d_eff;
```

# C. Rheological modification UDF

```
/*****************************************
UDF for specifying a power-law viscosity
*****************************************/

#include "udf.h"

#define n 0.65 /****Rheological indexes for CMC 0.50%****/
#define K 0.44


DEFINE_PROPERTY(pwr_viscosity,c,t)
{
real gamma;
real mu_app;
real rho = C_R(c,t);
real diss = C_D(c,t);

gamma = pow(rho*diss/K,1./(n+1));
mu_app = K*pow(gamma,n-1);

return mu_app;
}
```

# D. Substrate consumption UDF

```
/*********************************************
UDF for specifying a sugar consumption kinetic
*********************************************/
#include "udf.h"

#define S_crit 0.3 /*** critic substrate concentration in g/L ***/
#define A 20
#define mu_max 0.08 /*** ./h ***/
#define k_mu 0.05 /*** g/L ***/
#define qp_max 0.015 /*** ./h ***/
#define qp_min 0.002 /*** ./h ***/
#define k_qp 0.001 /*** g/L ***/
#define Y_xs 0.5 /*** Y_xs and Y_ps are the conversion yields ***/
#define Y_ps 0.5 /*********************************************/
#define X 10 /*** biomass concentration in g/L ***/

DEFINE_SOURCE(sugar_kinetics,c,t,dS,eqn)

{
  real y,dy,mu,dmu,qp,dqp,source;
  real S;
  S = C_R(c,t)*C_UDSI(c,t,0);
  y = tanh((S-S_crit)*A)*0.5+0.5;
dy = 0.5*A*pow(1/cosh((S-S_crit)*A),2); /*** definition of y
                                            function derivate- Ansys
                                            requires it ***/
  mu = mu_max*S*y/(k_mu+S)/3600;
  dmu = mu_max*(y*(1/(k_mu+S)+S*log(k_mu+S))+S/(k_mu+S)*dy)/3600;
  qp = (qp_max*(1-y)+qp_min)*S/(k_qp+S)/3600;
  dqp = S/(k_qp+S)*(-qp_max*dy)+(qp_max*(1-
y)+qp_min)*(1/(k_qp+S)+S*log(k_qp+S))/3600;
  source = -X*(mu/Y_xs+qp/Y_ps);     /*** [kg/m3-s] ***/
  dS[eqn] = -X*(dmu/Y_xs+dqp/Y_ps);  /*** [./s] ***/
  return source;
}
```

# Acknowledgements

Firstly, I would like to thank IFP-Energie Nouvelle for giving me the opportunity of carrying out my work in complete independence and full-reasonability, it was an incredible opportunity of self-growth and maturation and gave me the required confidence to decide to keep working in the R&D fields.

I owe a personal thank to Frédéric Augier, for his support during all the internship and especially during the though *hardware-failure* and *multiphase* times, for his unlimited optimism and his "t'inquiète pas" and finally for trusting in my awful French and thus giving me the opportunity to improving it.

I am particularly grateful for the assistance given by Vincenzo Cappello, for his calmness and patience even in the most stressing moments, for the several laughs in the corridors and for his help in understanding the whole work.

I would also like to thank Cécile Plais, for trusting me from the first instant, for her availability, her support during the whole period and the countless explanation on the telephone.

Finally, I would like to thank professor Daniele Marchisio for his precious suggestion during the writing of this thesis.

I want to express my gratitude to all the "*stagiaires*" present at IFP during my period there for their friendship, support during hard times and laughs. In particular (strictly randomly): to Bruno, my first friend in Lyon, for our good nightly talks and laughs, you're a real Friend; to Elia and Fabrizio and Fabio, the Italian *coffee break crew*, because those moments were the most important ones at work; a particular thank to Tanusha, for her sweetness in every situation and for helping me with French from the beginning; to the Portuguese girls, namely Sofia, Leonor, Ana, Rita, Mariana; I would also like to thank Licia, for the weekends spent studing in my kitchen; to Jano, Luca, Amina, Marko, Charles, Maxime, Kike, and Malika.

I am particularly grateful for the assistance given by Sofia, my *coloc,* for helping me learning French once again, correcting me, teaching me and supporting me during all our period together.

A special thank goes to Giulia (*Rigola*), for turning my internship into the best *Erasmus* experience I could ever have, for teasing me to go out when I was confined to my room, for her smile, her laughs, for all the time at "*les quais*", for have been my personal portable French dictionary, for standing by me during the hard times in writing the thesis and for being more than just a friend. This experience would not have been the same without you.

I would also like to thank Djordje and Andrea for the best nights out and all the Erasmus people I met during my months in Lyon.

Proseguo I miei ringraziamenti in italiano perché questo lavoro di tesi è stato anche il frutto dei miei anni passata all'università e a Torino, pertanto ringrazio quei colleghi che hanno reso certi momenti "politecnici" più allegri: Carlo, Gaia, Homero, Giorgio, Giovanni, Rocco, Davide e Pess.

Un pensiero speciale lo rivolgo a Dario e Letizia, la vostra amicizia è stata fondamentale sia dentro che fuori l'università, grazie mille per tutto il tempo passato assieme.

Ci tengo a ringraziare particolarmente i compagni del collettivo Alter.Polis, perché grazie alle esperienze passate insieme posso ritenermi una persona più consapevole, più umana e solo grazie a voi ho capito veramente cosa significa credere fortemente in qualcosa e dare sé stessi per una causa, nonché dormire su un pallet in una palestra sotto la pioggia. In particolare ringrazio *la vecchia guardia*: Livio, Elia, Erica, Marco, Sara, Giulio, Andrea, Simone, Davide, Junior, Leonardo, Liliana, Francesca, Riccardo, Tommaso.

Un ringraziamento a parte merita Giacomo, che oltre ad essere un compagno è stato anche un vero amico, sempre pronto ad ascoltarmi e a darmi consigli nei momenti più bui di questo percorso universitario.

Meritano un ringraziamento speciale gli amici di una vita, per avermi sopportato e supportato durante questi anni difficili, per essermi rimasti vicino sempre e avermi perdonato tutte le mie *sparizioni* durante gli esami. In particolar modo ringrazio: Matteo, non solo perché hai creato la migliore presentazione che il collegio di ingegneria chimica abbia mai visto, ma per tutti i consigli di questi anni, i giri in montagna, nella neve, su roccia ed in palestra; Filippo, amico di una vita, per il tuo immancabile "ciao Ricky" al telefono, per le birrette ignoranti e il silenzioso supporto; Aurelia, perché più di tutti mi hai ascoltato nei momenti difficili ma anche in quelli più belli; Amedeo, perché mai una volta hai mi hai fatto mancare la tua preziosa amicizia, qualsiasi fosse la ragione, anche a 1000 km di distanza; Alessandro, per quel tocco di marchigianità che hai dato alle nostre serate assieme; Niccolò, per i fantastici viaggi insieme e per l'amicizia che nonostante tutto dura da più di vent'anni; Sergio, Ivan, Gianluca e Vittorio.

Ringrazio tutti i miei familiari per essermi stati sempre vicino in ogni momento ed essere stati un solido punto di riferimento in tutti questi anni: Margherita e Antonella, Silvana, Ettore, Pietro e Bianca e tutti i nonni Lidio, Betti, Peppe e Santa.

Infine, ma non ultimi per importanza, un ringraziamento speciale e di cuore va alla mia famiglia: a mia madre Giovanna, che, oltre ad avermi sopportato pazientemente in questi ultimi mesi, non si è mai persa una sveglia per un esame, un colloquio o una occasione importante e che mi ha insegnato a dare il meglio di me nella vita, ad impegnarmi sempre, perché i risultati arriveranno, anche inaspettati e che non manca mai di ricordarmi che l'apparenza è importante quanto la sostanza; a mio padre Dino, che probabilmente mi trasmesso la cura per i più piccoli dettagli, oltre ad essere sempre stato presente, anche in sessioni estive con 40°C in casa, per prepararmi qualche ottimo piatto. Infine, ringrazio mia sorella Nene, che è la migliore sorella del mondo, sempre attenta e premurosa, pronta a tutto per vedermi felice e che non mi ha mai fatto sentire in colpa per essere un po' meno presente nella sua vita, ma anzi è sempre stata presente nonostante tutto.